Process Development and Device Modelling of Gallium Arsenide Heterojunction Bipolar Transistors

Anssi Hovinen

Dissertation for the degree of Doctor of Science in Technology to be presented with due permission for public examination and debate in Auditorium S4 at Helsinki University of Technology (Espoo, Finland) on the 1st of June, 2001, at 12 o'clock noon.

Helsinki University of Technology
Department of Electrical and Communications Engineering
Electron Physics Laboratory

Teknillinen korkeakoulu
Sähkö- ja tietoliikennetekniikan osasto
Elektronifysiikan laboratorio

Distribution:
Helsinki University of Technology
Electron Physics Laboratory
P.O. Box 3000
FIN-02015 HUT
Finland
Tel. +358-9-451-2322
Fax. +358-9-451 5008

ISBN 951-22-5438-7
ISSN 0781-4984

Otamedia Oy
Espoo 2001

<table>
<tr><td>HELSINKI UNIVERSITY OF TECHNOLOGY
P.O. BOX 1000, FIN-02015 HUT
http://www.hut.fi</td><td>ABSTRACT OF DOCTORAL DISSERTATION</td></tr>
<tr><td colspan="2">Author</td></tr>
<tr><td colspan="2">Name of the dissertation</td></tr>
<tr><td>Date of manuscript</td><td>Date of the dissertation</td></tr>
<tr><td>Monograph</td><td>Article dissertation (summary + original articles)</td></tr>
<tr><td colspan="2">Department
Laboratory
Field of research
Opponent(s)
Supervisor
(Instructor)</td></tr>
<tr><td colspan="2">Abstract</td></tr>
<tr><td colspan="2">Keywords</td></tr>
<tr><td>UDC</td><td>Number of pages</td></tr>
<tr><td>ISBN (printed)</td><td>ISBN (pdf)</td></tr>
<tr><td>ISBN (others)</td><td>ISSN</td></tr>
<tr><td colspan="2">Publisher</td></tr>
<tr><td colspan="2">Print distribution</td></tr>
<tr><td colspan="2">The dissertation can be read at http://www.hut.fi/Yksikot/Kirjasto/Diss/</td></tr>
</table>

Abstract

This thesis discusses the processing and analysis of high speed semiconductor devices with emphasis on GaAs-based heterojunction bipolar transistors. The heterojunction transistor process is developed as an essential part of this thesis. Device physics is first reviewed in depth to construct a solid basis for physical one dimensional simulation of heterojunction bipolar junction transistors. Theory is then applied to a simulation platform in a way which facilitates device design and evaluation at practical level. The simulation platform was used in designing epitaxial layers for a transistor structure with heavily doped base layer and current gain target at 50. The developed transistor process relies on wet chemical isolation etching, and takes into account the restrictions that arise from the academic perspective of the processing environment. The process development goal was educational robustness.

The development effort for HBT process is explained in detail, and processing steps are illustrated with scanning electron microscope images. The most critical processing steps were for defining isolation depths. Isolation is based on slow citric acid wet chemical etching monitored with a high precision profilometer. Active devices form isolated hills or “mesas” on the semi-insulating substrate. Because of the rather tall etched structures the lithography is of planarizing type. The process includes a unique double layer planarising lithography for AZ 5214E resist, developed within the framework of this thesis. The lithography is doubly functional such that it also allows two resist layers to be patterned separately on top of each other, which is utilised in defining shallow air bridges in the transistor structures.

The most important measurement results are explained. Degradation of transistor performance after excessive heating or current stress is also demonstrated, and a method for processing devices with minimal amount of heating is introduced as a means to takcle the problem. Measured collector characteristics of various types of HBTs are given. Best DC characteristics were achieved with a transistor structure including non-alloyed contacts and Schottky diode collector. This thesis focused on process development and DC analysis of the transistor. Frequency characteristics were measured only for completeness. It is shown that even the non-optimized process was capable of producing transistors with power gain cut off frequency exceeding 1 GHz.

Keywords: ***heterojunction, aluminum gallium arsenide, simulation, low thermal budget, double layer lithography, process development***

Preface

Laboratory scale process development using compound semiconductors as starting material may be an endless source of inspiration and joy for a researcher. For another, it may become a nightmare. Processing steps on gallium arsenide are demanding. Samples may be extra fragile with appreciable price tag. Proper way of doing the job is crucial. In laboratory scale efforts, process development on compound semiconductors turns very easily into learning by doing mistakes. Picking up *tweezers of wrong material* would be a mistake. Using *force* would be another. For that matter, any *treatment* other than predetermined by the process schedule on the sample would be a provocation towards pain. It becomes obvious that completion of any process run on gallium arsenide is next to heroic as compared to *silicon processing*.

I have been privileged to have the opportunity to practise compound semiconductor research for several years with Electron Physics Laboratory of Helsinki University of Technology. The laboratory offers facilities for both silicon and compound semiconductor processing studies. My generation of students was the last to enjoy the famous *Old Clean Room of Wing C* with its 3” MOS line. Today, our students in the semiconductor field may have more modern equipment in their new clean rooms, but perhaps because of that may also start to loose the inspiring touch of the pioneering atmosphere that once was among the new comer trying to wade through the very first steps of semiconductor practise. I thank my supervisor, Professor Pekka Kuivalainen, and the Head of Electron Physics Laboratory, Professor Juha Sinkkonen for my education in *semiconductor physics, devices and technology* in the way which respects our civilizational history of technology as much as the modern aspects of semiconductor research.

This work has benefitted from the input of numerous individuals. Some of them are introduced in Chapter 6, *Acknowledgements*. After all, the most valuable criticism about the substance of this work was supplied by my children and my wife, with their justified arguments about occupying their gaming platforms with my Matlab™ simulations and text editors.

List of Symbols

A^*	*Richardson constant*
A	*First coefficient of the Joyce-Dixon approximation*
B	*Second coefficient of the Joyce-Dixon approximation*
C	*Third coefficient of the Joyce-Dixon approximation*
D	*Fourth coefficient of the Joyce-Dixon approximation*
$D(x)$	*Electric flux*
$D(X)$	*Transparency function with argument X*
$D_0(X)$	*Transparency function of an abrupt junction with argument X*
D_n	*Minority carrier diffusion coefficient in n-type semiconductor*
D_{nb}	*Electron diffusion coefficient in base*
D_p	*Minority carrier diffusion coefficient in p-type semiconductor*
D_{pc}	*Hole diffusion coefficient in collector*
D_{pe}	*Hole diffusion coefficient in emitter*
E_0	*Vacuum energy level*
E_{00}	*Activation energy of tunneling through a Schottky barrier*
E^*	*Lower boundary of integration for transparency calculation*
E_c	*Energy level of the bottom of conduction band*
E_f	*Fermi level of energy*
E_{f1}	*Fermi level of base layer*
E_{f2}	*Fermi level of emitter layer*
E_g	*Width of the forbidden band gap in energy*
$E_{g,emitter}$	*Width of the forbidden band gap in energy of emitter*
E_{g1}	*Width of the forbidden band gap in energy of p-side of the junction*
E_{g2}	*Width of the forbidden band gap in energy of n-side of the junction*
$E_{g,base}$	*Width of the forbidden band gap in energy of base*
$E_{g,collector}$	*Width of the forbidden band gap in energy of collecotr*
$E_{m,abrupt}$	*Energy difference between conduction band tip level and conduction band edge of neutral AlGaAs in an abrupt heterojunction*
$E_{m,graded}$	*Energy difference between conduction band tip level and conduction band edge of neutral AlGaAs in a graded heterojunction*

E_v	*Energy level of the top of valence band*
ΔE_c	*Conduction band energy difference*
ΔE_g	*Amount of the change in band gap width*
ΔE_v	*Valence band energy difference*
$F_{1/2}$	*Fermi-Dirac integral*
$F(x)$	*Electric field*
fN	*Joyce-Dixon approximation function for n-type semiconductor*
fP	*Joyce-Dixon approximation function for p-type semiconductor*
h	*Plank's constant*
I_B	*Base current*
I_E	*Emitter current*
I_C	*Collector current*
J_0	*Saturation current density*
J_{12}^*	*Electron current density from GaAs to AlGaAs of abrupt heterojunction due to Schottky junction analogy*
J_{21}^*	*Electron current density from AlGaAs to GaAs of abrupt heterojunction due to Schottky junction analogy*
J_b	*Total base current density*
J_c	*Total collector current density*
$J_{c,diff}$	*Collector diffusion current density*
$J_{c,drift}$	*Collector drift current density*
J_e	*Total emitter current density*
J_{gC}	*Base-collector depletion region generation current density*
J_n	*Total electron current density across AlGaAs/GaAs junction*
J_n^b	*Electron current density from GaAs to AlGaAs*
J_n^f	*Electron current density from AlGaAs to GaAs*
J_{ne}	*Emitter electron current density*
J_{NE}	*Coefficient for the calculation of emitter electron current density*
J_p	*Hole current density*
J_{PC}	*Coefficient for the calculation of collector hole current density*
J_{pe}	*Emitter hole current density*
J_{PE}	*Coefficient for the calculation of emitter hole current density*

J_r	*Neutral base layer recombination current density*
J_{re}	*Emitter-base depletion region recombination current density*
$J_{Shockley}$	*Current density of a pn-junction diode due to Shockley*
J_{sm}	*Current density from the flow of electrons from semiconductor to metal*
$J^*_{thermionic\ emission}$	*Total current density of abrupt heterojunction due to Schottky junction analogy*
k	*Boltzmann constant*
K	*Ratio of the permittivity-doping density product of either side of the junction*
L_n	*Minority carrier diffusion length in n-type semiconductor*
L_{nb}	*Electron diffusion length in base*
L_p	*Minority carrier diffusion length in p-type semiconductor*
L_{pc}	*Hole diffusion length in collector*
L_{pe}	*Hole diffusion length in emitter*
M_c	*Number of equivalent minima of the conduction band*
m_{de}	*Density of states effective mass of electron*
m_{dh}	*Density of states effective mass of hole*
m_e^*	*Conductivity effective mass of electron*
m_{e1}^*	*Conductivity effective mass of electron in base layer*
n	*Free electron concentration*
Δn	*Excess electron density*
n_0	*Thermal equilibrium electron concentration in p-type semiconductor*
n_{0b}	*Thermal equilibrium electron concentration in base layer*
N^+	*Density of ionized donors*
N^-	*Density of ionized acceptors*
N_A	*Acceptor doping density*
N_B	*Base doping density*
n_c	*Mobile electron concentration in collector depletion region*
N_C	*Collector doping density*
N_c	*Conduction band density of states*
N_{cb}	*Conduction band density of states of base layer*
N_{cc}	*Conduction band density of states of collector layer*
N_{ce}	*Conduction band density of states of emitter layer*

N_D	*Donor doping density*
N_E	*Emitter doping density*
n_{hot}	*Concentration of electrons with enough energy to surmount the conduction band spike by thermionic emission*
n_i	*Intrinsic carrier concentration*
n_{i1}	*Intrinsic carrier concentration of p-side of the junction*
n_{i2}	*Intrinsic carrier concentration of n-side of the junction*
n_p	*Minority electron concentration*
n_{p0}	*Minority electron equilibrium concentration*
N_t	*Trap state density*
N_v	*Valence band density of states*
N_{vb}	*Valence band density of states of base layer*
N_{ve}	*Valence band density of states of emitter layer*
N_{vc}	*Valence band density of states of collector layer*
p	*Free hole concentration*
Δp	*Excess hole density*
p_0	*Thermal equilibrium hole concentration in n-type semiconductor*
p_{0c}	*Thermal equilibrium hole concentration in collector layer*
p_{0e}	*Thermal equilibrium hole concentration in emitter layer*
R_{th0}	*Thermal resistance of the substrate*
q	*Unit charge*
Q	*Total charge density of the base layer*
R_n	*Simplifying coefficient without dimension used in excess electron density calculation*
R_p	*Simplifying coefficient without dimension used in excess hole density calculation*
T	*Device temperature*
U	*Recombination rate*
$V(x)$	*Potential*
V_a	*Applied potential*
V_{a1}	*Portion of applied potential over the p-side of the junction*
V_{a2}	*Portion of applied potential over the n-side of the junction*
V_{bc}	*Applied voltage over base-collector junction*
V_{BE}	*Potential difference between base terminal and emitter terminal*
V_{be}	*Applied voltage over base-emitter junction*

V_{bi}	*Built-in potential*
V_{b1}	*Portion of built-in potential over base side depletion region*
V_{b2}	*Portion of built-in potential over emitter side depletion region*
V_{cb}	*Potential difference between collector terminal and base terminal*
V_{ce}	*Potential difference between collector terminal and emitter terminal*
V_j	*Potential over the junction*
V_{j1}	*Portion of junction potential over the p-side*
V_{j2}	*Portion of junction potential over the n-side*
V_{jc}	*Potential over base-collector junction*
V_{je}	*Potential over base-emitter junction*
v_n^*	*Richardson-Dushman velocity*
v_s	*Electron saturation velocity*
v_{th}	*Thermal velocity of electrons*
W_{base}	*Neutral region thickness of base layer*
$W_{emitter}$	*Neutral region thickness of emitter layer*
$W_{collector}$	*Neutral region thickness of collector layer*
W_{dC}	*Width of the base-collector junction depletion region*
W_{gr}	*Width of the grading layer of graded heterojunction*
x	*AlAs mole fraction*
X	*Argument of the transparency function*
X_B	*p-layer thickness of a long diode*
X_C	*Coordinate of the collector side edge of the base-emitter junction depletion region*
X_E	*n-layer thickness of a long diode*
$X1$	*Coordinate of the base side edge of the base-emitter junction depletion region*
$X2$	*Coordinate of the emitter side edge of the base-emitter junction depletion region*
$X3$	*Coordinate of the base side edge of the base-collector junction depletion region*
$X4$	*Coordinate of the collector side edge of the base-emitter junction depletion region*
X_{je}	*Coordinate of the base-emitter metallurgical junction*
X_{jb}	*Coordinate of the collector contact junction*
X_{jc}	*Coordinate of the base-collector metallurgical junction*
β	*Large signal current gain*
γ	*Emitter injection efficiency*

ε_0	*Permittivity of vacuum*
ε_r	*Permittivity relative to vacuum*
ε_s	*Permittivity of the semiconductor*
ε_{s1}	*Permittivity of the base layer*
ε_{s2}	*Permittivity of the emitter layer*
ε_{s3}	*Permittivity of the collector layer*
η_n	*Simplifying coefficient without dimension used in excess electron density calculation*
η_p	*Simplifying coefficient without dimension used in excess hole density calculation*
$\Theta 1$	*Energy difference between Fermi level and GaAs valence band edge*
$\Theta 2$	*Energy difference between AlGaAs conduction band edge and Fermi level*
σ	*Capture cross section of a trap state*
σ_n	*Electron capture cross section of a trap state*
σ_p	*Hole capture cross section of a trap state*
τ	*Minority carrier lifetime*
τ_n	*Electron lifetime in p-type semiconductor*
τ_p	*Hole lifetime in n-type semiconductor*
ϕ_B	*Schottky barrier height*
ϕ_B^*	*Energy difference between Fermi level and the tip of conduction band spike*

Abbreviations

Al	Aluminum
AlAs	Aluminum arsenide
AlGaAs	Aluminum gallium arsenide
AlN	Aluminum nitride
As	Arsene
ASCII	American Standard Code for Information Interchange
BJT	Bipolar Junction Transistor
CPE	Chemical plasma etching
Ga	Gallium
GaAs	Gallium arsenide
GaAsSb	Gallium arsene antimonide
GaN	Gallium nitride
HBT	Heterojunction Bipolar Transistor
HEMT	High Electron Mobility Transistor
In	Indium
InGaAs	Indium Gallium Arsenide
InGaP	Indium Gallium Phosphide
InP	Indium phosphide
MBE	Molecular Beam Epitaxy
MOCVD	Metallo-Organic Chemical Vapor Deposition
MOVPE	Metallo-organic Vapor Phase Epitaxy
PECVD	Plasma enhanced chemical vapor deposition
RBS	Rutherford Back Scattering

Contents

1 Introduction 1
2 Basic Device Operation 6
2.1 Nomenclature and Definitions 6
2.2 Band Gap Tailoring 16
2.3 Electrode Currents of a transistor 19
2.4 Abrupt Heterojunction under thermal equilibrium 21
2.5 AlGaAs / GaAs –Heterojunction Under Applied Voltage 29
2.6 Current through abrupt AlGaAs / GaAs –Heterojunction 31
2.7 Current through graded AlGaAs / GaAs –Heterojunction 35
2.8 Transistor Base Layer as a Charge Storage 36
2.9 Large Signal Current Gain of a Heterojunction Bipolar Transistor 42
2.10 Modeling of the transistor terminal currents 44
2.11 Recombination and Generation currents in Depletion Regions 67
2.12 Band Gap Narrowing 73
2.13 Bias Conditions for Simulations 77
3 Experimental 80
3.1 Epitaxial Structure 80
3.2 Current Gain Simulation of the Example Structure 82
3.3 Epitaxial Layers in Detail 86
3.4 Crystal Orientation 89
3.5 Processing Steps 92
3.5.1 Alignment marks 93
3.5.2 Emitter Mesa Pattern 94
3.5.3 Base Mesa Pattern 95
3.5.4 Emitter and Collector Ohmic Metal 95
3.5.5 Base Ohmic Metal 98
3.5.6 Collector Mesa Pattern 98
3.5.7 Insulation 99
3.5.8 Contact Holes 99
3.5.9 Wiring Metallisation 100

3.5.10 Passivation 101
3.5.11 Pad Opening 101
3.6 Naming Convention of the Processed Devices 101
3.7 Test Structure with Loose Tolerance Design 102
3.8 Choice of Contact Metallisation Material 103
3.9 Self Heating Effect 106

4 Practical Measurements 110
4.1 Analysis environment 110
4.2 Connecting the Device to measurement 111
4.3 Extracting Equivalent Circuit Parameters from Measurements 111
4.4 Conclusive Remarks on the Process Run 116
4.5 Stability of the Measured Transistor Performance 119
4.6 Evaluation of the Frequency Response of the Processed Devices 125

5 Conclusions 127
6 Acknowledgements 129
7 References 130

"We used GaAs despite its technology, not because of it, and the threat was never far away that Si devices, with their much simpler and more highly developed technology, would catch up with GaAs performance, the fundamental advantages of GaAs notwithstanding."

-Herbert Kroemer 1981

1 Introduction

The opening quote for this thesis was taken from Dr. Kroemer's introduction into *Heterostructure Bipolar Transistors and Integrated Circuits [r01].* Dr. Kroemer was awarded the Nobel Price in Physics 2000, together with Dr. Zhores I. Alferov "*for their invention and development of fast opto- and microelectronic components based on layered semiconductor structures, termed semiconductor heterostructures*" [r02]. Kroemer proved theoretically in 1957 that a transistor with wide band gap emitter overcomes "conventional" transistors for current amplification and high speed operation [r03]. In 1963 he proposed the principle of the heterojunction laser, at the same time but independently with Dr. Zhores I. Alferov. During the invention Kroemer was with Varian in Palo Alto, California while Dr. Alferov was with A. F. Ioffe Physico-Technical Institute, St. Petersburg, former Leningrad.

Dr. Alferov was also the first to successfully grow lattice matched AlGaAs compound semiconductor on top of GaAs crystal with clear interface in 1967 [r04]. The first patent that was set forth about heterojunction bipolar transistors was by William Shockley, filed 26 June 1948, within his patent application for the "conventional" transistor [r05]. Shockley was awarded the Nobel Prize in Physics already in 1956 with his co-workers Bardeen and Brattain for the development of the semiconductor transistor [r06]. The *basic work on information and communication technology* that was honoured once again by the Nobel Prize in Physics has made possible the wide use of communication links, e.g., for internet and telephony, the actual skeleton of the modern information society.

As the need for mass produced compound semiconductor devices have increased, progress has been made also on wafer size and integration level. Portable communication systems need to be small, light weight and cheap. To fulfill mass production needs, gallium arsenide industry has moved forward to 6" wafer sizes. Traditional small scale GaAs-processing with mesa isolation techniques have been accompanied by "high integration" GaAs-processes for VLSI-scale production that resemble more closely traditional silicon processing and thus benefit from the available silicon industry equipment. Since the very early efforts towards good quality heterointerfaces at late 60's, the science of heterojunction bipolar technology has matured to a well respected commercial level. In the beginning of year 2000 it was already easy to find over 30 commercial manufactures for ,e.g., heterojunction bipolar transistors (HBT's). Among the others,

one could choose between *EiC Corporation, Fujitsu FCSI, Matsushita, Motorola, NEC, Philips, RF Micro Devices, Raytheon, Rockwell, Siemens, TRW, Thomson, Toshiba*, or *TriQuint* to contact with. Even the high voltage applications are no longer a bottle neck for HBT's [r07].

Today the leading research groups in the field of high speed semiconductor technology are competing against technology oriented challenges in the frequency region not far from 1 THz [r08]. The tools used to reach the higher frequencies include reduction of device dimensions by electron beam lithography for the sub-micron patterning, substrate transfer process to remove the active component from the substrate and subsequent bonding to conductive ground to remove serial resistance of the lower part of the device, and usage of Schottky diode collector contacts to remove the parasitic collector resistance. Household communication technology of the year 2020 may well be in dept for those research efforts at their own time.

The purpose of this thesis is more close to the technology challenges that are faced in our own time and space. The basic attitude of Dr. Kroemer still holds. We use GaAs despite its technology, not because of it, and the threat is never far away that Si devices, with their much simpler and more highly developed technology, would catch up with GaAs performance, the fundamental advantages of GaAs notwithstanding. The maturity level of silicon-germanium (SiGe) technology is also acknowledged. Today we may use indium phosphide (InP) or gallium nitride (GaN) to emphasize the fundamental material advantages.

In the present thesis the processing and modelling of "conventional" heterojunction bipolar transistors are studied. A conventional HBT technology refers to mesa isolation technique in the electrical separation of active devices, which produces a transistor structure as shown in Figure f1. The subject of compound semiconductor processing technology is very vast. Practically every processing step should have devoted by its own thesis, and thus profound treatment of the overall subject of device processing was not possible. The substance of this work has three corner stones. First, physical one dimensional modelling of AlGaAs/GaAs heterojunction bipolar transistor is discussed and the model equations are converted to a uselful form to constitute a Matlab™ simulation platform for the device. Second, a representative device is designed using the Matlab simulations as guidance. Third, a heterojunction bipolar transistor process is developed and measured device parameters are evaluated against the simulations.

The work towards bipolar transistor processing that will be introduced in this thesis has its origin in early 90's when I had the opportunity to study the processing of modulation doped heterojunction field effect transistors (MODFET's) with Electron Physics Laboratory of Helsinki University of Technology [r09]. Many of the processing methods that are used in the HBT process were originally developed during those efforts. The very high fidelity wet chemical etching method for mesa isolation was among the most useful legacy of my early studies on compound semiconductor processing. Among others there is the double layer lithography method that I was now able to utilise at full benefit in forming air bridge structures for wiring metallisations. Air bridge metallisation technique is a prerequisite for high speed device processing in general. Later I focused on the processing of crystalline silicon solar cells for a few years [r10]. The legacy of that work for this thesis was on the understanding of the importance of feedback from process room back to development desk via numerous measurements and device simulation. Some of the Matlab™ simulation practices and code that were once used for evaluation of silicon solar cells found new service in this work for evaluation of measurement results.

To be able to interpret the measured performance of a transistor a solid understanding of the basic operation of the device is needed. There is plenty of commercial sofware and service available for routine treatment of an HBT with a predetermined set of equations [r11]. In the present thesis the need for flexible simulations with full access to device equations constituted the driving force towards proprietary code generation. The physical equations that govern over HBT operation were encoded into a set of Matlab™ files for easy access. It became soon evident that the encoded HBT simulation platform served its purpose more than well in demonstration of the operation of an ideal heterojunction transistor under bias. The simulation equations are almost solely based on the physical parameters of the device so that the link to physical reality is conserved, and the user is not left with choosing proper set of artificial fitting parameters. Yet the equations were kept as simple as adequate in order not to forget the purpose of the tool as a robust educational introduction into the physics of traditional heterojunction bipolar technology. Additionally, the development work with the simulation code served as a "learning by doing" experiment, revealing many practical points in basic device physics that were not properly recognized by the author before. Because of the free access to the code files, new ideas about

HBT modelling may now be readily tested out by modifying the equations and definitions accordingly. In practical use under the present thesis the simulation platform proved to be an ideal tool in studying, e.g., the simple questions like *"what if the numerical value of electron thermal velocity is doubled"*, *"what if the transparency of conduction band spike is increased by 10%*", "*what if the band gap narrowing effect is ignored*", or "*what if hole currents are ignored*". The simulation data analysis is flexible, as the user may encode his own Matlab™ files for graphical studies about the results. Most of the illustrative graphs in this thesis are generated using the HBT simulation platform developed by the author.

Because of the importance of physical background to the process development and evaluation, the equations that govern over the electrical operation of a heterojunction bipolar transistor are derived in length, occupying about 50 pages. It was tempting to leave the equations away completely from the text. However, forming the basis of the HBT simulation platform, exlusion of the equations would not have been fair for the possible reader who otherwise might get more interested in the field of HBT physics and perhaps find his own use for the simulation platform.

Modification of the simulation code for future needs is made easy by extensive use of commenting in plain english inside the Matlab™ files. The files are in ASCII format and thus editable in almost any text editor. The basic level of education in algebra with Matlab™ should be enough to understand the composition of the simulation files. The code is not included in the printed version of this thesis, as the present set of files would occupy about 30 pages. Instead, the code is distributed in electronic form by the author for educational and non-commercial purposes on request.

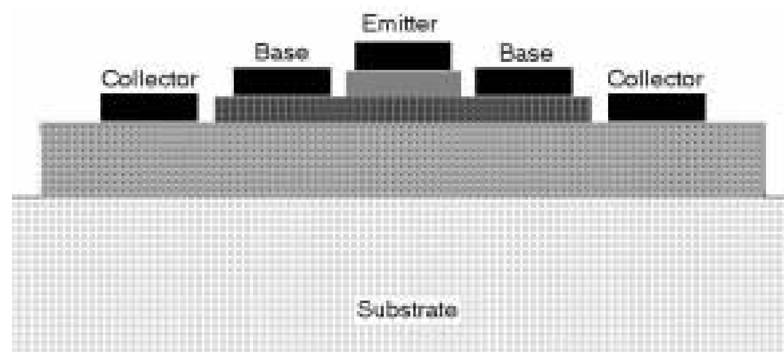

Figure f1: Cross section of a mesa isolated heterojunction bipolar transistor.

The present thesis is organized in the same precise way as is the conventional, mesa isolated heterojunction bipolar transistor itself:

Chapter 1, *Introduction,* serves as "*a low resistivity contact layer"* into the rather involved subject of heterojunction bipolar technology.
Chapter 2, *Basic Device Operation,* serves as the actual "*emitter"* for the physical background and equations governing HBT operation. The basic device physics is reviewed at a level that allows the physical equations to be implemented in one-dimensional simulations. The equations were also transferred into a series of Matlab™ coded m-files that consitute a complete simulation platform for one dimensional HBT evaluation. In order to maintain applicability to simple device characterisation without extensive use of computer iterations, the treatment concentrates mainly on ideal transistor characteristics. Series resistance losses and two dimensional potential variations are not included in the core equations. However, the importance of series resistance losses is acknowledged, and a simple resistivity model is included into simulation code that calculates first estimates on resistive losses across transistor layers for the user. These refinements are not included in the text of this thesis.

Chapter 3, *Experimental*, forms the practical "*base layer"* for this thesis. The heterojunction material related issues are studied, and the processing steps are introduced in detail.

Chapter 4, *Practical Measurements*, serves as a "*lightly doped collector layer"* that is used to gain feedback from the processing phase for preliminary critical evaluation.

Chapter 5, *Conclusions*, serves the purpose of a "*heavily doped sub-collector"* with conclusive evaluation of the subject.

Chapter 6, *References*, finally forms an organised *"low resistivity collector contact"* to the outer circuitry.

2 Basic Device Operation

2.1 Nomenclature and Definitions

The electron tube was the basic building block for electrical amplifying circuits before bipolar transistor era. [r12]. The tube is still used in applications that need extremely high power levels, such as radio transmitter power stages. Tube equivalent for a transistor is a triode which in its basic form constitutes of an electrically heated cathode filament or "emitter", a metallic anode plate or "collector", and a metallic mesh or "grid" in between emitter and collector. All the electrodes are encapsulated into a sealed cylinder that maintains vacuum condition. The external electrical connections to the electrodes are accomplished with metallic feed-throughs. In operation, the emitter filament is heated by current until the electrons in filament material gain enough energy to escape to vacuum. The heated emitter filament is surrounded by a cloud of free electrons. The escape process is called "thermionic emission" of electrons. The minimum energy needed for emission is equal to the work function of the filament material. If there was a potential difference between emitter filament and collector plate such that the collector was made more positive than emitter, the emitted electrons would start to drift towards collector. Before reaching the collector plate the electrons need to pass the grid. If there was an applied potential on the grid such that electron travel towards collector is disturbed, the collector plate current would be controlled by the grid potential. Usually the grid is biased negative with respect to emitter.

The basic operation principle of a "semiconductor triode" or a bipolar junction transistor (BJT) is not as self-explanatory as was the vacuum tube triode, although many of the definitions are adopted from the vacuum tube literature [r06]. In a BJT the vacuum is replaced by purified semi-conductive solid state material, e.g., silicon. The first discrepancy between "solid state semiconductor triode" and vacuum tube comes from the fact that in a semiconductor there are two kinds of charge carriers that can constitute electrical current flow. Semiconductor crystal can conduct electrical current either by

means of free electrons, or by moving vacancies of electrons that are called "holes". Both of the charge carrier types are present in any semiconductor. The product of the carrier concentrations in thermal equilibrium is constant. If n [cm^{-3}] is the electron concentration and p [cm^{-3}] is the hole concentration, then

(e1)
$$np = n_i^2,$$

where n_i [cm^{-3}] is the "intrinsic carrier concentration" of the semiconductor [r13]. In an undoped, or "intrinsic" semiconductor, the charge carrier concentrations are equal. The type of majority charge carriers of a semiconductor is controlled by intentionally doping of an otherwise pure semiconductor crystal with a definite amount of atoms that either have more valence electrons or less valence electrons than the crystal atoms. Electron-type conduction is referred as "n-type" and hole-type conduction as "p-type". The "npn-type junction transistor" structure constitutes of a p-type semiconductor layer sandwiched between two n-type layers. Importantly, the pn-junctions are monocrystalline in nature maintaining the periodicity of the crystal lattice at the atomic level. A "npn"-structure that is made by mechanically compressing a stack of semiconductors of proper doping together would not constitute a proper transistor because of the broken crystal bonds on the interfaces.

The first *n*-type layer is the "emitter" of a npn-type junction transistor. The second *n*-type layer is the "collector". Because there is no physical grid in between, the *p*-type layer is called "base" instead. Historically the name refers to the first germanium transistors where "base" was the actual basis of the construction [r06]. In principle, the npn-transistor is symmetrical, and one could expect some transistor action even if the "emitter" and "collector" electrodes were reversed. The electron tube triode would not work at all in "reverse mode" because of the need for a heated emitter filament.

Similarly to the electron tube triode, the main function of the transistor is to emit charge carriers from the emitter through base layer, and collect the charge carriers in the collector layer to produce external collector current. The base electrode should have an

action such that the collector current will be controlled by the base. In a semiconductor the force that can move charge carriers is induced either by an electric or magnetic fields, or by a spatial concentration gradient of charge carriers. The spatial concentration gradient generates movement by diffusion. The bipolar junction transistor operation is based on controlling the minority carrier concentration gradient across the base region.

In a npn-type junction transistor, the base layer minority carriers are electrons. The control over the electron concentration across the base is achieved by utilizing the voltage dependence of minority carrier concentrations in depletion region edges of base-emitter *pn*-junction. According to the *pn*-diode law, the minority carrier concentrations in the depletion region edges of a junction depend exponentially on the voltage over the junction [r13]. For the base side depletion region edge at point $x = x_d$ of the emitter-base junction of a npn-transistor the electron concentration $n_p(x=x_d)$ is thus

(e2) $$n_p\left(x = x_d\right) = n_{p0} e^{\frac{qVbe}{kT}},$$

where n_{p0} electron equilibrium concentration in base, q is the electron charge, V_{be} is the bias voltage across the junction, k is the Boltzmann constant, and T is the junction temperature. The electron concentration deeper in the base decreases exponentially with distance to the depletion region edge. If the base layer is very thick, the electron concentration reaches again the equilibrium concentration value of n_{p0}. A npn-structure with a thick *p*-layer forms merely two *pn*-junction diodes back to back with no transistor action. For the proper operation of the bipolar transistor the base thickness should be small to avoid such condition. Usually the base thickness is small enough to justify approximation of the exponential decay of minority carrier concentration by a straight line. In Figure f2 the minority carrier concentrations in different areas of the npn-transistor are drawn in the normal operation condition, where base-emitter junction is forward biased and base-collector junction is reverse biased. The condition is referred to as “forward active mode”. The *pn*-junction law forces the electron concentration in the base side of the base-collector depletion region to a very low value because of the

reverse junction bias. The minority carrier concentration across the base has now roughly triangular shape, and the peak value of $n_p(x=x_d)$ is controlled by external bias voltage V_{be}. The bias voltage V_{bc} across the base-collector junction does not have noticeable contribution to the base minority carrier concentration in this picture if the reverse bias condition is kept valid. When the transistor is biased such that emitter-base junction is reverse biased and collector-base junction is forward biased, the condition is referred to as " reverse active mode". In this mode, the base minority carrier distribution is controlled by V_{bc}.

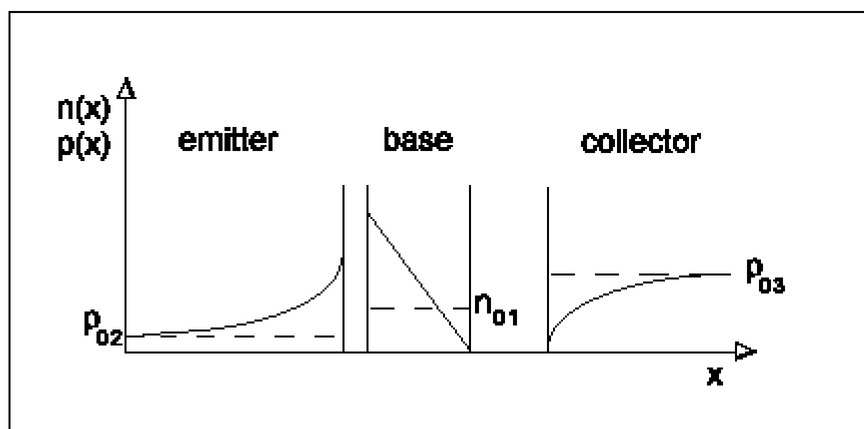

Figure f2: Minority carrier concentrations across a npn-transistor biased in forward active mode. n_{01} is minority electron concentration in neutral base, p_{02} is minority hole concentration in neutral emitter, and p_{03} is minority hole concentration in neutral collector.

The benefit of using a solid state material instead of vacuum tube arrangement comes from the energy needed to transfer an electron from emitter region to collector region. There is no need to remove the electron from the crystal to vacuum level during the transfer. As a consequence, the power consumption of the transistor is only a small fraction of that of the electron tube triode. Typical value of V_{BE} for a silicon bipolar junction transistor in forward active mode is about 0,7V.

Besides possessing two types of charge carriers, a bipolar transistor and an electron tube triode has another discrepancy. In a vacuum tube the free electrons travel at vacuum energy level. The charge carriers in a BJT are allowed to move on definite energy bands inside the semiconductor crystal. Holes are free to move in "valence" bands of energy, and electrons are free to move in "conduction" bands of energy. Valence band and conduction band are separated by a "forbidden band gap". In order to create free charge carriers into an intrinsic semiconductor, electrons in the filled energy states of valence band has to be given enough energy to "jump over the forbidden band gap" thus forming vacancies of electron, or "holes", into the valence band of energy, and free electrons into the conduction band of energy. Another way to introduce free charge carriers into the crystal is the aforementioned intentional doping of the semiconductor. The free charge carriers on the valence and conduction bands tend to preserve minimum energy. Excess energy is transferred to the crystal lattice as heat until the charge carrier is on its lowest possible energy state. For electrons, the lowest energy is found on the "bottom of the conduction band", and for holes it is on the "top of the valence band". A simplified schematic picture about the crystal seen by charge carriers can be drawn by representing the energy band boundaries as lines separated by a forbidden band gap in energy versus distance coordinate system, or the energy band diagram.

The energy band diagram of a npn-type junction transistor under thermal equilibrium is presented in Figure f3. The energy level for vacuum E_0 is included for convenience. Vacuum energy level is always a straight line, as there is never spatial energy derivatives associated with the vacuum level. If there was, one could emit electrons to the vacuum level and absorp them back after a distance thus creating energy from nothing. The dashed line inside the forbidden band gap is the "Fermi level" of energy E_f. The fermi level concept comes from statistical physics and governs the flow of particles, such as electrons and holes, in a same pictorial manner as temperature governs the flow of energy. The electrons wish to move from the areas of higher Fermi level to the areas where the Fermi level is lower. The energy separation between vacuum level E_0 and

Fermi level E_f is the work function of the semiconductor material, or the amount of energy in average that has to be supplied to the electron to remove it from the semiconductor. Under thermal equilibrium, the Fermi level is constant throughout the crystal.

The Fermi level energy and charge carrier concentrations are thus interdependent. The Fermi level resides near conduction band edge on emitter and collector layers of the npn-transistor because there the semiconductor crystal was doped n-type. On the p-type base the Fermi level resides near the valence band edge. Figure f3 reveals that under thermal equilibrium the energy band edges have to bend to keep the Fermi level constant. The bending represents electric fields inside the crystal that have depleted free electrons and holes from the region of bending. The aforementioned depletion region edges are the points where the band derivative returns to zero. The regions with no electrical field are the “neutral regions” of the semiconductor.

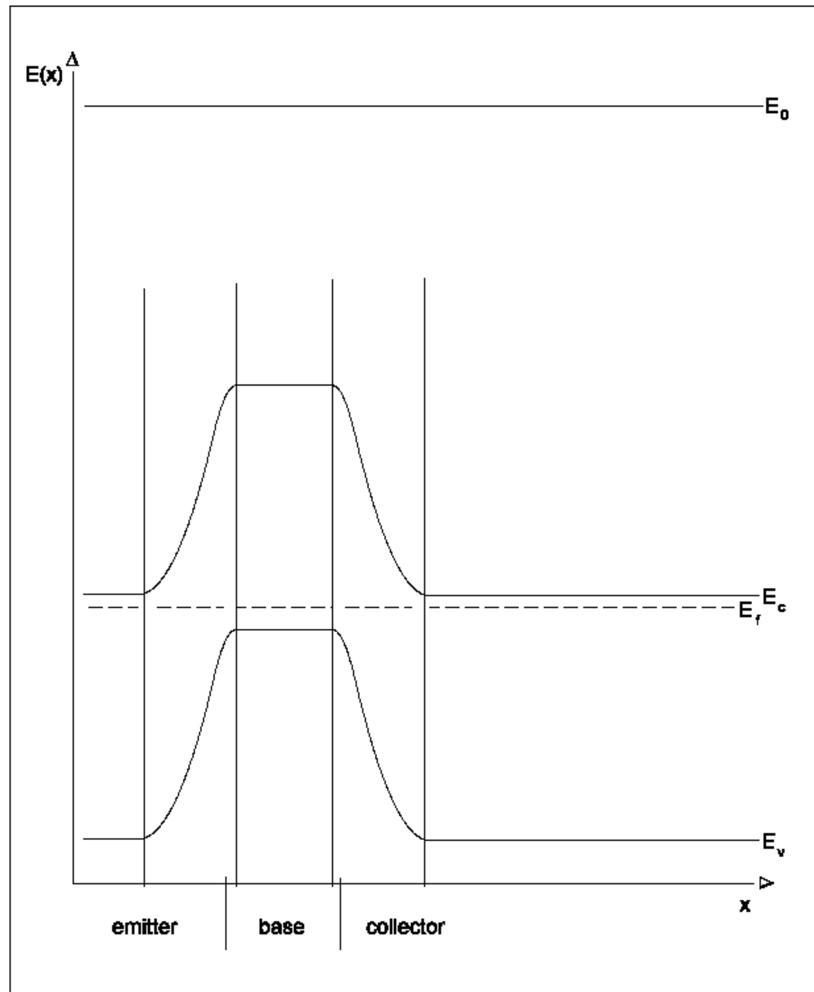

Figure f3: The energy band diagram of a npn-type junction transistor under thermal equilibrium.

The exact position of the Fermi level is found using the Fermi-Dirac integral [r13]. For electrons in a n-type semiconductor the relation between electron concentration n and Fermi level E_f is

(e3)
$$n = N_c \frac{2}{\sqrt{\pi}} F_{\frac{1}{2}}\left(\frac{E_f - E_c}{kT}\right),$$

where the Fermi-Dirac integral is

$$F_{\frac{1}{2}}(\eta_f) = \int_0^{\infty} \frac{\sqrt{\eta}}{1+e^{(\eta-\eta_f)}} d\eta,$$

and N_c is the effective density of states in the conduction band, or

(e4) $$N_c = 2\left(\frac{2\pi m_{de} kT}{h^2}\right)^{\frac{3}{2}} M_c,$$

where m_{de} is the "density of states" effective mass for electrons, h is the Planck´s constant, and M_c is the number of equivalent minima in the conduction band. For holes in p-type material the relation is

(e5) $$p = N_v \frac{2}{\sqrt{\pi}} F_{\frac{1}{2}}\left(\frac{E_v - E_f}{kT}\right),$$

where N_v is the effective density of states in the valence band, or

(e6) $$N_v = 2\left(\frac{2\pi m_{dh} kT}{h^2}\right)^{\frac{3}{2}},$$

where m_{dh} is the "density of states" effective mass for holes.

The Fermi-Dirac integral is mathematically involved. In practical calculations of this thesis the relation between electron concentration n and Fermi level in n-type semiconductor is obtained from the Joyce-Dixon approximation [r14],

(e7) $$\frac{E_f - E_c}{kT} = \ln\left(\frac{n}{N_c}\right) + A\cdot\left(\frac{n}{N_c}\right) + B\cdot\left(\frac{n}{N_c}\right)^2 + C\cdot\left(\frac{n}{N_c}\right)^3 + D\cdot\left(\frac{n}{N_c}\right)^4,$$

where A = 0,353553, B = $-4{,}95009\cdot 10^{-3}$, C = $1{,}48386\cdot 10^{-4}$, and D = $-4{,}42563\cdot 10^{-6}$. For

hole concentration p in p-type semiconductor the Joyce-Dixon approximation is

(e8) $$\frac{E_v - E_f}{kT} = \ln\left(\frac{p}{N_v}\right) + A \cdot \left(\frac{p}{N_v}\right) + B \cdot \left(\frac{p}{N_v}\right)^2 + C \cdot \left(\frac{p}{N_v}\right)^3 + D \cdot \left(\frac{p}{N_v}\right)^4,$$

where the coefficients *A, B, C* and *D* are the same as previously. When the doping level of the semiconductor is moderate, the Fermi Dirac integral can be approximated further. The Boltzmann formula for n-type semiconductor is

(e9) $$n = N_c e^{\frac{E_f - E_c}{kT}}.$$

For p-type semiconductors the formula is

(e10) $$p = N_v e^{\frac{E_v - E_f}{kT}}.$$

Figure f4 compares the Joyce-dixon approximation and Boltzmann formula. It is seen that if the Fermi level lies in the forbidden band gap with energy separation to band edges more than 3kT, the Boltzmann formula coincidences with the Joyce-Dixon approximation. The exact result from the Fermi-Dirac integral would overlap the Joyce-Dixon approximation throughout the scale. The 3kT distance corresponds to carrier concentrations that are about 5% of the respective energy band density of states . For silicon, the 5% limiting concentrations are $n = 1{,}5 \cdot 10^{18}$ cm^{-3}, and $p = 5{,}3 \cdot 10^{17}$ cm^{-3}. For gallium arsenide, the concentrations are $n = 5{,}3 \cdot 10^{17}$ cm^{-3} and $p = 3 \cdot 10^{17}$ cm^{-3}.

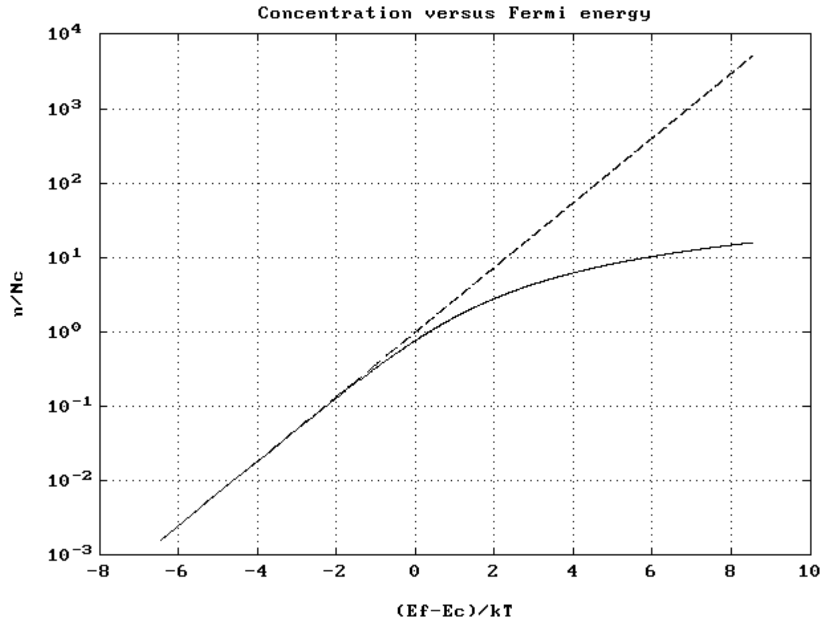

Figure f4: Comparison of Boltzmann approximation (dashed line) and Joyce-Dixon approximation (solid line) of the Fermi-Dirac integral. The exact value of the integral would almost overlap the solid line as verified in, e.g., [r14], page 34.

From equations (e1) , (e9), and (e10) the intrinsic carrier concentration n_i can be obtained,

(e11) $$n_i = \sqrt{N_c N_v} e^{-\frac{E_g}{2kT}},$$

where $E_g = (E_c - E_v)$ is the width of the forbidden band gap. Because the calculation included Maxwell-Boltzmann statistics, the formula for n_i needs not to be valid with heavily doped samples. It is seen from the formula that the intrinsic carrier concentration of a semiconductor decreases exponentially as E_g increases. In practice, this has application in the case of heterointerfaces, where semiconductive layers of different band gaps are joined together in a manner that the crystal periodicity is maintained. The electrical properties of the material change in a very short distance around the interface allowing the design of modern semiconductor devices such as High Electron Mobility Transistors (HEMTs) and Heterojunction Bipolar Transistors (HBTs).

2.2 Band Gap Tailoring

Figure f3 represented the energy band diagram of a conventional bipolar junction transistor in thermal equilibrium. The forbidden band gap was of constant width throughout the device. With modern processing methods, such as Molecular Beam Epitaxy (MBE) or Metallo-Organic Chemical Vapour Deposition (MOCVD) it is possible to make semiconductor crystals that include spatial modulation in the forbidden band gap width. In epitaxial processing, the monocrystalline semiconductor material is grown by stacking semiconductor atoms with almost molecular accuracy. The electrical properties of the semiconductor are controlled by adding a specific amount of dopant atoms and even varying the atoms that constitute the main crystal.

The heterojunction bipolar transistor gets its name from the composition of the transistor structure. In a single heterojunction structure the emitter layer of the transistor is made of material that has wider forbidden bad gap than base or collector layers. The possible material choices are dictated by proper crystal lattice match between the layers. Ideally, lattice constants between adjacent layers should be identical, thus no strain is generated during epitaxial growth of the structure. Excess strain would break the bonds between lattice atoms in the vicinity of heterojunction, yielding to imperfect crystal and poor functionality of the transistor.

Figure f5 shows the lattice constant mapping of different semiconductor materials. As can be seen, AlAs and GaAs have almost the same lattice constant, so any composition of single crystal $Al_xGa_{1-x}As$ is possible to be grown on top of GaAs crystal. The band gap of the ternary compound adjusts with the AlAs mole fraction x. InGaP lattice matched to GaAs is also possible. Other choices could be, e.g., GaAsSb lattice matched to InP or GaInAs lattice mathed to InP. The traditional choice for a heterostructure material pair has been $Al_xGa_{1-x}As$ on top of GaAs, where AlAs mole fraction is kept below 0,3 to avoid complications that arise from the $Al_xGa_{1-x}As$ energy band diagram shifting from direct band gap structure to indirect gap structure when x approaches 0,45 [r13].

$GaAs/Al_xGa_{1-x}As$ structure is the most studied material in high speed compound semiconductor research, and its applications have matured to commercial level. In recent years the compound semiconductor research has been bending towards studies on GaN-AlN combination. It is seen in Figure f5 that the lattice match is good, and both the energy gaps and their relative difference is appreciable. Nitrogen based compounds will probably find their use in high temperature and high power applications in the future.

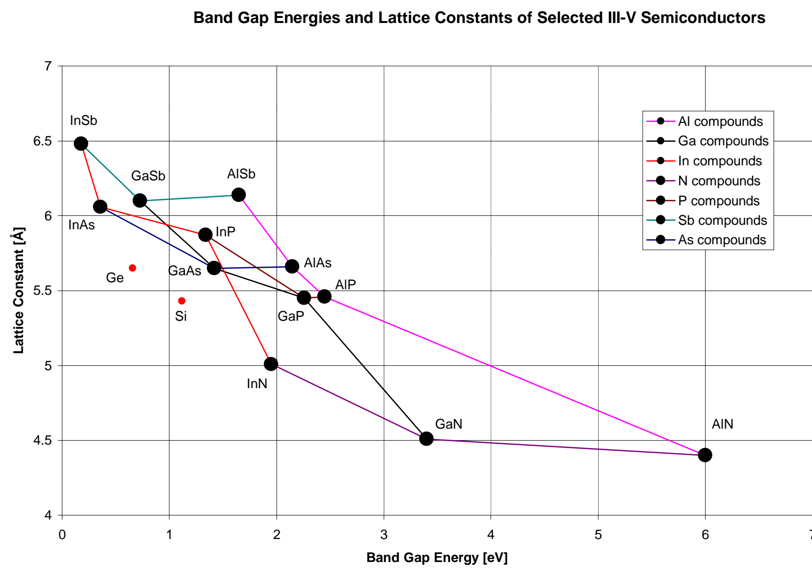

Figure f5: The lattice constant mapping of different III-V semiconductor materials. Silicon and germanium values are also shown (red dots). Numerical data is collected from [r13] and [r15].

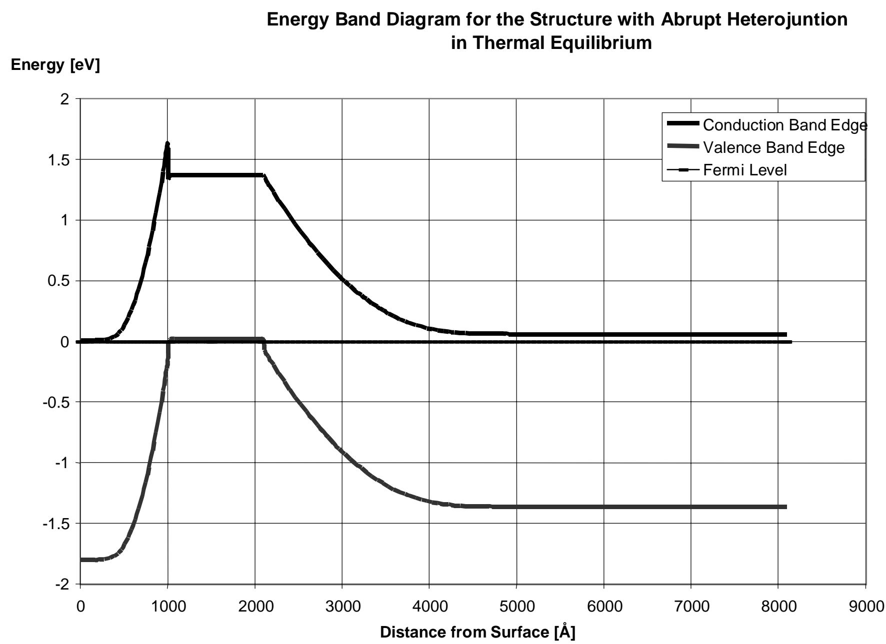

Figure f6: Energy band diagram of an abrupt heterojunction bipolar transistor. Numerical parameter values that were used in the enegy band simulation are introduced in chapter 3.2.

The energy band diagram of a typical heterojunction bipolar transistor in thermal equilibrium is shown in Figure f6. The device is npn-type with $Al_{0,25}Ga_{0,75}As$ emitter, GaAs base and GaAs collector. There are some differences to the conventional bipolar transistor picture of Figure f3. Forbidden energy band gap width changes abruptly in the base-emitter junction, as the emitter band gap is wider than in base or collector. This generates the spike on the conduction band that is seen in the Figure f6. The difference in band gap widths ΔE_g is

(e12) $$\Delta E_g = E_{g,emitter} - E_{g,base}.$$

The $Al_xGa_{1-x}As$/GaAs heterojunction shares the bandgap difference ΔE_g between conduction band difference ΔE_c and valence band difference ΔE_v so that

$$\Delta E_c(x) = \begin{cases} (1{,}247 - 0{,}55)x, & 0 \le x \le 0{,}45 \\ 0{,}476 + (0{,}125 - 0{,}55)x + 0{,}143x^2, & 0{,}45 < x \le 1{,}0 \end{cases}$$

(e13)

$$\Delta E_v(x) = 0{,}55x, \qquad 0 \le x \le 1$$

$$\Delta E_g(x) = \Delta E_c(x) + \Delta E_v(x)$$

where x is the AlAs mole fraction of the emitter and the energy unit is *eV* [r14]. The equation for conduction band spike is deliberately presented in a form that emphasizes its dependence on x with reference to valence band. Numerical values of band gap discontinuities for practical calculations of this thesis rely on equations (e13).

2.3 Electrode Currents of a transistor

The main purpose of a transistor is to serve as a controllable conduit of charge carriers from its emitter electrode to its collector electrode. The overall picture inside the conduit includes also leaks and obstacles of various kind. One of the most important relationships inside a transistor is how efficiently the base controls over the collector current. Figure f6 gives a collection of relevant definitions and parameters for the calculation of the electrode currents of a heterojunction bipolar transistor. The figure represents a transistor in forward active mode as emitter-base junction is forward biased and base-collector junction is reverse biased.

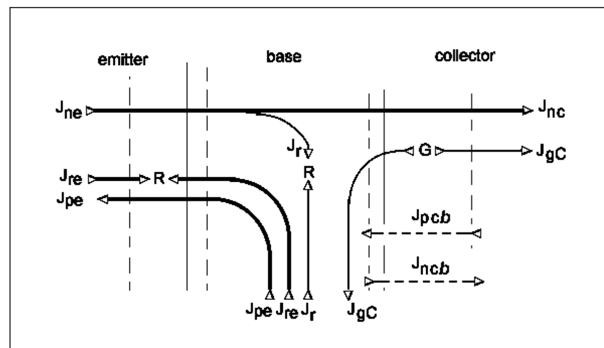

Figure f6: A collection of relevant definitions and parameters for the calculation of the electrode currents of a heterojunction bipolar transistor.

Physical surfaces of the transistor are not included in the figure. Currents that arise from surface recombination of the exposed areas of the transistor are thus not seen. The emitter current density J_e is represented by three kinds of charge carrier flow. By definition, the positive direction of J_e is away from the transistor. The three components of J_e are (1) flow of electrons from emitter across the emitter-base junction to the base region J_{ne}, (2) flow of electrons that recombine inside the emitter-base depletion region area with holes supplied by the base J_{re}, and (3) flow of holes that are back-injected from base across the emitter-base junction J_{pe}. Thus

(e14)
$$J_e = J_{ne} + J_{re} + J_{pe}$$

By definition, the positive direction of the base current density J_b is into the transistor. Inside the base region the current components relevant to the base electrode current density J_b are (1) flow of holes that are back-injected from base region across the emitter-base junction J_{pe}, (2) flow of holes that recombine with electrons inside the emitter-base depletion region J_{re}, and (3) flow of holes that recombine with electrons inside the neutral base region J_r. Spontaneous charge carrier generation inside the reverse biased base-collector depletion region may occur, which leads to (4) hole generation current J_{gC} towards base from the depletion region. This hole current substracts from the total base hole current needed to balance the flow of holes consumed in recombination events. J_{ncb} and J_{pcb} represent electron and hole leakage currents across the reverse biased collector-base junction. These currents are very small in bias conditions of Figure f6, and are omitted here for simplicity. However, when the base-collector junction is forward biased, J_{ncb} and J_{pcb} play an important role and will be included in the terminal current calculations of chapter 2.10. Thus

(e15)
$$J_b = J_{pe} + J_{re} - J_{gC} + J_r .$$

The back-injected hole current density J_{pe} usually dominates over the rest of the base current components.

By definition, the direction of the collector current density J_c is towards the transistor. Inside the transistor the current components for J_c are (1) flow of electrons that originate from emitter and have survived the travel without recombination, and (2) flow of electrons that have been spontaneously generated inside the reverse biased base-collector region. Thus

(e16)
$$J_c = J_{nE} - J_r + J_{gC}.$$

The large signal current gain β of a transistor is defined as the ratio of the collector current I_C and base current I_B [29]. With equal areas of emitter, base and collector

(e17)
$$\beta = \frac{I_C}{I_B} = \frac{J_{ne} - J_r + J_{gC}}{J_{pe} + J_{re} + J_r - J_{gC}} < \frac{J_{ne} + J_{gC}}{J_{pe} - J_{gC}}.$$

This is the large signal current gain of the transistor. Small signal current gain is obtained by dividing the differential increase of I_c with respective differential increase in I_b. J_{gC} is a weak function of base-collector voltage, and may be neglected in the calculation. It is seen from the formula that the gain is maximized when the back injected hole current across emitter-base junction is minimized.

2.4 Abrupt Heterojunction under thermal equilibrium

The equations governing electrical behaviour of the emitter-base heterojunction are crucial in calculations of the analytical equations for transistor electrode currents. To have the convenience of associating numerical values for the relevant parameters for illustrative purposes, the case of an abrupt heterojunction of n-type $Al_{0,3}Ga_{0,7}As$ and p-type GaAs is chosen here. The energy band diagram of the structure in thermal equilibrium is given in Figure f7. The depletion region with its immobile space charge that originates from the ionized dopant atoms is also included, as is the respective electrical field. X1 is the depletion region edge in base side, and X2 is the emitter side depletion region edge. X_{je} represents the metallurgical junction. The rest of the variables are defined as they occur in the analysis of the structure.

To verify that the picture may be correct, a hypothetical experiment can be carried out.

In a infinite bar of intrinsic GaAs in thermal equilibrium at temperature of 300K the Fermi level resides approximately in the middle of the forbidden band gap. Carrier concentrations n and p equal the intrinsic carrier concentration n_i or $2{,}6 \cdot 10^6$ cm^{-3} throughout the bar. Then, half of the bar is changed for intrinsic $Al_{0,3}Ga_{0,7}As$ without breaking the crystal periodicity on the junction. On the junction, the conduction band and valence band would be discontinuous, with an amount given in equation (e13). Far apart from junction the Fermi level still resides around the middle of the band gap. For $Al_{0,3}Ga_{0,7}As$ the intrinsic carrier concentration is about $1{,}7 \cdot 10^3$ cm^{-3}. Initially, the free electrons in AlGaAs-side of the junction see the lower Fermi level of GaAs and jump over the junction. The electron leaves a positively charged immobile crystal ion behind, and after recombining with a hole in the GaAs side another, negatively charged immobile ion is formed. The immobile ions constitute an electrical dipole with electric field that points from AlGaAs towards GaAs.

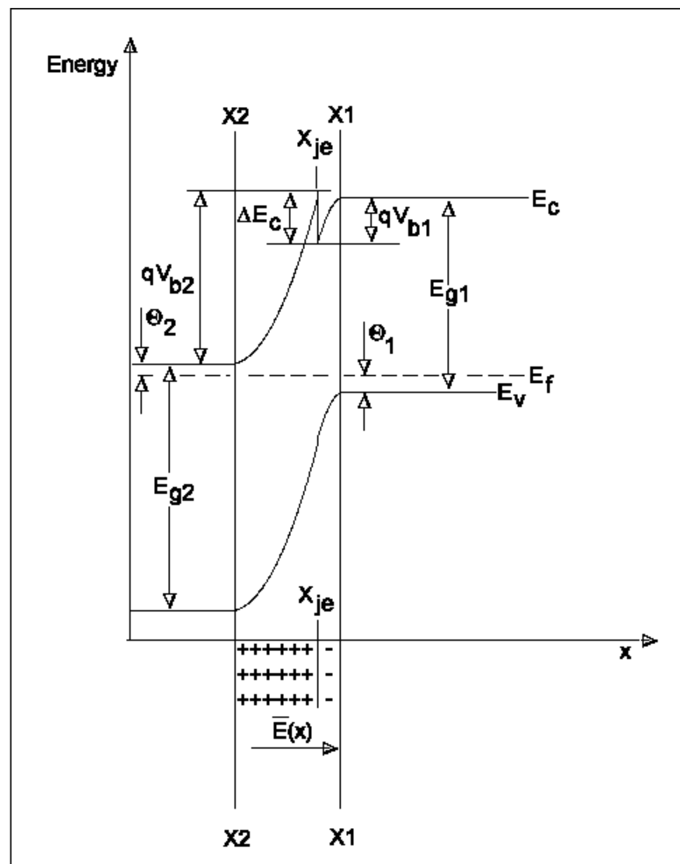

Figure f7: The energy band diagram of an abrupt heterojunction of n-type $Al_{0,3}Ga_{0,7}As$ and p-type GaAs in thermal equilibrium.

The direction of the field is such that it repels electrons from further movement across the junction. The movement of electrons continue until the cumulative repulsive force of the space charge region is strong enough to maintain an equilibrium. When the equilibrium is reached, Fermi level would be constant all over the bar.

The physics that governs over the junction is represented by Poisson equation and the continuity of the electric flux *D(x)*. The Poisson equation relates the net positive charge concentration inside a unit volume of space to the electric field strength that is present over the same volume of space. In one dimension, the Poisson equation is

(e18) $$\frac{dF}{dx} = \frac{q}{\varepsilon_s}(p - n + N^+ - N^-),$$

where $F = F(x)$ is the electric field strength, q is the magnitude of the electron charge, ε_s is the permittivity of the material, p is the concentration of free holes, n is the concentration of free electrons, N^+ is the concentration of the positive immobile ions, and N^- is the concentration of the negative immobile ions. The electric flux density *D(x)* is defined as

(e19) $$D(x) = \varepsilon_s F(x).$$

The intrinsic GaAs/AlGaAs heterojunction would have a depletion region of width *W=X2-X1,* that would be the sum of depletion widths in either sides of the junction. The potential *V(x)* between a potential reference point and the point of observation is obtained by integrating the electric field over the distance between the points. The potential increases when the direction of integration is against the electric field. If the potential reference point is put to the GaAs-side of the depletion region with coordinate origin set to point $x = X_{je} = 0$, or $V(-X_1)=0$, , the potential of AlGaAs is

(e20) $$V(X2) = -\int_{-X1}^{X2} F(x)dx.$$

This is the build-in potential V_{bi} of the junction that is needed to balance over the difference between the Fermi levels in either sides of the junction. From Figure f7

(e21) $$V_{bi} = V(X2) = V_{b1} + V_{b2} = \frac{E_{g1} + \Delta E_c - \Theta 1 - \Theta 2}{q},$$

where V_{b1} is the potential over the GaAs depletion layer, V_{b2} is the potential over the AlGaAs depletion layer, θ_1 is the energy difference between the Fermi level and GaAs valence band edge, and θ_2 is the energy difference between AlGaAs conduction band edge and the Fermi level. Taking into account that there is no other charge in the depletion regions but the immobile ions with concentrations on n_{i1} on GaAs side, and n_{i2} on AlGaAs side of the junction, the Poisson equation reduces to

(e22) $$\frac{dF}{dx} = -\frac{q}{\varepsilon_{s1}} n_{i1} \qquad [-X1 < x < 0]$$
$$\frac{dF}{dx} = \frac{q}{\varepsilon_{s2}} n_{i2} \qquad [0 < x < X2].$$

The electric field is then for GaAs-side of the junction where [-X1<x<0],

(e23) $$F(x) = \int_{-X1}^{x} \left(-\frac{q}{\varepsilon_{s1}} n_{i1} \right) dx = -\frac{q}{\varepsilon_{s1}} n_{i1} \left(x + X1 \right).$$

For AlGaAs-side of the junction where [0<x<X2],

(e24) $$F(x) = F(0^+) + \int_{0}^{x} \left(\frac{q}{\varepsilon_{s2}} n_{i2} \right) dx = F(0^+) + \frac{q}{\varepsilon_{s2}} n_{i2} x,$$

where $F(0^+)$ is the electric field in the AlGaAs side of the metallurgical junction. The continuity of the electric flux density $D(x)$ at the junction dictates that

(e25) $$D(0^-) = \varepsilon_{s1} F(0^-) = D(0^+) = \varepsilon_{s2} F(0^+).$$

Substituting $F(0^+)$ from equation (e23) it is found that

(e26) $$F\left(0^{+}\right)=-\frac{q}{\varepsilon_{s2}}n_{i1}X1,$$

which after substitution into equation (e24) gives for [0<x<X2]

(e27) $$F(x)=-\frac{q}{\varepsilon_{s2}}\left(n_{i1}X1-n_{i2}x\right).$$

At the depletion region edge X2 the electric field *F(X2)* is zero. This underscores the charge conservation relationship over the depletion region,

(e28) $$n_{i1}X1=n_{i2}X2,$$

and gives for [0<x<X2]

(e29) $$F(x)=-\frac{qn_{i2}}{\varepsilon_{s2}}\left(X2-x\right).$$

The potential *V(x)* can now be calculated by integrating the electric field over the depletion layer. For GaAs side [-X1<x<0] with the boundary condition that *V(-X1)*=0,

(e30) $$V(x)=-\int_{-X1}^{x}\left(-\frac{q}{\varepsilon_{s1}}n_{i1}\left(x+X1\right)\right)=\frac{q}{2\varepsilon_{s1}}n_{i1}\left(x+X1\right)^{2}.$$

The potential over GaAs side depletion region obeys parabolic curvature. The potential at the junction is

(e31) $$V_{b1}=V\left(x=0^{-}\right)=\frac{q}{2\varepsilon_{s1}}n_{i1}X1^{2}.$$

Similarly, after taking into account that potential is continuous at the junction, potential over AlGaAs [0<x<X2] is

(e32) $$V(x)=V_{b1}-\int_{0}^{x}\left(-\frac{qn_{i2}}{\varepsilon_{s2}}\left(X2-x\right)\right)dx=V_{b1}+\frac{qn_{i2}}{\varepsilon_{s2}}\left(X2x-\frac{x^{2}}{2}\right)$$

The build-in potential over the depletion region is thus

(e33)
$$V_{bi} = V(x = X2) = V_{b1} + V_{b2} = \frac{q}{2\varepsilon_{s1}} n_{i1} X1^2 + \frac{q}{2\varepsilon_{s2}} n_{i2} X2^2.$$

The unknown depletion region widths X1 and X2 can be solved by taking the ratio of V_{b1} and V_{b2} and substituting the charge conservation equation (e28) to get

(e34)
$$\frac{V_{b2}}{V_{b1}} = \frac{\varepsilon_{s1} n_{i2} X2^2}{\varepsilon_{s2} n_{i1} X1^2} = \frac{n_{i1}\varepsilon_{s1}}{n_{i2}\varepsilon_{s2}}$$

which is then substituted to the equation (e33) of V_{bi},

(e35)
$$V_{bi} = \left(1 + \frac{V_{b2}}{V_{b1}}\right) V_{b1} = \left(1 + \frac{n_{i1}\varepsilon_{s1}}{n_{i2}\varepsilon_{s2}}\right) V_{b1}.$$

Equation (e21) relates the build-in potential to the Fermi levels $\theta 1$ and $\theta 2$. Equations (e9) and (e10) relate the Fermi levels to free electron and hole concentrations. For $\theta 1 = E_f - E_v$ in GaAs neutral region the numerical values of $p = n_{i1} = 2{,}6 \cdot 10^6 \text{cm}^{-3}$ and $N_v = 7 \cdot 10^{18} \text{cm}^{-3}$ give from equation (e10) θ_1=0,74 eV. For $\theta_2 = E_c - E_f$ in AlGaAs neutral region the numerical value of n equals $n_{i2} = 1{,}7 \cdot 10^3 \text{cm}^{-3}$. To determine a numerical value of effective density of states N_c for $Al_xGa_{1-x}As$ conduction band, the effective electron mass m_{de} has to be known in equation (e4). For material with AlAs mole fraction x below 0,45, the effective electron mass $m_{de} = m_{de}(\text{x})$ is [r14]

(e36)
$$m_{de}(x) = (0.067 + 0.083x)m_0,$$

where m_0 is the free electron mass. For $Al_{0,3}Ga_{0,7}As$ the numerical value of N_c from equation (e4) is then $N_c = 7 \cdot 10^{17} \text{cm}^{-3}$. From equation (e9), Fermi level position in the neutral region of AlGaAs is θ_2 = 0,87 eV. The conduction band discontinuity ΔE_c for equation (e21) is found from equation (e13), and is ΔE_c = 0,2091 eV. The forbidden energy bang gap width of GaAs in room temperature is E_{g1} = 1,424 eV, and the AlGaAs forbidden energy bang gap width from equation (e13) is then E_{g2} = 1,798 eV. Substituting the numerical values to equation (e21) the build in potential V_{bi} of an intrinsic $Al_{0,3}Ga_{0,7}As$/GaAs heterostructure is 23,82 mV. To get V_{b1} from equation (e35)

the permittivities ε_{s1} and ε_{s2} need to be known. For GaAs, ε_{s1} is 13,18$\cdot$ ε_0, where ε_0 is the permittivity of vacuum. For $Al_xGa_{1-x}As$ the permittivity varies approximately linearly with x [r14],

(e37) $$\varepsilon_{s2} = (13{,}18 - 3{,}12x)\cdot \varepsilon_0, \qquad 0 \le x \le 1{,}0$$

which for x=0,3 gives ε_{s2} = 12,24$\cdot$ ε_0. Equation (e35) gives then V_{b1} = 14,46μV. Practically all of the build-in potential is over the AlGaAs depletion layer. The depletion region widths as obtained from equation (e33) are $X1$ = 90 μm and $X2$ = 0,137 meters. It is seen from equation (e28) that $X1$ and $X2$ conserve the total charge across the depletion region of the junction.

The hypothetical GaAs/AlGaAs bar is now ready to be doped with impurities in order to create a pn-heterojunction. Dopant atoms are thus being supplied uniformly into the two bar halves in a way that GaAs gets carbon atoms that are p-type dopants or acceptors, and AlGaAs gets silicon atoms that are n-type dopants or donors. The doping atoms are such that in normal operation temperatures practically all of the dopant atoms are ionized so that added hole concentration p will be approximately equal to carbon doping concentration N_A, and added electron concentration n will be approximately equal to silicon doping concentration N_D.

Excess electrons are thus introduced in AlGaAs and excess holes into GaAs. In AlGaAs side the Fermi level starts to drift upwards in energy, and in GaAs side downwards in energy. In the vicinity of the junction the excess electrons in AlGaAs see again the lower Fermi level on GaAs side and wish to fill the holes in GaAs side. In every movement of electron, a positive and immobile space charge is formed in the AlGaAs side and negative and immobile space charge is formed in the GaAs side. The space charges continue forming electrical dipoles that cumulative strengthen the electric field across the junction.

As the typical doping levels are several orders of magnitude higher than intrinsic concentrations, the intentional doping soon dominates the electrical behaviour of the material at room temperature. The field direction is still from AlGaAs towards GaAs representing a repulsive force against further movement of electrons. Depending on the doping levels, more or less electrons move across the junction until equilibrium is again formed by the repulsive electric field of the space charge dipole. At equilibrium, the Fermi level is again constant throughout the structure. The calculations that were done for an intrinsic heterosructure can now be repeated, taking into account that the immobile space charge now consitutes almost entirely by the ionized dopant atoms. If the doping consentrations exceed the validity limit of the Boltzmann equation (e9) and (e10), the Joyce-Dixon approximation of equation (e7) and (e8) should be used.

With doping concentrations of $N_A = 1 \cdot 10^{19} cm^{-3}$ and $N_D = 1 \cdot 10^{17} cm^{-3}$ the Fermi level positions accroding to equations (e7) and (e8) are $\Theta_2 = +48,948$ *meV* and $\Theta_1 = -22,019$ *meV.* The negative Fermi level position indicates that Fermi level is now below valence band edge in p-doped GaAs. From equation (e21) the built-in potential is found to be $V_{bi} = 1,606$ V. Potential across GaAs side of the junction is from equation (e35) $V_{b1} =$ 14,78 mV, and the GaAs-side depletion region width from equation (e31) is $X1 = 14,67$ Å. For AlGaAs, the calculation gives $V_{b2} = 1,59136$ V, and $X2 = 14,67$ µm. Again, the total charge is conserved. The huge difference in doping levels make the junction practically one sided. Schematically, the energy band diagram looks like that of Figure f7, although the narrow depletion region in GaAs side would not be visible.

2.5 AlGaAs / GaAs –Heterojunction Under Applied Voltage

The heterojunction of Figure f7 forms a diode structure. If external voltage V_A is applied such that GaAs is forced more positive than AlGaAs, the thermal equilibrium is disturbed as illustrated in Figure f8. The applied potential difference is seen by the junction as a shift between Fermi levels in each side of the depletion region. In AlGaAs-side the level shifts upwards in energy, and in GaAs-side downwards.

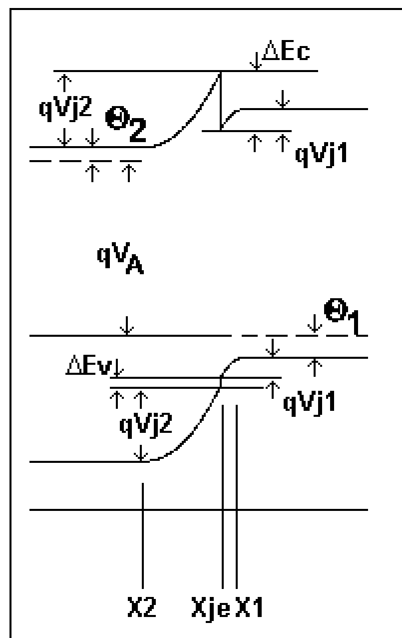

Figure f8: Heterojunction under applied voltage.

The overall potential V_j across the junction is now

(e38) $$V_j = V_{bi} - V_A = V_{j1} + V_{j2},$$

where V_{j1} is the potential over GaAs-side depletion layer, and V_{j2} is the potential over AlGaAs-side depletion layer. Again, the electrons in AlGaAs wish to jump over the

junction to reach the lower Fermi level region. For every electron that leaves AlGaAs, an electron is supplied by the negative terminal of the voltage supply that is connected to the AlGaAs side of the diode. In GaAs side, the electron recombines with a hole, which is then replaced by another hole that is generated by an electron leaving the bar to the positive terminal of the voltage supply, that is connected to the GaAs side of the diode. Electrical current flows through the diode indicating that the diode is forward biased. If the polarity of the voltage supply is reversed, the Fermi level in AlGaAs shifts downwards, and upwards in GaAs. The potential V_j would increase by an amount of V_A.

The applied potential V_A is shared between the junction sides such that

(e39)
$$\begin{aligned} V_{j1} &= V_{b1} - V_{A1} \\ V_{j2} &= V_{b2} - V_{A2} \\ V_A &= V_{A1} + V_{A2} \\ V_{bi} &= V_{b1} + V_{b2}, \end{aligned}$$

where V_{A1} is the portion of applied voltage V_A over GaAs-side depletion region and V_{A2} is the portion of applied voltage over AlGaAs-side depletion region. $V_{bi} = V_{b1} + V_{b2}$ is the build-in potential of the junction under thermal equilibrium. Equation (e35) can now be rewritten in applied bias condition

(e40)
$$V_j = V_{bi} - V_A = \left(1 + \frac{n_{i1}\varepsilon_{s1}}{n_{i2}\varepsilon_{s2}}\right)V_{j1}.$$

Equation (e33) under applied bias is

(e41)
$$V_j = V_{j1} + V_{j2} = (V_{b1} - V_{A1}) + (V_{b2} - V_{A2}) = \frac{qn_{s1}X1^2}{2\varepsilon_{s1}} + \frac{qn_{s2}X2^2}{2\varepsilon_{s2}}.$$

It is seen from equation (e41) that when forward applied voltage equals V_{bi} the depletion region width goes zero. At that point, the energy band diagram of the junction is flat as there is no space charge present. Band edges and the Fermi level then alter stepwise at the metallurgical junction.

2.6 Current through abrupt AlGaAs / GaAs –Heterojunction

The discontinuities of energy bands in an abrupt AlGaAs/GaAs -heterojunction serve as potential barriers against charge carrier movement across the junction. The discontinuity of valence band ΔE_v impedes hole injection from GaAs to AlGaAs. The conduction band spike ΔE_c impedes electron injection from AlGaAs to GaAs. From equation (e17) it was seen that transistor current gain β depends on the ratio of injected electrons and back-injected holes. It is customary to characterize the transistor emitter function by "emitter efficiency" γ,

(e42) $$\gamma = \frac{\text{emitted electron current density}}{\text{emitted electron current density} + \text{emitted hole current density}}.$$

The valence band discontinuity improves emitter efficiency by reducing back-injection of holes. The conduction band discontinuity is more problematic. While the spike reduces electron current and emitter efficiency it filters the electrons in energy such that there is a considerable portion of high energy electrons included in the electron flow [r48]. The high energy electrons are those that have enough energy to surmount the spike from AlGaAs to GaAs. The excess energy is kinetic, and the base transit time is smaller than with electrons at the edge of the conduction band. The transistor can thus operate faster. For applications where high energy electron emission is not important, the AlGaAs/GaAs junction is spatially graded, such that the AlAs mole fraction x is altered gradually over a distance instead of having an abrupt profile. In a properly graded junction the conduction band spike is absent, and the structure resembles a homojunction with the exception of having different band gaps.

The generation of high energy electrons in an abrupt heterojunction is an example of "thermionic emission". It is the solid state counterpart of the electron tube triode emitter function. Additionally, quantum mechanics gives the electrons behind the spike yet another way to reach the GaAs side. The potential spike is thin enough to allow the electron to have a finite probability to tunnel through the potential barrier. With

approximately triangular shape of the spike there is always tunneling present to some extent. The flow of electrons that tunnel through the spike constitute "field emission" current across the junction. The emission modes are illustrated in Figure f9. Also included in the figure are recombination currents that arise from recombination in the depletion region and in the neutral region of AlGaAs. The total emitter current is a sum of recombination currents and the combination of thermionic and field emission currents.

Figure f9 has some similarity to the ideal metal-semiconductor Schottky-junction of Figure f11. If the p-side was heavily doped almost all of the junction voltage is across the AlGaAs depletion region. This allows to estimate the heterojunction thermionic emission current with an analogy to the analysis of a Schottky junction. The Schottky barrier height ϕ_B is defined as the separation of the metal Fermi level and the edge of the conduction band spike. The current density from the flow of electrons from semiconductor to metal with the ideal Schottky junction J_{sm} is [r13]

(e43) $$J_{sm} = A^* T^2 e^{\frac{-q\phi_B}{kT}} e^{\frac{qV_A}{kT}},$$

where ϕ_B is in electron volts, V_A is the applied bias voltage and A^* is the effective Richardson constant

(e44) $$A^* = \frac{4\pi q m_e^* k^2}{h^3}.$$

Here m_e^* is the "conductivity" effective electron mass. At zero bias J_{sm} has a value that balances against the current flow from metal to semiconductor such that net current is zero. With the heterojunction of Figure f9 the Schottky barrier height ϕ_B is replaced by ϕ_B^*, or the Fermi level separation from the edge of the conduction band spike in AlGaAs side,

(e45) $$\phi_B^* = qV_{b2} + \Theta_2,$$

where V_{b2} is the portion of the built-in potential V_{bi} that is over AlGaAs-side depletion layer and θ_2 is the energy difference between AlGaAs conduction band edge and the Fermi level.

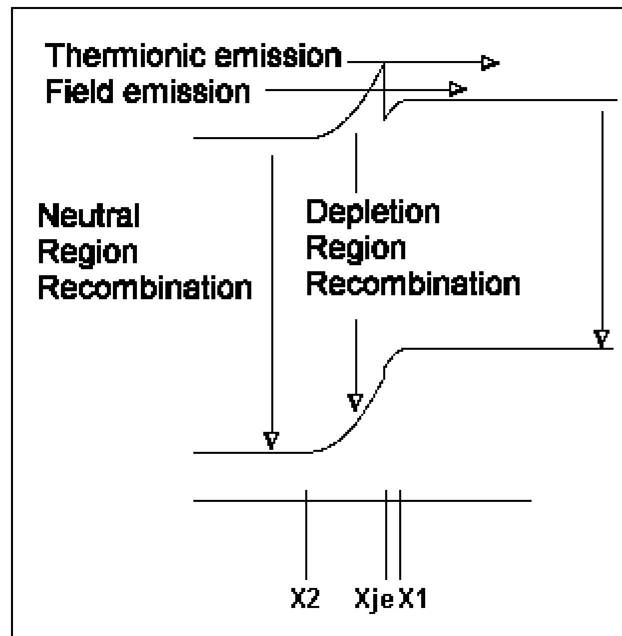

Figure f9: Emission modes and recombination currents of a heterojunction barrier.

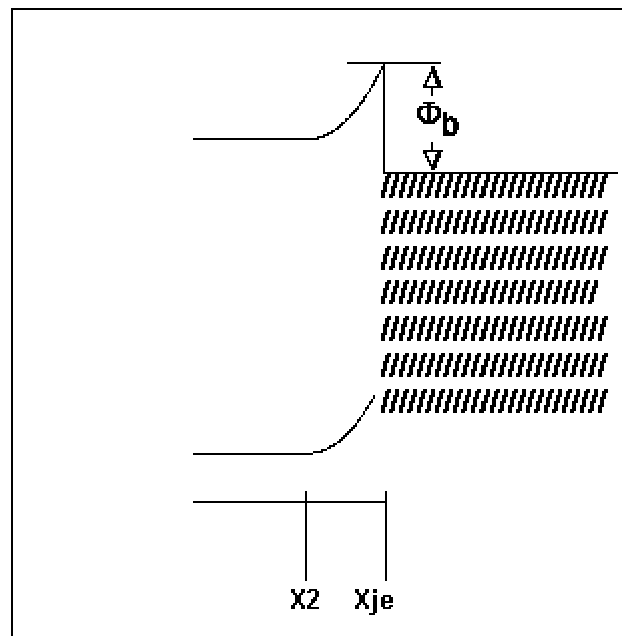

Figure f11: Ideal metal-semiconductor Schottky-junction.

The potential over Schottky junction V_A is replaced by the potential drop over AlGaAs V_{j2}. Replacing intrinsic concentrations with intentional doping concentrations N_A and N_D in equations (e34) and (e35), and using equation (e21) ϕ_B^* would be

(e46)
$$\phi_B^* = \frac{E_{g1} + \Delta E_c + K\Theta_2 - \Theta 1}{1+K},$$

where

(e47)
$$K = \frac{\varepsilon_{s2} N_D}{\varepsilon_{s1} N_A}.$$

The equation for V_{j2} from equation (e40), after replacing intrinsic concentrations with intentional doping concentrations N_A and N_D, is then

(e48)
$$V_{j2} = \frac{V_{j1}}{K} = \frac{V_j}{1+K}.$$

The equation for thermionic emission current density from the flow of electrons from AlGaAs to GaAs with an abrupt heterojunction and heavy p-doping is then

(e49)
$$J_{21}^* = A^* T^2 e^{-\frac{1}{kT}\left(\frac{E_{g1} + \Delta E_c + K\Theta_2 - \Theta 1}{1+K}\right)} e^{-\frac{q}{kT}\frac{V_j}{1+K}}.$$

At zero bias the electron current J_{21}^* balances the current J_{12}^* which flows from GaAs to AlGaAs. The total current density across the junction would be the sum of the current flows J_{21}^* and J_{12}^*, or

(e50)
$$J_{\text{thermionic emission}}^* = A^* T^2 e^{-\frac{1}{kT}\left(\frac{E_{g1} + \Delta E_c + K\Theta_2 - \Theta 1}{1+K}\right)} \left(e^{-\frac{q}{kT}\frac{V_j}{1+K}} - 1 \right)$$

It has to be kept in mind that the ideal Schottky junction current equation (e43) is derived under the following assumptions [r13]:
1) Schottky barrier height is much larger than kT
2) Thermal equilibrium is established at the plane that determines emission
3) The existence of a net current flow does not affect this equilibrium, so that the opposite current fluxes can be superimposed.

The collector current density J_C of a transistor with graded heterojunction emitter is limited by the electron diffusion through the neutral base. If the heterojunction was abrupt, the picture includes high energy, high velocity electrons in base that have either tunneled through the spike or had enough energy to surmount it completely. In this case the collector current density is not entirely related to the diffusion properties in the base. Only if the height of the conduction band spike was small enough such that the electrons loose their excess kinetic energy completely far before they reach the collector, the transistor collector current is again limited by the diffusion of electrons with energies at the conduction band edge level.

2.7 Current through graded AlGaAs / GaAs –Heterojunction

In a graded heterojunction the electron flow across the depletion region is not affected by a potential spike. The ideal current equation follows that of Shockley equation of a pn-homojunction [r13]. After taking into account that the material type changes from GaAs to AlGaAs at the junction altering the intrinsic carrier density n_i and therefore minority carrier concentrations at thermal equilibrium p_{n0} and n_{p0}, the Shockley equation for a graded, long heterojunction diode structure reads

(e51) $$J_{Shockley} = \left(\frac{qD_p}{L_p} \frac{n_{i2}^2}{N_D} + \frac{qD_n}{L_n} \frac{n_{i1}^2}{N_A} \right) \left(e^{\frac{qV_j}{kT}} - 1 \right)$$

Here n_{i1} is intrinsic carrier density in GaAs, n_{i2} is intrinsic carrier density in AlGaAs, D_p is the hole diffusion coefficient in n-type AlGaAs, D_n is the electron diffusion coefficient in p-type GaAs, L_p is the hole diffusion length in n-type AlGaAs, and L_n is the electron diffusion length in p-type GaAs.

By definition, the diffusion coefficient and diffusion length is bound together by the minority carrier lifetime τ,

(e52) $$\tau_{p,n} = \frac{L_{p,n}^2}{D_{p,n}}.$$

A long diode structure is such that the diode extends over three times the diffusion length in either direction away from the metallurgical junction. If the diode is short, the diffusion lengths in equation (e51) are replaced by the neutral region thicknesses of either side. If X_E is the thickness n-AlGaAs layer and X_B is the thickness p-GaAs layer, the equation for a graded, short heterojunction diode would be

(e53) $$J_{Shockley} = \left(\frac{qD_p}{(X_E - X2)} \frac{n_{i2}^2}{N_D} + \frac{qD_n}{(X_B - X1)} \frac{n_{i1}^2}{N_A} \right) \left(e^{\frac{qV_j}{kT}} - 1 \right)$$

2.8 Transistor Base Layer as a Charge Storage

Estimates on transistor terminal currents can be calculated by treating the base neutral region as a storage volume of minority carrier charge. The storage is being filled on emitter side by electron emission, and dynamic equilibrium is maintained by electrons escaping the storage to collector side. Some electron are lost from the storage by recombination processes that adds to total base current. Across the storage a gradient in minority carrier concentration has to be present such that there is more electrons in emitter side than in collector side of the storage volume.

The gradient of minority carrier concentration of electrons *n(x)* induces diffusion of electrons in p-type GaAs base. The current density J_n from diffusion of electrons is

(e54) $$J_n = qD_n \frac{dn(x)}{dx},$$

where q is the magnitude of electron charge and D_n is the electron diffusion coefficient in p-type GaAs. Because the concentration gradient decreases towards collector, the direction of the diffusion current density J_n is towards emitter. Under steady state

condition the net electron concentration inside an infinitesimal volume element of width dx is constant in time. If there was any recombination event inside the volume element, not all of the incoming electrons reach the collector side. The portion of electron flow that does not come out at collector side of the volume element is

(e55) $$dJ_n(x) = J_n(x) - J_n(x+dx) = qD_n\left(\frac{dn(x)}{dx} - \frac{dn(x+dx)}{dx}\right),$$

which equals the electron flow into recombination events.

The minority carrier recombination lifetime τ is defined as the average time that is needed by a volume element with excess minority carriers to reach again the equilibrium by recombination. The recombination rate U measures the average recombination process in [$cm^{-3}s^{-1}$]. For electrons in p-type GaAs

(e56) $$U(x) = \frac{n(x) - n_0}{\tau_n}.$$

where n_0 is the minority electron concentration in p-type GaAs at thermal equilibrium. In steady state the current density from recombinations inside the volume element balances the diffusion current loss giving

(e57) $$qU(x) = \frac{dJ_n(x)}{dx} \Leftrightarrow \frac{n(x) - n_0}{\tau_n} = D_n\frac{d^2n(x)}{dx^2}.$$

In order to solve n(x) boundary conditions have to be set. Let the neutral base layer be limited by the emitter-base depletion region edge at $x = 0^+$ and the base-collector depletion region edge at $x = X_c^-$. Assuming a graded heterojunction the pn-junction law of equation (e2) should hold, and

(e58) $$n(0^+) = n_{0b} e^{\frac{qV_{je}}{kT}} = \frac{n_{i1}^2}{N_A} e^{\frac{qV_{je}}{kT}},$$

where V_{je} is the potential difference of the base and emitter neutral regions that approximately equals base-emitter voltage V_{BE}, and n_{0b} is the minority electron concentration in base at thermal equilibrium. On collector side the pn-junction law reads

(e59) $$n(X_c^-) = n_{0b} e^{\frac{qV_{jc}}{kT}} = \frac{n_{i1}^2}{N_A} e^{\frac{qV_{jc}}{kT}},$$

where V_{jc} is the potential difference of the base and collector neutral regions that approximately equals base-collector voltage V_{BC}.

With a heavily doped base the thermal equilibrium electron concentration n_{0b} is very low. With $N_A = 1 \cdot 10^{19}\text{cm}^{-3}$ and $n_{i1} = 2,6 \cdot 10^6\text{cm}^{-3}$ $n_{0b} = 6,76 \cdot 10^{-7}\text{cm}^{-3}$. For a transistor operating in forward active mode $V_{je} > 0$V and $V_{jc} < 0$V. With $V_{je} = 1$ V and $V_{jc} = -1$ V $n(0^+) = 4,3 \cdot 10^{10}\text{cm}^{-3}$ and $n(X_c^-) = 1,1 \cdot 10^{-23}\text{ cm}^{-3}$, which is practically zero.

A very simple formula for the the diffusion current density J_n across the base can be derived if it is postulated that the minority electron concentration $n(x)$ across the neutral base layer of a transistor biased into forward active mode is always much more than the thermal equilibrium value n_{0b}. With equation (e52) equation (e57) would then reduce to

(e60) $$\frac{d^2 n(x)}{dx^2} - \frac{n(x)}{L_n^2} = 0.$$

The solution for $n(x)$ that satisfies boundary conditions of equation (e58) and $n(X_c^-)=0$ is

$$n(x)=\frac{n(0^+)}{e^{\frac{W_{base}}{L_n}}-e^{-\frac{W_{base}}{L_n}}}\left[e^{\frac{W_{base}-x}{L_n}}-e^{-\frac{W_{base}-x}{L_n}}\right], \tag{e61}$$

where $W_{base} = X_c^- - 0^+$ is the thickness of the neutral base region. With small values of z the exponential function e^z is approximately equal to 1+z. It is seen from equation (e61) that the equation of $n(x)$ when $W_{base} << L_n$ reduces further to

$$n(x)\approx n(0^+)\left[1-\frac{x}{W_{base}}\right]. \tag{e62}$$

The electron concentration has a linear dependence on the distance from the emitter side of the neutral base, and goes zero at the collector side of the neutral base. From (e54) the current density from diffusion of electrons across the base is then constant over the base. The collector current density from diffusion of electrons across the base $J_{c,diff}$ would then be

$$J_{c,diff}=qD_n\left.\frac{dn(x)}{dx}\right|_{x=X_c^-}=qD_n\frac{n(0^+)}{W_{base}}=\frac{qD_n}{W_{base}}\frac{n_{i1}^2}{N_A}e^{\frac{qV_{je}}{kT}}. \tag{e63}$$

The necessary condition for equation (e63) to hold is that $W_{base} << L_n$. Typical values for recombination lifetime and diffusion coefficient of electrons in heavily doped p-GaAs are τ_n ~ 1 ns and D_n ~25 cm^2s^{-1}, giving diffusion length L_n of about 1,5 μm. Typical base thicknesses are around 0,1 μm or less, indicating that equation (e63) is applicable.

What was also assumed was that the heterojunction was graded, and the pn-junction law gives the minority carrier concentration at the emitter side of the neutral region of base. With abrupt heterojunctions the electron concentration is determined by the combination of thermal and field emission. In that case the derivation of collector current equation is somewhat more involved, giving for the total collector current J_C [r14]

(e64) $$J_C = J_0 e^{\frac{qV_{je}}{(1+K)E_{00}\coth\left(\frac{E_{00}}{kT}\right)}}\left[1-e^{-\frac{qV_{je}}{kT}}\right],$$

where J_0 is a constant and

$$E_{00} = \frac{qh}{4\pi}\sqrt{\frac{N_D}{m_e^* \varepsilon_{s2}}}.$$

There was many approximations involved with equation (e61). In reality, the carrier concentration at the collector depletion region edge is far from zero when the transistor is biased to forward active mode. The current density through base-collector junction should be continuous. After reaching the base-collector depletion region the electrons are accelerated by the strong electric field of the reverse biased junction until they achieve the saturation velocity v_s. The corresponding current density from electrons $J_{c,drift}$ would be [r51]

(e65) $$J_{c,drift} = qn_c v_s,$$

where n_c is the mobile electron concentration inside the base-collector depletion region. It was assumed with equation (e59) that under forward active mode the electron concentration at the collector side of the neutral base drops to practically zero. To maintain the current continuity, the approximation needs to be refined to give

(e66) $$n\left(X_c^-\right) = n\left(X_c^+\right) = n_c = \frac{J_{c,diff}}{qv_s}$$

With a typical value of $v_s = 1 \cdot 10^7$ cm/s and current density of 1kA/cm^2 $n_c \sim 6{,}2 \cdot 10^{14}$ cm^{-3}. With neutral base thickness of 1000Å and D_n = 25 cm^{2}s^{-1}, this would demand from equation (e63) that $n(0^+) = 2{,}5 \cdot 10^{15}$ cm^{-3}. With base doping of $N_A = 1 \cdot 10^{19}$cm^{-3} and n_{i1} = $2{,}6 \cdot 10^6$cm^{-3} the emitter-base bias potential should be V_{je} = 1,28 V.

To correct the picture of minority carrier concentration profile across the charge storage in order to maintain current continuity at x = X_c, equation (e62) may be rewritten as

(e67) $$n(x) \approx \left(n(0^+) - n_c\right)\left[1 - \frac{x}{W_{base}}\right] + n_c .$$

The total charge density Q of the base layer under forward active mode is obtained by integrating $n(x)$ over the neutral base and multiplying by electron charge q,

(e68) $$Q = q\int_0^{W_{base}} n(x)dx = \frac{q}{2}W_{base}\left[n(0^+) + n_c\right]$$

The definition of recombination lifetime of equation (e56) and equation (e68) gives the base current density from recombinations inside the neutral base J_r as

(e69) $$J_r = \frac{Q}{\tau_n}.$$

The base transit time τ_b of a charge carrier population is the time needed to drain the stored charge by the collector current,

(e70) $$\tau_b = \frac{Q}{J_{c,diff}} = \frac{W_{base}^2}{2D_n}\left(1 + \frac{n_c}{n(0^+)}\right) \approx \frac{W_{base}^2}{2D_n}.$$

For accurate characterization of the transistor behaviour equation (e57) need to be solved with more accurate boundary condition for $x = X_c$. It is common to rewrite the continuity equation (e57) for the excess charge carrier concentration $\Delta n = n(x) - n_o$, where n_o is the thermal equilibrium electron concentration in the base layer. Equation (e57) then reads

(e71) $$\frac{d^2\Delta n(x)}{dx^2} - \frac{\Delta n(x)}{L_n^2} = 0.$$

.

The solution for $\Delta n(x)$ that satisfies boundary conditions of equation (e58) and (e59) is

(e72)
$$\Delta \mathrm{n}(\mathrm{x}) = n(x) - n_0 = \frac{\Delta n(X_c^-)\sinh\left(\frac{x}{L_n}\right) - \Delta n(0^+)\sinh\left(\frac{x - X_c^-}{L_n}\right)}{\sinh\left(\frac{X_c^-}{L_n}\right)},$$

where $\Delta n(0^+) = n(0^+)\text{-}n_0$ and $\Delta n(X_c^-) = n(X_c^-)\text{-}n_0$.

2.9 Large Signal Current Gain of a Heterojunction Bipolar Transistor

The current gain of a transistor was introduced with equation (e17) as the ratio of collector and base currents. The gain was limited by the ratio of forward injected electrons to back-injected holes in the forward biased base-emitter junction. With a graded heterojunction emitter the flow of electrons and holes is limited by diffusion and Shockley equation of (e53) holds. With abrupt heterojunction the flow of electrons is not necessarily limited by diffusion because of the conduction band spike.

The flow of holes is not impeded by any spike but only a valence band difference of ΔE_V. Hole current is limited by diffusion and Shockley equation is valid, such that the back-injected hole current density in a short base-emitter diode in either type of heterojunction is

(e73)
$$J_p = \frac{qD_p}{(X_E - X_0^-)} \frac{n_{i2}^2}{N_D} e^{\frac{qV_{je}}{kT}} = \frac{qD_p}{W_{emitter}} \frac{n_{i2}^2}{N_D} e^{\frac{qV_{je}}{kT}},$$

where X_E is emitter contact, X_0^- is emitter side depletion region edge, $W_{emitter} = X_E - X_0^-$ is the thickness of the neutral emitter. Substituting (e73) and (e63) into (e17) gives for a graded heterojunction transistor

(e74) $$\beta \le \frac{D_n W_{emitter} N_D}{D_p W_{base} N_A} \frac{n_{i1}^2}{n_{i2}^2}.$$

The influence of a heterojunction emitter on transistor gain is clearly visible in equation (e74). In a homojunction transistor the intrinsic carrier concentrations are the same in either side of the base-emitter junction. The design of a homojunction transistor for optimum large signal gain includes maximizing the "DWN" product in the numerator of equation (e74) while minimizing the "DWN" product in the denominator. In the case of heterojunction the designer has additional freedom to manipulate the intrinsic carrier consentration ratio. From equation (e11) it is seen that n_i decreases exponentially as the forbidden band gap width E_g is increased. For GaAs the intrinsic concentration is n_{i1} = $2{,}6 \cdot 10^6 cm^{-3}$ and for $Al_{0,3}Ga_{0,7}As$ n_{i2} = $1{,}7 \cdot 10^3 cm^{-3}$. Assuming that equation (e74) gives the actual device gain accurately, and neglecting the small variations in other material parameters, the graded heterojunction boosts the transistor gain by a factor of $2 \cdot 10^6$. With abrupt heterojunction the conduction band spike makes the effect less dramatic by holding off the forward injected electrons, but high gain is still obtained even after heavy base doping N_A, that in homojunction case would not be practical.

2.10 Modeling of the transistor terminal currents

In order to give an analytical expression for the transistor electrode currents J_e , J_b and J_c of section 2.3, the electron and hole current densities into and out of different portions of the transistor need to be sorted out and summed properly. It is convenient to start the analysis by studying the net electron flow across base-emitter heterojunction of Figure f12 at point $x = 0$ such that emitter is left and base is right from the origin.

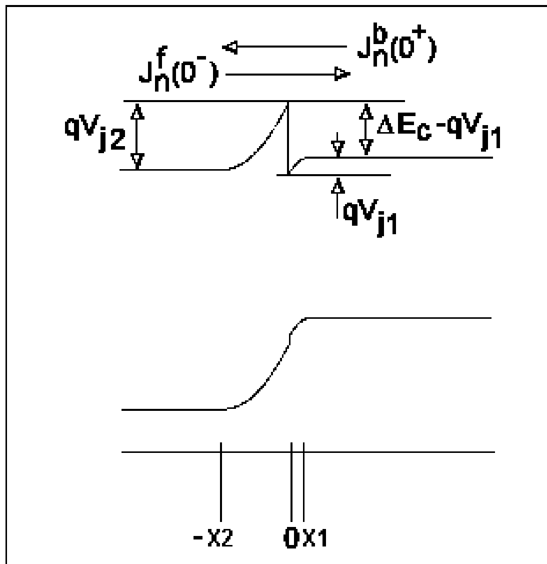

Figure f12: net electron flow across base-emitter heterojunction.

Exploiting again the Schottky-junction analogy, the maximum diffusion current that can be drawn from AlGaAs to GaAs, $J_n(0)$, can be modeled by Richardson-Dushman emission [r17]

(e75) $$J_n(0) = qn(0)v_n^*,$$

where $n(0)$ is electron concentration at the junction and v_n^* is the Richardson-Dushman velocity,

(e76) $$v_n^* = \frac{v_{th}}{\sqrt{6\pi}} = \frac{1}{\sqrt{6\pi}}\sqrt{\frac{8kT}{\pi m_{e1}^*}} = \sqrt{\frac{4kT}{3\pi m_{e1}^*}},$$

where the conductivity effective mass m_{e1}^* is that of GaAs-side. The total current $J_n(0)$ is a superposition of two opposite electron fluxes, $J_n^f(0^-)$ from AlGaAs to GaAs and $J_n^b(0^+)$ from GaAs to AlGaAs such that $J_n(0) = J_n^f(0^-) + J_n^b(0^+)$. Both fluxes are considered to be Richardson-Dushman currents of equation (e75). It is assumed that electron concentration at heterojunction obeys Maxwellian distribution in energy such that the concentration of electrons with energy equal to the tip level at the GaAs-side of the junction $n_{hot}(0^+)$ is found from the concentration of the electrons at conduction band edge level $n(0^+)$ by [r18]

(e77)
$$n_{hot}\left(0^+\right) = n\left(0^+\right)e^{-\frac{\Delta E_c}{kT}}.$$

The current density $J_n(0)$ is then

(e78)
$$J_n(0) = -\frac{qv_{th}}{\sqrt{6\pi}}\left\{n\left(0^-\right) - n\left(0^+\right)e^{-\frac{\Delta E_c}{kT}}\right\}.$$

For convenience, the negative sign of the current equation is visible to assure that $J_n(0)$ will have correct sign when compared with the diffusion current in the neutral base region in mechanical calculations below. This convention leads to transistor terminal current equations that give negative values for emitter and collector currents when the transistor is biased in forward active mode, indicating that the direction of the diffusion current is negative to the direction of decreasing concentration gradient of electrons. Current graphs are usually plotted with positive signs.

Equation (e78) counts only those electrons that have enough energy to surmount the potential barrier of the conduction band spike. Grinberg et al. [r19] introduced a thermionic-field-diffusion model for the heterojunction emitter to take into account the electron tunneling through the barrier by transparency D, that depends on the electron energy. The transparency of an arbitrary potential barrier is a quantum mechanical problem by nature. The exact solution of D needs to be calculated numerically, but in some special cases the transparency may be approximated by analytical formulas.

For a triangular potential barrier the transparency was found to be [r19]

(e79) $$D(X)=D_0(X)=e^{-\frac{E_{m,abrupt}}{E_{00}}\left[\sqrt{1-X}+\frac{1}{2}X\ln(X)-X\ln\left(1+\sqrt{1-X}\right)\right]},$$

where $E_{m,abrupt}$ is the potential energy difference of the conduction band tip level to the conduction band edge of neutral AlGaAs, or with abrupt heterojunction

$$E_{m,abrupt}=qV_{j2}$$

with V_{j2} from equation (e39). The energy reference E_{00} is

$$E_{00}=\frac{qh}{4\pi}\sqrt{\frac{N_D}{m_{e2}^*\varepsilon_{s2}}},$$

where the material parameters refer to GaAs-side. Unfortunately the square root sign with the equation of E_{00} was missing in the original article of [r19] and the printing error is not always recognized. The transparency D approaches unity as the junction bias voltage V_{je} approcahes built-in potential V_{bi} of the base-emitter junction making V_{j2} to approach zero. Also, when the argument X approaches unity, $D(X)$ approaches unity. The meaning of argument X will become apparent shortly. In mechanical calculations it will represent the ratio of the energy of incident electron to the upper energy boundary of integration.

The condution band spike vanishes with ideally graded heterojunctions. In practice, the grading is often only partial such that some of the spike is still effective. The transparency of a partially graded heterojunction is also possible to evaluate analytically in some special cases. If the grading layer is such that the AlAs mole fraction varies linearly over the grading layer of width W_{gr} while the doping is kept constant, the transparency D is [r19]

(e80) $$D(X) = D_0(X) e^{\left\{-\frac{E_{m,graded}}{E_{00}}\left[\sqrt{(1-X+f(X)(1-X))} - f(X)\ln\sqrt{\frac{1-X}{f(X)}+1}+\sqrt{\frac{1-X}{f(X)}}\right]\right\}},$$

where D_0 is the transparency if the junction was abrupt and

$$E_{m,graded} = \frac{q^2 N_A}{2\varepsilon_{s2}}\left(X2 - W_{gr}\right)^2,$$

$$f(X) = X + \frac{1}{4}\left(\frac{\Delta E_c}{E_m}\right)^2\left(\frac{X_2}{W_{gr}} - 1\right)^2 - \frac{\Delta E_c}{E_m}\left(\frac{X_2}{W_{gr}} - 1\right),$$

and *X2* is the thickness of the depletion region in AlGaAs-side, that is found from equations (e40) and (e41). The energy dependence of the transparency of an abrupt $Al_{0,3}Ga_{0,7}As$/GaAs heterojunction with 1V bias according to equation (e79) is shown in Figure f13.

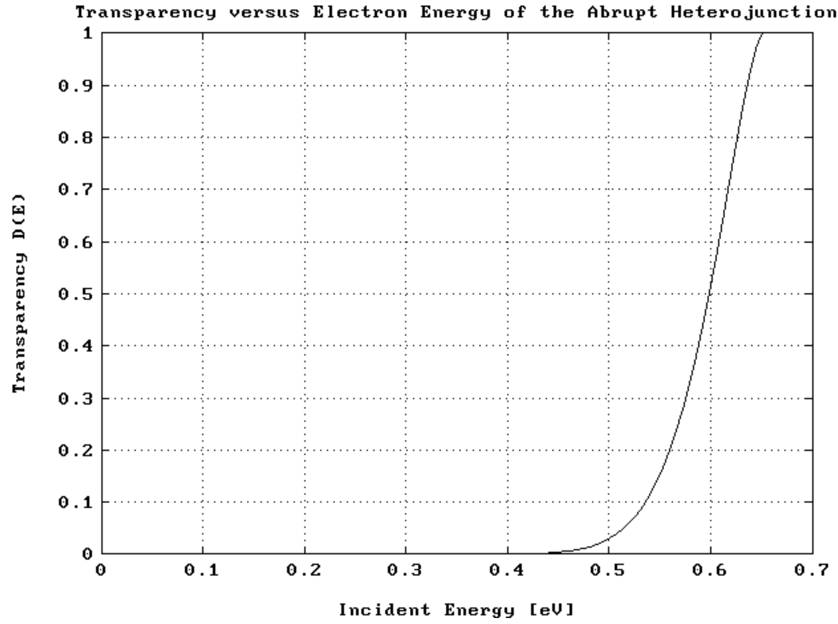

Figure f13: The energy dependence of the transparency of of an abrupt $Al_{0,3}Ga_{0,7}As$/GaAs heterojunction with 1V bias. Doping concentrations were was $N_e = 5\cdot10^{23}$ m^{-3}, $N_b = 1\cdot10^{25}$ m^{-3}, and $N_c = 4\cdot10^{22}$ m^{-3}. The calculation was based on equaiton (e79).

Taking into account the transparency of the conduction band spike, the equation (e78) for electron current from AlGaAs to GaAs is modified to [r19]

(e81) $$J_n(0) = -\frac{qv_{th}}{\sqrt{6\pi}}\left\{n(0^-) - n(0^+)e^{-\frac{\Delta E_c}{kT}}\right\}\gamma_n,$$

where the multiplying factor γ_n integrates together the electrons that leak through the barrier with different energies

$$\gamma_n = 1 + e^{\frac{E_m}{kT}}\frac{1}{kT}\int_{E^*}^{E_m} D\left(\frac{E_x}{E_m}\right)e^{-\frac{E_x}{kT}}dE_x.$$

For abrupt heterojunction case

$$E^* = \begin{cases} qV_{j2} - \Delta E_c, & \text{when } qV_{j2} > \Delta E_c \\ 0 & \text{when } qV_{j2} \le \Delta E_c. \end{cases}$$

For graded heterojunction case the lower boundary of integration E^* is

$$E^* = \begin{cases} qV_{j2} - \Delta E_c, & \text{when } 0 < qV_{j2} - \Delta E_c < E_{m,graded} \\ 0 & \text{when } qV_{j2} - \Delta E_c \le 0. \end{cases}$$

Here the last condition is different from, e.g. Grinberg et al. [r19] in order to keep the region of integration inside the actual energy spike. The referenced condition is

$$E^* = \begin{cases} qV_{j2} - \Delta E_c, & \text{when } qV_{j2} - \Delta E_c < E_{m,graded} \\ 0 & \text{when } qV_{j2} - \Delta E_c \ge E_m. \end{cases}$$

The definition of E^* adjusts the lower boundary of integration such that when the notch of the conduction band edge in GaAs-side of the heterojunction at $x = 0^+$ is lower than the energy level of conduction band edge of the neutral AlGaAs, the integration starts from the neutral AlGaAs conduction band edge level. Otherwise the integration starts from the level of the notch at $x = 0^+$. E^* is always less than E_m in the calculation of γ_n. When the bias is such that $E^* > E_m$, the conduction band spike vanishes and conventional diffusion model applies.

The multiplication factor γ_n equals unity when the emission is purely of thermionic emission type. It was later verified by Das et al. [r20] by comparison of their more accurate quantum mechanical calculations to those of Grinberg et al. [r19], that the approximate equation (e81) gives current densities that are within 40% of the correct values. For an abrupt AlGaAs / GaAs heterojunction with AlAs-mole fraction x=0,3 the approximation underestimates the transparency of lower electron energies but overestimates the transparency of higher energy electrons. After integration, the error is partially canceled and the equation (e81) proves useful.

The electron concentrations $n(0^+)$ and $n(0^-)$ in equation (e81) are found from the pn-diode law,

(e82)
$$n(0^-) = n(-X2)e^{-\frac{qV_{j2}}{kT}}$$
$$n(0^+) = n(X1)e^{+\frac{qV_{j1}}{kT}}.$$

The potentials over the depletion regions are found from equation (e40) after substitution of the intentional doping concentrations N_A and N_D,

(e83)
$$V_{j1} = (V_{bi} - V_{be})\frac{N_D\varepsilon_{s2}}{N_A\varepsilon_{s1} + N_D\varepsilon_{s2}},$$
$$V_{j2} = (V_{bi} - V_{be})\left(1 - \frac{N_D\varepsilon_{s2}}{N_A\varepsilon_{s1} + N_D\varepsilon_{s2}}\right).$$

Heterojunction bipolar transistors are often designed such that N_A is much more than N_D. V_{j1} is then only a small fraction of V_{j2}. Minority electron concentration in the base side of the junction $n(0^+)$ does not easily approach majority hole concentration, and depletion region approximation is applicable.

If the electric field across the base is zero, the current conduction mechanism is diffusion in the neutral base layer. The diffusion current density $J_n(X1)$ at point x = X1 in Figure f12 is found from equation (e72),

(e84) $$J_n(X1) = +qD_n \left.\frac{d\Delta n(x)}{dx}\right|_{x=X1} = +\frac{qD_n}{L_n}\frac{\Delta n(X_3) - \Delta n(X1)\cosh\left(\frac{W_{base}}{L_n}\right)}{\sinh\left(\frac{W_{base}}{L_n}\right)},$$

where the material parameters refer to those of base layer. Forcing $J_n(X1)$ and $J_n(0)$ to be equal, the equation for excess electron concentration at x=X1 can now be solved,

(e85) $$\Delta n(X1) = n(X1) - n_0(X1) = \frac{1}{R_n}\left\{\eta_n \Delta n(X3) e^{-\frac{\Delta E_n}{kT}} + n(-X2) e^{\frac{-qV_{j2}-\Delta E_n}{kT}} - n_0(X1)\right\},$$

where

$$\Delta E_n = qV_{j1} - \Delta E_c$$
$$\eta_n = \frac{\sqrt{6\pi} D_n}{\gamma_n v_{th} L_n \sinh\left(\frac{W_{base}}{L_n}\right)}$$
$$R_n = 1 + \eta_n \cosh\left(\frac{W_{base}}{L_n}\right) e^{-\frac{\Delta E_n}{kT}},$$

and $n_0(X1)$ represents the electron concentration with zero bias at the depletion region edge $x=X1$. For clarity, $n_0(X1)$ needs not to be associated with the bulk minority carrier equilibrium concentration n_{01}. Equation (e85) should go zero without external bias, as should $\Delta n(X3)$. It follows that

(e86) $$n_0(-X2) = n_0(X1) e^{\frac{qV_{bi}-\Delta E_c}{kT}}.$$

This should be compared with the equilibrium electron concentrations far inside the neutral regions. Equilibrium electron concentration in neutral base far from the depletion region edge, n_{01}, may be represented by its dependence on equilibrium electron concentration in neutral emitter, n_{02}, and built-in potential V_{bi}. From equation (e9) it is found that if the semiconductor was not degenerate such that Boltzmann formula holds, under thermal equilibrium

(e87) $$\frac{n_{02}}{n_{01}} = \frac{N_{c2}}{N_{c1}} e^{\frac{E_{f2}-E_{c2}-E_{f1}+E_{c1}}{kT}} = \frac{N_{c2}}{N_{c1}} e^{\frac{E_{c1}-E_{c2}}{kT}} = \frac{N_{c2}}{N_{c1}} e^{\frac{qV_{bi}-\Delta E_c}{kT}}.$$

It is tempting to approximate the ratio of densities of states as 1,0 in the calculations above, to give

(e88) $$n_0(-X2) \approx n_{02} \approx n_{01} e^{\frac{qV_{bi}-\Delta E_c}{kT}}.$$

The density of states ratio in the $Al_{0,3}Ga_{0,7}As$ / $GaAs$ heterojunction is

$$\frac{N_{c2}}{N_{c1}} = \frac{7 \cdot 10^{17} cm^{-3}}{4,7 \cdot 10^{17} cm^{-3}} = 1,49.$$

The approximation is thus not always fair. Combining equations (e86) and (e87) gives

(e89) $$\frac{n_0(-X2)}{n_0(X1)} = e^{\frac{qV_{bi}-\Delta E_c}{kT}} = \frac{N_{c1} n_{02}}{N_{c2} n_{01}}.$$

Equation (e89) was derived under assumption of non-degenerate semiconductor. It is not uncommon to have degenerate doping especially in the base layer of a heterojunction bipolar transistor. Joyce-Dixon approximation of Fermi-Dirac integral is then used instead of Boltzmann equation in defining the Fermi level position against the band edge.

From equations (e7) and (e8) it is seen that the difference between the Boltzmann equation based Fermi level position $E_{f,B}$ and the Joyce-Dixon based position $E_{f,J}$ is

(e90) $$fN = \frac{E_{f,J} - E_{f,B}}{kT} = A \cdot \left(\frac{n}{N_c} \right) + B \cdot \left(\frac{n}{N_c} \right)^2 + C \cdot \left(\frac{n}{N_c} \right)^3 + D \cdot \left(\frac{n}{N_c} \right)^4,$$

for n-type semiconductor, and

$$fP = \frac{E_{f,B} - E_{f,J}}{kT} = A \cdot \left(\frac{p}{N_v} \right) + B \cdot \left(\frac{p}{N_v} \right)^2 + C \cdot \left(\frac{p}{N_v} \right)^3 + D \cdot \left(\frac{p}{N_v} \right)^4,$$

for p-type semiconductor. fN and fP are positive quantities. Equations (e9) and (e10) may be rewritten as

(e91)
$$n = \left\{ N_c e^{\frac{E_{f,B} - E_c}{kT}} \right\} e^{fN} = n_{Boltzmann} \cdot e^{fN},$$
$$p = \left\{ N_v e^{\frac{E_v - E_{f,B}}{kT}} \right\} e^{fP} = p_{Boltzmann} \cdot e^{fP}.$$

In mechanical calculations with degenerate semiconductors the Boltzmann concentration value should be reduced by the amount of exponential term in order to obtain the correct free carrier concentration. The correct value for n or p is found by iteration for specific $n_{Boltzmann}$ or $p_{Boltzmann}$. The built-in voltage of equation (e21) adjusts accordingly,

(e92) $$V_{bi} = \frac{E_{g1} + \Delta E_c - \Theta 1 - \Theta 2}{q} = V_{bi,Boltzmann} + \frac{kT}{q}(fN + fP).$$

The condition for vanishing current with zero bias then reduces back to equation (e89) even with degenerate doping, and the current equations remain useful.

Substituting (e89) into equation (e85), after taking into account that

$$-qV_{j2}-\Delta E_n=-q(V_{bi}-V_{be})+\Delta E_c,$$

gives the excess electron concentration at the base depletion region edge,

(e93)
$$\Delta n(X1)=\frac{J_{NE}}{R_n}\left\{\frac{\Delta n(X3)}{n_0(X1)}-\cosh\left(\frac{W_{base}}{L_n}\right)\left(e^{\frac{qVbe}{kT}}-1\right)\right\},$$
$$J_{NE}=\frac{qD_n n_0(X1)}{L_n\sinh\left(\frac{W_{base}}{L_n}\right)}.$$

Electron concentration at the collector side depletion layer edge *n(X3)* can be found from the pn-junction law of equation (e2),

(e94)
$$n(X3)=n_0(X3)e^{-\frac{qV_{cb}}{kT}},$$

where n_0(X3) is electron concentration at the collector depletion region edge at thermal equilibrium. V_{CB} is the magnitude of the collector-base bias in forward active mode. Substitution of equations (e93) and (e94) into equation (e84) gives

(e95)
$$J_n(X1)=+\frac{J_{NE}}{R_n}\left\{\left(e^{\frac{qVbe}{kT}}-1\right)\cosh\left(\frac{W_{base}}{L_n}\right)+\left(e^{-\frac{qV_{cb}}{kT}}-1\right)\right\}.$$

Similarly, the electron current density at the collector depletion region edge $J_n(X3)$ is

(e96)
$$J_n(X3)=+qD_n\left.\frac{d\Delta n(x)}{dx}\right|_{x=X3}=$$
$$+\frac{J_{NE}}{R_n}\left\{\left(e^{-\frac{qV_{cb}}{kT}}-1\right)\left[\cosh\left(\frac{W_{base}}{L_n}\right)+\eta_n\sinh^2\left(\frac{W_{base}}{L_n}\right)e^{-\frac{\Delta E_n}{kT}}\right]-\left(e^{\frac{qVbe}{kT}}-1\right)\right\}.$$

Hole current density across base-emitter junction $J_p(0)$ is determined in a same way as was done with electrons. Equation (e78) for holes reads

(e97)
$$J_p(0) = -\frac{qv_p}{\sqrt{6\pi}}\left\{p\left(X1^+\right)e^{\frac{-qV_j-\Delta E_v}{kT}} - p\left(-X2^-\right)\right\},$$

where v_p is thermal velocity of holes, $p(-X2^-)$ represents the holes flowing towards base from left and $p(X1^+)$ represents the holes flowing towards emitter from right. In thermal equilibrium the flow of holes that have enough energy to surmount the potential barrier of $qV_j + \Delta E_v$ from GaAs side is exactly compensated by the thermal flow of holes from AlGaAs, which do not suffer from any potential barrier.

Equation (e82) for holes reads

(e98)
$$\begin{aligned} p\left(0^-\right) &= p\left(-X2\right)e^{+\frac{qV_{j2}}{kT}} \\ p\left(0^+\right) &= p\left(X1\right)e^{-\frac{qV_{j1}}{kT}}. \end{aligned}$$

Assuming again that N_A is much more than N_D, V_{j1} will be only a small fraction of V_{j2}. There is appreciable probability that minority hole concentration in the emitter side of the junction $p(0^-)$ will approach majority electron concentration even in thermal equilibrium. This violates the depletion region approximation in the emitter side of the bipolar transistor [r21]. When solving the electric field inside the emitter depletion region using Poisson equation (e18), the mobile minority hole concentration should not be neglected. Taking the holes into account, the equation for built-in potential V_{bi} would be [r14]

(e99)
$$V_{bi} = \left(1 + \frac{\varepsilon_{s1}N_A}{\varepsilon_{s2}N_D}\right)\left(V_{bi} - V_{B2}\right) - \frac{kT}{qN_D}\left(\frac{n_{i2}^2}{N_D}\right)\left[e^{\frac{qV_{B2}}{kT}} - 1\right],$$

from which the emitter side potential V_{B2} is found by iteration, as V_{bi} is also found from equation (e21). With practical numerical values the additional term in equation (e99) is in the order of 1% of total built-in potential. In applications where such discrepancies in potentials are accepted the depletion region approximation may be considered valid.

The hole concentration in neutral emitter area is found from the diffusion equation

(e100) $$\frac{\Delta p(x)}{L_p^2}-\frac{d^2\Delta p(x)}{dx^2}=0,$$

where L_p is the hole diffusion length in emitter. With boundary conditions of

$$\Delta p(-X_e)=\Delta p(-X_e),$$
$$\Delta p(-X2)=\Delta p(-X2),$$

where $-X_e$ is the coordinate of the emitter contact, and keeping the origin at the junction as previously, the solution for $\Delta p(x)$ is

(e101) $$\Delta p(x)=-\left(\frac{\Delta p(-X_e)\sinh\left(\frac{x+X2}{L_{pe}}\right)-\Delta p(-X2)\sinh\left(\frac{x+X_e}{L_{pe}}\right)}{\sinh\left(\frac{W_e}{L_{pe}}\right)}\right),$$

where valid x values are between $-X_e$ and $-X_2$. The negative sign is visible to maintain the proper direction of hole diffusion current density in mechanical calculations. The hole diffusion current density $J_p(-X2)$ at point $x=-X2$ is then

(e102) $$J_p(-X2)=-qD_p\left.\frac{d\Delta p(x)}{dx}\right|_{x=-X2}=$$
$$=\frac{qD_p}{L_{pe}\sinh\left(\frac{W_e}{L_{pe}}\right)}\left\{\Delta p(-X_e)-\Delta p(-X2)\cosh\left(\frac{W_e}{L_{pe}}\right)\right\},$$

where $W_e=X_e-X2$ the neutral emitter thickness. The excess hole concentration is solved by forcing $J_p(-X2)$ and $J_p(0)$ to be equal. The equation for $\Delta p(-X2)$ is then

(e103) $$\Delta p(-X2)=\frac{\eta_p \Delta p(-X_e)+p(X1)e^{\frac{-qV_j-\Delta E_v}{kT}}-p_0(-X2)}{R_p},$$

where
$$R_p=1+\eta_p\cosh\left(\frac{W_e}{L_{pe}}\right),$$
$$\eta_p=\frac{\sqrt{6\pi}D_{pe}}{v_p L_{pe}\sinh\left(\frac{W_e}{L_{pe}}\right)}.$$

The constant R_p here is different from, e.g. [r19] because equation (e97) was constructed in a way that equation (e98) is avoided.

The necessary condition for vanishing excess hole concentration *Δp(-X2)* with zero bias is

(e104) $$\frac{p_0(X1)}{p_0(-X2)}=e^{\frac{qV_{bi}+\Delta E_v}{kT}}=\frac{p_{01}N_{v2}}{p_{02}N_{v1}}.$$

Substitution of equation (e104) and (e103) into (e102) with $\Delta p(-W_e)=0$ gives

(e105) $$J_p(-X2)=-\frac{J_{PE}}{R_p}\left(e^{\frac{qV_{be}}{kT}}-1\right)\cosh\left(\frac{W_e}{L_{pe}}\right),$$

where

$$J_{PE}=\frac{qD_{pe}p_0(-X2)}{L_{pe}\sinh\left(\frac{W_e}{L_{pe}}\right)}.$$

The collector junction of a basic heterojunction bipolar transistor is not a heterojunction. The hole diffusion current density at the collector depletion region edge $x=X4$ is similar to equation (e105),

(e106)
$$J_p(X4) = J_{PC}\left(e^{-\frac{qV_{cb}}{kT}} - 1\right)\cosh\left(\frac{W_c}{L_{pc}}\right),$$

where

$$J_{PC} = \frac{qD_{pc}p_0(X4)}{L_{pc}\sinh\left(\frac{W_c}{L_{pc}}\right)}.$$

The neutral collector width $W_c = X_c - X4$, and the material parameters refer to collector neutral region.

The total electrode currents of an ideal transistor can now be collected from above. Total emitter current density J_E is

(e107)
$$\begin{aligned}&J_E = J_n(X1) + J_p(-X2) = \\ &-\left\{\frac{J_{NE}}{R_n}\cosh\left(\frac{W_{base}}{L_n}\right) - \frac{J_{PE}}{R_p}\cosh\left(\frac{W_e}{L_p}\right)\right\}\left(e^{\frac{qV_{be}}{kT}} - 1\right) + \\ &+\left\{\frac{J_{NE}}{R_n}\right\}\left(e^{-\frac{qV_{cb}}{kT}} - 1\right)\end{aligned}$$

Total collector current density of an ideal transistor is

(e108)
$$\begin{aligned}&J_C = J_n(X3) + J_p(X4) = \\ &-\left\{\frac{J_{NE}}{R_n}\right\}\left(e^{\frac{qV_{be}}{kT}} - 1\right) + \\ &+\left\{\frac{J_{NE}}{R_n}\left[\cosh\left(\frac{W_{base}}{L_n}\right) + \eta_n \sinh^2\left(\frac{W_{base}}{L_n}\right)e^{-\frac{\Delta E_n}{kT}}\right] + J_{PC}\cosh\left(\frac{W_c}{L_{pc}}\right)\right\}\left(e^{-\frac{qV_{cb}}{kT}} - 1\right)\end{aligned}$$

The total base current density of an ideal transistor is $J_B = J_E - J_C$. Equations (e107) and (e108) relate the ideal heterojunction bipolar transistor current-voltage characteristics to the material parameters of the transistor in a convenient manner such that the basic device operation may be studied using common calculators. Different biasing conditions affect the neutral widths W_e and W_b according to equation (e41), and a similar equation for neutral collector width is easy to derive. Taking into account that material parameters may change with different AlAs mole fractions x, the equations also allow to study how the AlAs mole fraction affects transistor electrical behaviour. For this thesis the equations were encoded into a series of Matlab™ files to help in evaluation of the various effects of material parameters to the transistor action. Typical simulation run consists of about 1 million floating point operations and takes about 30 seconds in a 300MHz PII desktop computer. The parameters, control swithes and material constants that are used in calculations of the AlGaAs/GaAs-heterojunction bipolar transistor are collected into Tables I, II and III. The numerical values of simulation parameters in Table I should be considered as examples only. It is left for the user of the simulator to determine the exact numerical values.

Table I: User defineable parameters used in calculation of a AlGaAs/GaAs npn-heterojunction bipolar transistor with respective Matlab symbols in the HBT simulation platform header file.

USER DEFINED PARAMETERS:	MATLAB SYMBOL:	TYPICAL VALUE:	UNIT:
AlAs mole fraction	x	0,25	-
Base-Emitter Voltage	Vbe	scalar: 1,45	V
Collector-Emitter Voltage	Vce	vector: [0:0.01:5]	V
Base Voltage decrement	decr	0.01	V
Emitter doping	Ne	5e23	m^{-3}
Base doping	Nb	1e25	m^{-3}
Collector doping	Nc	2e23	m^{-3}
Emitter Area	Ae	4e-10	m^{-3}
Collector Area	Ac	4e-10	m^{-3}
Emitter junction distance from surface	Xje	1e-7	m
Collector junction distance from surface	Xjc	2e-7	m
Collector contact distance from surface	Xjb	8e-7	m
Device temperature	T	300	K
Trap density of emitter depletion region	Nt	2e22	m^{-3}
Trap density of collector depletion region	Ntc	2e22	m^{-3}
Trap capture cross section	sigman	4e-21	m^2
minority carrier lifetime in emitter	lifepe	1e-8	s
minority carrier lifetime in base	lifenb	2e-9	s
minority carrier lifetime in collector	lifepc	1e-8	s
Emitter surface recombination velocity	S0	1e4	m/s
First estimate for mobility in emitter	myye_ref	800e-4	$m^2/_{Vs}$
First estimate for mobility in base	myyb_ref	800e-4	$m^2/_{Vs}$
First estimate for mobility in collector	myyc_ref	800e-4	$m^2/_{Vs}$
minimum minority carrier density in emitter	poemin	0	m^{-3}
minimum minority carrier density in base	nobmin	0	m^{-3}
minimum minority carrier density in collector	pocmin	0	m^{-3}

Table II: Swithes used in controlling over the calculation of a AlGaAs/GaAs npn-heterojunction bipolar transistor with respective Matlab symbols in the HBT simulation platform header file.

	MATLAB SYMBOL:	TYPICAL VALUE:
Switches for controlling the simulation:		
1=enabled, other=disabled		
Enable the Kirk effect calculation	enable_Kirk	1
Disable band gap effects	default_Eg	0
Use Joyce-Dixon instead of Boltzmann	use_Joyce	1
Enable conduction band peak transparency	transparency	1
Enable correction for resistive losses	correct_for_res	0
Disable hole currents	holedis	0
Educational disturbance coefficients:		
multiply total transparency by amount of:	boost_transparency	1
multiply emitter diffusion coefficient by:	adjust_Dpe	1
multiply base diffusion coefficient by:	adjust_Dnb	1
multiply collector diffusion coefficient by:	adjust_Dpc	1
multiply device epitaxial layer thicknesses by:	Magnification	1
multiply electron thermal velocity by:	vn_coeff	1
multiply hole thermal velocity by:	Vp_coeff	1

Table III: Physical parameters used in the calculation of a AlGaAs/GaAs npn-heterojunction bipolar transistor with respective Matlab symbols in the HBT simulation platform header file.

Static parameter:	Matlab symbol:	Value of equation:	Unit:
Boltzmann constant	k	1,380658E-23	J/K
unit charge	q	1,6021773e-19	C
Planck's constant	hP	6,6260755E-34	Js
Emitter layer electron affinity	KhiiC2	4,07-1,1*x	eV
Base layer electron affinity	KhiiC1	4,07	eV
Collector layer electron affinity	KhiiC3	4,07	eV
Conduction band discontinuity	deltaEc	q*1,1*x	J
Emitter band gap in room temperature	EgC2	q*(1,424+1,247x)	J
Base band gap in room temperature	EgC1	q*1,424	J
Collector band gap in room temperature	EgC3	q*1,424	J
free electron mass	me	9,1093897E-31	kg
electron effective mass	mn	0,067*me	kg
hole effective mass	mh	0,5*me	kg
permittivity of vacuum	eps0	8,85419E-12	F/m
emitter permittivity at room temperature	epse	(13,18-3,12*x)*eps0	
base permittivity at room temperature	epsb	13,18*eps0	
collector permittivity at room temperature	epsc	13,18*eps0	
temperature adjusted emitter permittivity	epseT	epse*(1+1e-4*(T-300))	
temperature adjusted base permittivity	epsbT	epsb*(1+9*e-5*(T-300))	
temperature adjusted collector permittivity	epscT	epsc*(1+9e-5*(T-300))	
Emitter conduction band density of states	Nce	6,3E23	m^{-3}
Base conduction band density of states	Ncb	4,4E23	m^{-3}
Collector conduction band density of states	Ncc	4,4E23	m^{-3}
Emitter valence band density of states [r22]	Nve	Nce/0,04934	m^{-3}
Base valence band density of states [r22]	Nvb	Ncb/0,034	m^{-3}
Collector valence band density of states [r22]	Nvc	Ncc/0,034	m^{-3}
Temperature adjusted densities of states:			
see [r11]			
Carrier mobilities see [r11]			

Figure f14 shows the simulated collector characteristics of an ideal conventional GaAs bipolar transistor in common emitter configuration. Material parameters were those of Table I, and the calculation was based on Boltzmann approximation of Fermi-Dirac integral. Emitter thickness was 1000Å, base thickness was 1100Å and collector thickness was 6 000 Å. Emitter doping was $N_e = 2 \cdot 10^{23}$ m^{-3}, base doping was $N_b = 1 \cdot 10^{23}$ m^{-3}, and collector doping was $N_c = 4 \cdot 10^{22}$ m^{-3}. Base voltages during the collector voltage sweeps were V_{be} = 1,0 V, 0,98 V, 0,96 V, and 0,94 V. In Figure f15 the emitter is changed for $Al_{0,3}Ga_{0,7}As$ without altering the biasing conditions. The same V_{be} stepping induces somewhat less collector current because of the increase in built-in potential V_{bi}. Figures 15 and 16 compare the DC current gains of the transistors. The conventional GaAs transistor gain was about 2000. With heterojunction the gain increased to over $4,6 \cdot 10^7$.

Figure f18 shows how the gain of a conventional bipolar transistor would suffer from excessive base doping. Emitter doping was $N_e = 5 \cdot 10^{23}$ m^{-3}, base doping was $N_b = 1 \cdot 10^{25}$ m^{-3}, and collector doping was $N_c = 4 \cdot 10^{22}$ m^{-3}. Boltzmann approximation was again used in the calculation. The current gain barely exceeds unity. Figure f19 shows the same simulation with heterojunction emitter. The gain is about 1200 despite the high base doping. The collector current with V_{be} = 1,0 V or less keeps collector current in microampere level. Figure f20 shows the transistor collector characteristics with constant base voltage V_{be} = 1,35V, 1,33V, 1,31V and 1,29V as calculated from thermionic emission model, thus excluding electrons that would tunnel through the conduction band spike. Figure f21 gives the same characteristics as calculated from thermionic-field-diffusion model. The collector current level is increased over 100 times by the tunneling electrons. It is seen that collector current goes zero at about +300mV collector voltage. This is the offset voltage V_{offset} of the transistor. At offset voltage the collector electron current component $J_n(X3)$ of equation (e96) is exactly canceled by the collector hole current component $Jp(X4)$ of equation (e106). Low values of V_{ce} turn base-collector junction forward biased as the base bias voltage is kept constant, and hole current component increases exponentially according to equation (e106). Thermionic-field-diffusion model gives slightly lower V_{offset}. Solving V_{offset} from equations (e96) and (e106) with numerical values gives V_{offset} = 299 mV from thermionic emission model and V_{offset} = 218 mV from thermionic-field-diffusion model.

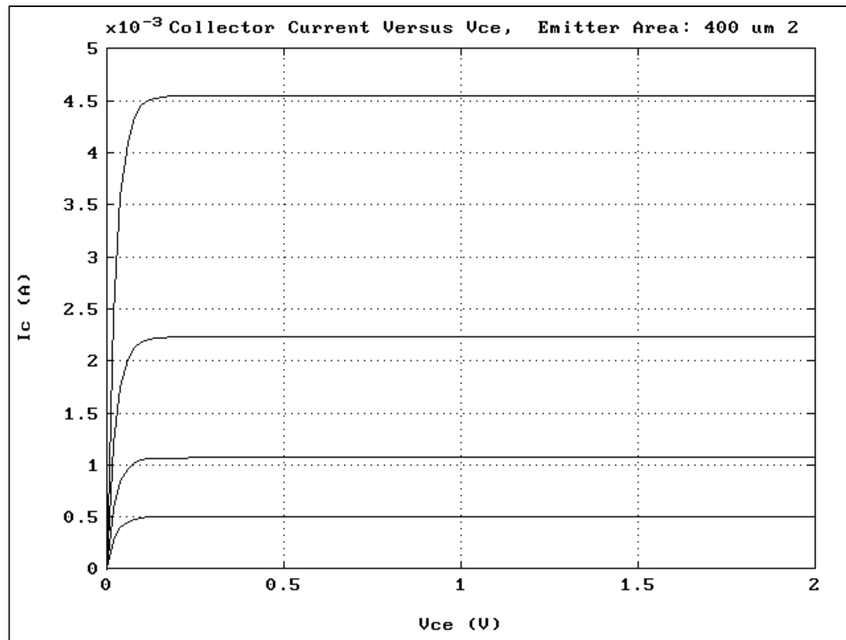

Figure f14: Simulated collector characteristics of an ideal GaAs homojunction transistor in common emitter configuration and constant base voltages of V_{be} = 1,0 V, 0,98 V, 0,96 V, and 0,94 V.

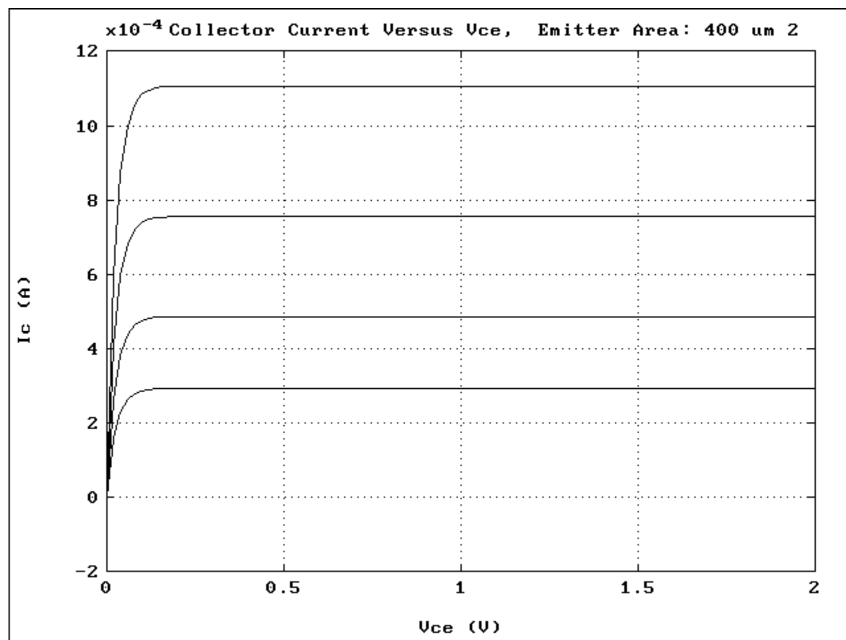

Figure f15: Simulated collector characteristics of an ideal $Al_{0,3}Ga_{0,7}As$/GaAs heterojunction transistor in common emitter configuration with the same biasing conditions as in Figure f14.

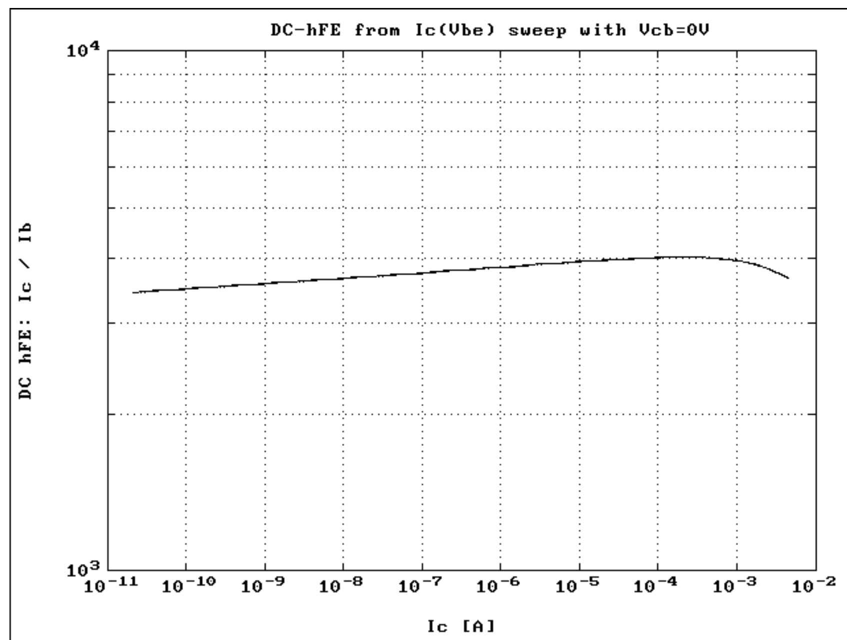

Figure f16: Current gain of the GaAs homojunction bipolar transistor of Figure f14.

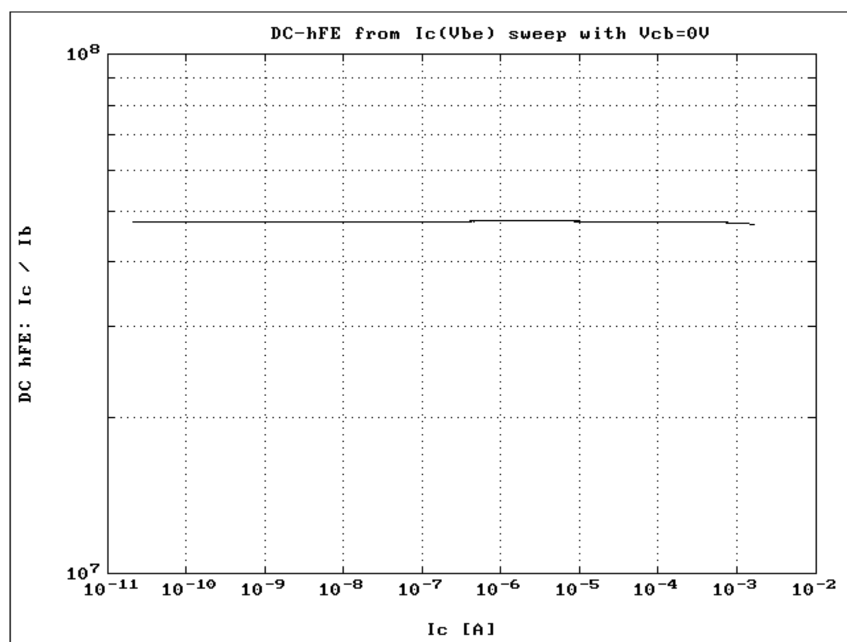

Figure f17: Current gain of the $Al_{0,3}Ga_{0,7}As$/GaAs heterojunction bipolar transistor of Figure f15.

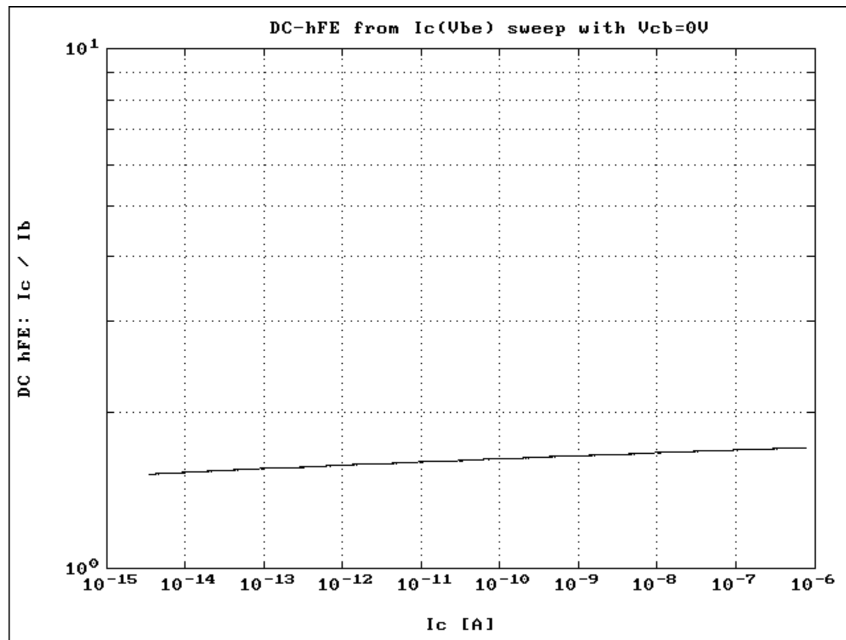

Figure f18: Conventional GaAs bipolar transistor with high base doping. Emitter doping was $N_e = 5 \cdot 10^{23}$ m^{-3}, base doping was $N_b = 1 \cdot 10^{25}$ m^{-3}, and collector doping was $N_c = 4 \cdot 10^{22}$ m^{-3}.

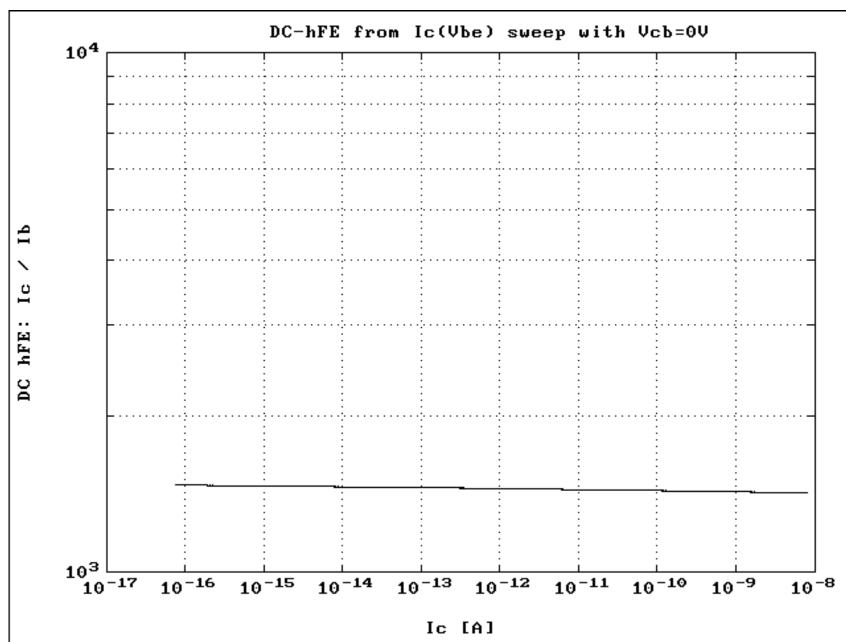

Figure f19: $Al_{0,3}Ga_{0,7}As$/GaAs heterojunction transistor with emitter doping of $N_e = 5 \cdot 10^{23}$ m^{-3}, base doping $N_b = 1 \cdot 10^{25}$ m^{-3}, and collector doping $N_c = 4 \cdot 10^{22}$ m^{-3}.

.

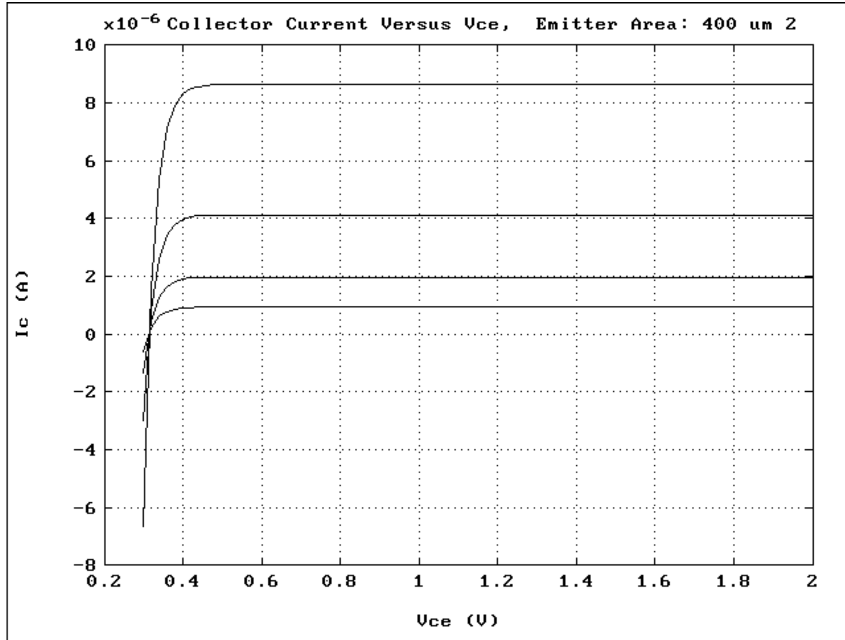

Figure f20: Collector characteristics with constant base voltage V_{be} = *1,35V, 1,33V, 1,31V*and *1,29V* for an $Al_{0,3}Ga_{0,7}As/GaAs$ heterojunction transistor with emitter doping of $N_e = 5 \cdot 10^{23}$ m^{-3}, base doping N_b = $1 \cdot 10^{25}$ m^{-3}, and collector doping $N_c = 4 \cdot 10^{22}$ m^{-3}. Calculation was based on thermionic emission model.

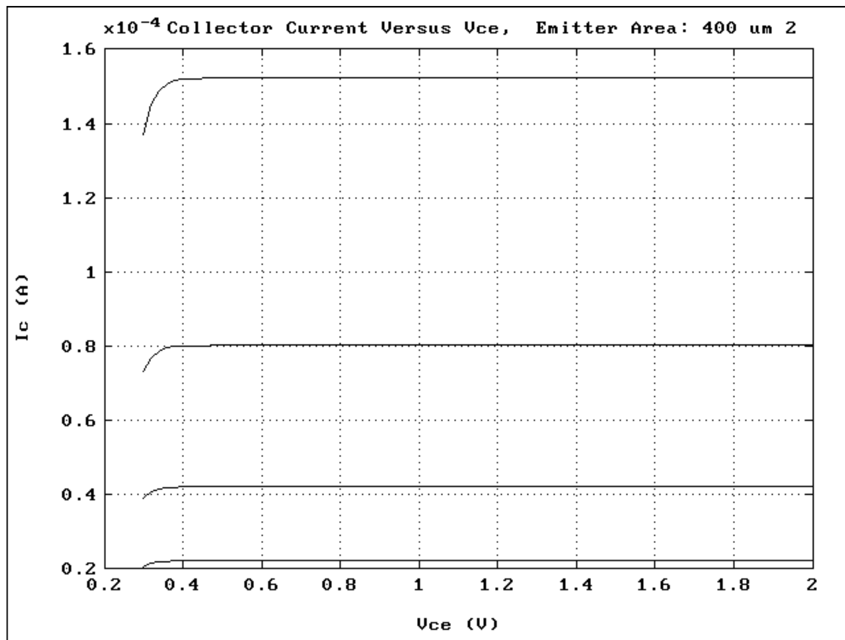

Figure f21: The same simulation as in Figure f20, but with the calculation based on thermionic-field-diffusion model.

2.11 Recombination and Generation currents in Depletion Regions

Thermal equilibrium inside a semiconductor volume element is restored by carrier recombination in the case of excess carriers, and carrier generation in the case of lack of carriers in order to maintain the thermal equilibrium condition of equation (e1). The recombination-generation event is either a band to band transition of electron or assisted by a trap level inside the forbidden band gap. Depending on how the released energy is dispatched after a band to band transition the event is classed to either radiative or Auger recombination [r13]. In the trap assisted case the event may include electron capture or emission by the trap with conduction band, and electron emission or capture by the trap with valence band. The trap state is neutral after electron emission to either conduction or valence band. The recombination rate U in [cm^{-3}/$_s$] of a single, uniformly distributed trap level assisted recombination-generation event is [r13]

(e109)
$$U=\left\{\frac{N_t}{\frac{1}{\sigma_p}\left[n+n_i e^{\frac{E_t-E_i}{kT}}\right]+\frac{1}{\sigma_n}\left[p+n_i e^{-\frac{E_t-E_i}{kT}}\right]}\right\}v_{th}\left(np-n_i^2\right),$$

where N_t is the trap density, σ_p and σ_n are the “capture cross sections” of holes and electrons in units of area, p and n are the hole and electron concentrations, n_i is the intrinsic carrier concentration, E_t is trap level in energy, E_i is the intrinsic Fermi level, and v_{th} is thermal velocity. For a trap level that coincidences with the intrinsic Fermi level,

(e110)
$$U=\left\{\frac{N_t}{\frac{1}{\sigma_p}\left[n+n_i\right]+\frac{1}{\sigma_n}\left[p+n_i\right]}\right\}v_{th}\left(np-n_i^2\right),$$

and if also the capture cross sections were equal for holes and electrons,

(e111)
$$U=\left\{\frac{\sigma_n N_t}{\left[n+p+2n_i\right]}\right\}v_{th}\left(np-n_i^2\right).$$

Under low injection conditions the excess minority carrier concentration is much less than the majority carrier concentration such that in p-type semiconductor

$$\Delta n = (n - \frac{n_i^2}{p}) << p,$$

and in n-type semiconductor

$$\Delta p = (p - \frac{n_i^2}{n}) << n.$$

Equation (e111) then reduces to

(e112) $$U = \left(\sigma_p N_t v_{th}\right)\left(p - \frac{n_i^2}{n}\right) = \frac{p - p_0}{\tau_p},$$

for n-type semiconductor, and

(e113) $$U = \left(\sigma_n N_t v_{th}\right)\left(n - \frac{n_i^2}{p}\right) = \frac{n - n_0}{\tau_n},$$

for p-type semiconductor. In the case of excess carriers equation (e111) gives a positive value of recombination rate. If there was lack of carriers, U would be negative in sign to indicate carrier generation. In thermal equilibrium U equals zero.

The recombination current density inside a volume element is found by integrating U over the volume and multiplying by the unit charge. In one dimension,

(e114) $$J_{recombination} = q\int_A^B U(x)dx,$$

where A and B are the boundaries of the region under study. Inside the depletion region of a pn-junction diode the thermal equilibrium value of the pn-product is amplified exponentially by the applied bias voltage V_j, and equation (e1) reads [r13]

(e115) $$np = n_i^2 e^{\frac{qV_j}{kT}}.$$

Equation (e111) is then

(e116) $$U(x)=\left\{\frac{\sigma_n N_t}{\left[n(x)+p(x)+2n_i\right]}\right\}v_{th}n_i^2\left(e^{\left(\frac{qV_j}{kT}\right)}-1\right)$$

Equation (e116) has a maximum value in the point $x = x_m$ where

$$n(x_m)=p(x_m)=n_i e^{\frac{qV_j}{2kT}}.$$

The maximum recombination rate U_{max} when the applied bias is such that

$$e^{\frac{qV_j}{kT}} >> 1$$

is then

(e117) $$U_{\max}=U(x_m)=\frac{\sigma_n N_t v_{th}}{2}n_i e^{\frac{qV_j}{2kT}}.$$

In section 2.3 the major recombination currents of a bipolar transistor biased in forward active mode were introduced. The base-emitter space charge region recombination current J_{re} for equations (e14) and (e15) is now

(e118) $$J_{re}=q\sigma N_t v_{th}\left(e^{\frac{qV_j}{kT}}-1\right)\int_{-X2}^{X1}\frac{n_i^2}{\left(n(x)+p(x)+2n_i\right)}dx,$$

where the integral is best solved piecewise. The upper limiting value of J_{re} is found by replacing $U(x)$ with U_{max} over the whole depletion region giving

(e119) $$J_{re}^{\max}=\frac{q\sigma_n N_t v_{th} n_i W_d}{2}e^{\frac{qV_j}{2kT}},$$

where W_d is the thickness of the depletion region.

More rigorous integration of equation (e118) over the n-side depletion region of the pn-junction with $p>n$ and $V_j >> (^{kT}/_q)$ gives [r23]

(e120) $$J_{re}^{n-side} = q\sqrt{\frac{\pi}{2}}\frac{\sigma_n N_t v_{th} n_{i2}}{\sqrt{\frac{qN_d(2V_{b2}-V_j)}{\varepsilon_{s2}}}}\left(\frac{kT}{q}\right)e^{\frac{qV_j}{2kT}},$$

where $V_{b2} = V_{bi} - V_{b1}$ is the built-in potential over the n-side of the junction, and is found from equation (e35). For the p-side depletion region of the pn-junction with $p>n$ and $V_j >> (^{kT}/_q)$ the integration would give [r14]

$$J_{re}^{p-side} \approx (e^1 - 1)\frac{q\sigma_n N_t v_{th}(n_{i1})^2}{N_a}W_p e^{\frac{qV_j}{kT}},$$

(e121)

where W_p is the p-side depletion region width, and is found from equation (e41). The total depletion region recombination current of a pn-junction is

(e122) $$J_{re} = J_{re}^{n-side} + J_{re}^{p-side}.$$

Equation (e122) can be applied in determining the recombination current inside the base-emitter junction depletion region of a heterojunction bipolar transistor. The total emitter current is according to equation (e14)

$$J_e = J_{ne} + J_{re} + J_{pe}.$$

The collector junction of a transistor under forward active mode is reverse biased. Equation (e115) indicates that the pn-product is less than the thermal equilibrium value, and carrier generation occurs in the base collector depletion region. Strong enough reverse bias forces both n and p much less than n_i, such that equation (e111) reduces to

(e123) $$U \approx -\frac{n_i \sigma_n N_t v_{th}}{2}.$$

Generation rate is constant over the reverse biased depletion region. Generation current density in the base-collector depletion region is found by integration,

$$J_{gC} = \frac{n_i q \sigma_n N_t v_{th}}{2} W_{dC},$$

(e124)

where $W_{dC} = X4\text{-}X3$ is the total depletion region width of the reverse biased base-collector junction,

$$W_{dC} = \sqrt{\frac{2\varepsilon_{s3}}{qN_{d3}}\left(V_{b3} - V_{a3}\right)} + \sqrt{\frac{2\varepsilon_{s1}}{qN_A}\left(V_{b1} - V_{a1}\right)},$$

where equation (e39) was used to divide the built-in potential V_{bi} and applied voltage V_a over the depletion region sides. Typical numerical values for single trap level recombination event modeling in gallium arsenide is given in Table I. Figures f22 and f23 show Gummel plots of an $Al_{0,3}Ga_{0,7}As$/GaAs heterojunction transistor with emitter doping of $N_e = 5 \cdot 10^{23}$ m^{-3}, base doping $N_b = 1 \cdot 10^{25}$ m^{-3}, and collector doping $N_c = 4 \cdot 10^{22}$ m^{-3} with and without the recombination effects. The current gain plot with recombination effects is shows in Figure f24.

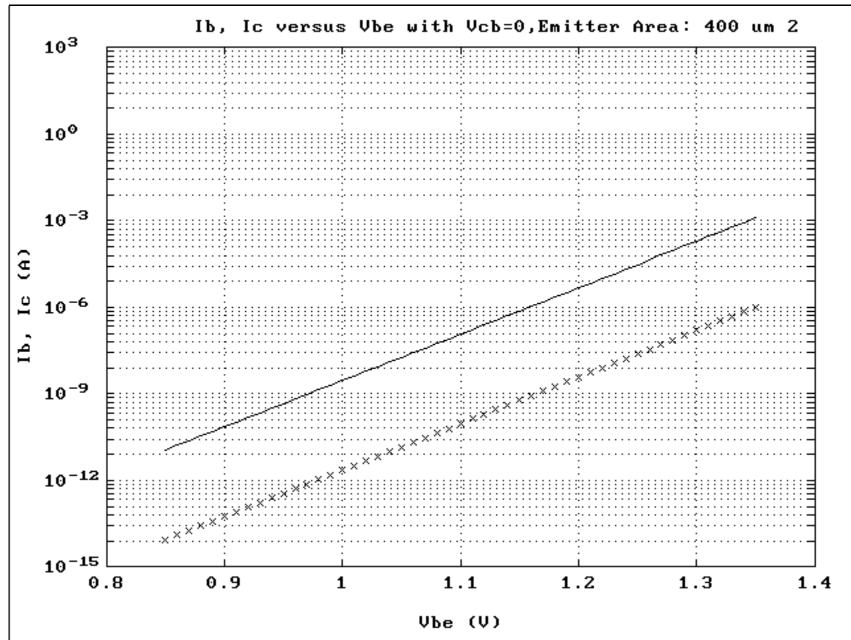

Figure f22: Gummel plot of an $Al_{0,3}Ga_{0,7}As$/GaAs heterojunction transistor with emitter doping of $N_e = 5 \cdot 10^{23}$ m^{-3}, base doping $N_b = 1 \cdot 10^{25}$ m^{-3}, and collector doping $N_c = 4 \cdot 10^{22}$ m^{-3}. Calculation was based thermionic-field-diffusion model without recombination effects. Line = *Ic*, x-line = *Ib*.

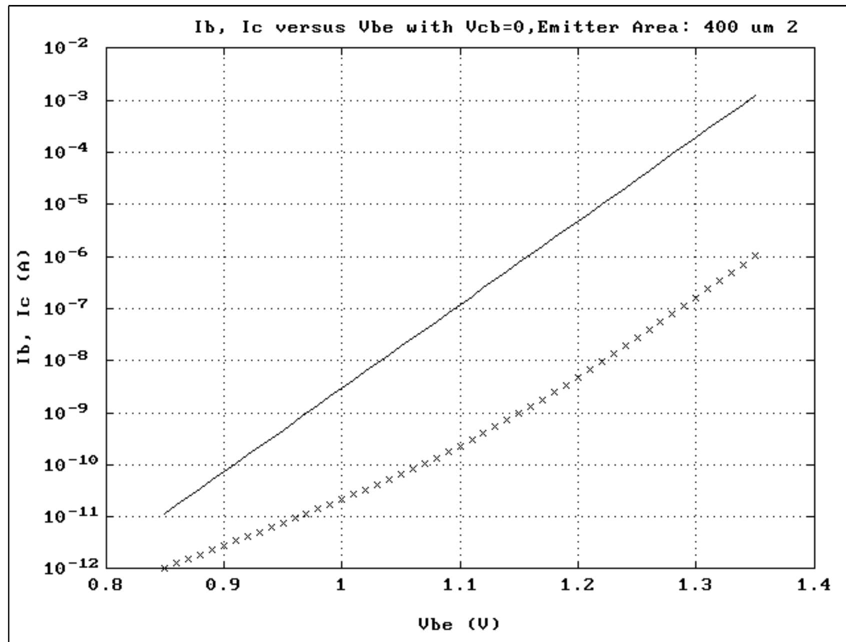

Figure f23: The same simulation as in Figure f22 with recombination effects. Line = *Ic*, x-line = *Ib*.

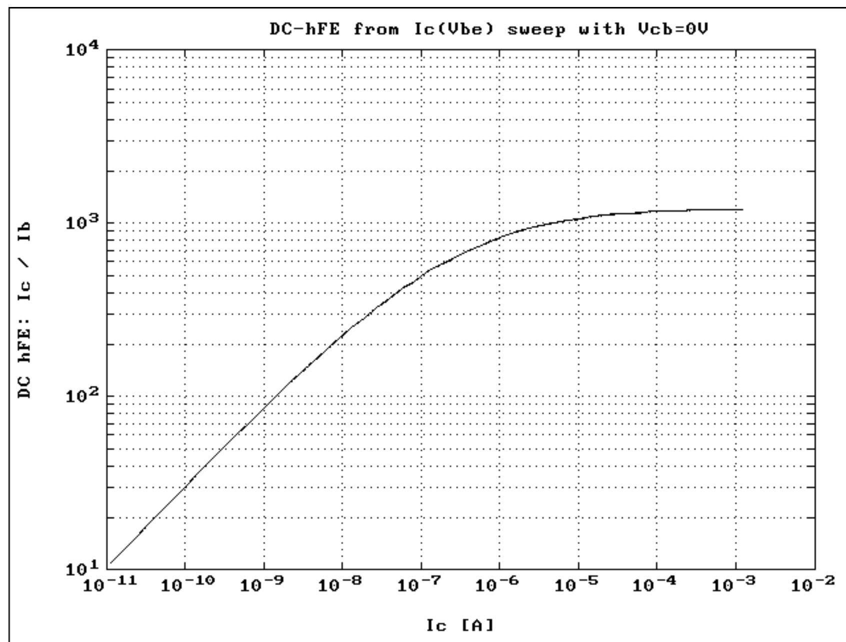

Figure f24: Current gain plot of the transistor of Figure f23.

It is seen that the base-emitter depletion region recombination lowers transistor current gain in low current levels. The transistor with recombination parameters of Table I would not perform well in collector current levels below 100 µA.

2.12 Band Gap Narrowing

Transistor terminal current equations (e107) and (e108) show that currents depend linearly on the product of diffusion coefficient and minority carrier equilibrium concentration, embedded inside coeffiecients J_{ne}, J_{pe} and J_{pc}. Combining equations (e1) and (e11) with $p = N_A$ in the heavily doped base, the equilibrium electron concentration in neutral base is

(e125)
$$n_{01} = \frac{n_{i1}^2}{N_A} = \frac{N_{c1} N_{v1} e^{-\frac{E_{g1}}{kT}}}{N_A}.$$

Minority carrier concentration is thus very sensitive on variations in forbidden band gap width E_g. In section 2.2 the gap was shown to vary with AlAs mole fraction x, wich induces appreciable variation in n_i. Another mechanism that alters n_i is heavy doping. Dopant atoms introduce statistical variation in the periodicity of the potential encountered by the charge carriers inside the semiconductor crystal, which together with carrier-carrier interaction transfers to rigid shrinkage of the band gap that may be a sizeable fraction of ΔE_C of equation (e13) [r24]. On the other hand, doping levels that exceed density of states N_v in the base fill the hole states completely in the top of valence band edge and force the Fermi level to enter deeper into the valence band. This degeneracy effect tends to widen the optical band gap of the base. Finally, the heavy doping disturbs the parabolicity of the density of states function ρ_c in energy scale such that calculation of carrier concentration p_0 or n_0 directly by integration over energy of the density of states function weighted by the occupation probability F of the state,

(e126)
$$n_0 = \int_{E_c}^{E_{max}} \rho_c (E - E_c) \cdot F(E - E_F) dE,$$
$$p_0 = \int_{E_{min}}^{E_V} \rho_V (E_V - E) \cdot [1 - F(E - E_F)] dE,$$

becomes involved. The $p_0 n_0$ product follows equation (e125) only if the density of states function is assumed parabolic and the semiconductor is not degenerate. If the energy gap is changed by ΔE_{g1}, the impact for n_i would be

(e127)
$$n_{i1,effective} = n_{i1} e^{-\frac{\Delta E_{g1}}{kT}}.$$

For silicon, the rigid energy band reduction due to majority-minority carrier pair interaction is given by [r13]

(e128) $$\Delta E_{g,silicon} = \frac{3q^2}{16\pi\varepsilon_s}\left(\frac{q^2 N_{doping}}{\varepsilon_s kT}\right)^{\frac{1}{2}},$$

where material parameters refer to silicon. The emitter of a conventional silicon bipolar transistor is heavily doped, and the band gap narrowing makes the device effectively a heterojunction transistor with emitter as the more narrow band gap material. According to equation (e74), this reduces the transistor current gain as n_{i2} increases by heavy doping. Equation (e128) does not hold for GaAs-based heterojunction bipolar transistors, but the effective intrinsic carrier concentration may still be represented in a similar fashion as in equation (e127), by introducing an “effective band gap shrinkage” ΔG, such that [r24]

(e129) $$n_{i1,effective} = n_{i1} e^{-\frac{\Delta G_1}{kT}}.$$

Under low doping, and assuming parabolicity of the density of states function ρ, the effective band gap shrinkage ΔG reduces back to the rigid band gap shrinkage ΔE_g. For modeling purposes the band gap narrowing effect in heavily doped p-type GaAs may be evaluated experimentally, as was done by *Klausmeier-Brown, Lundstrom and Melloch* [r24]. Extracting $(n_{i,effective})^2 \cdot D_{nb}$ product from measured collector current data and defining numerical values for D_{nb} using Einstein relationship

$$D_{nb} = \frac{kT}{q}\mu_{nb},$$

where μ_{nb} is the mobility of minority electrons in base, they found that effective band gap shrinkage for p-type GaAs may be fitted to function [r24]

(e130) $$\Delta G \approx 3.1 \cdot 10^{-8} (N_B)^{\frac{1}{3}} \qquad (\text{in } eV),$$

where N_b is in dimension of [cm^{-3}]. Electron mobility μ_{nb} was determined from an empirical formula [r24]

(e131) $$\mu_{nb} = \frac{\mu_{max} - \mu_{min}}{1 + \left(\frac{N_b}{N_{ref}}\right)^{\alpha}} + \mu_{min},$$

with numerical values of

$$\mu_{\max} = 8000 \frac{cm^2}{Vs},$$
$$\mu_{\min} = 943 \frac{cm^2}{Vs},$$
$$N_{ref} = 2{,}84 \cdot 10^{16} cm^{-3}.$$

It is seen that effective band gap shrinkage ΔG in p-type GaAs varies as $(Nb)^{1/3}$. As pointed out in [r24], equation (e130) is applicable up to doping levels N_b = $1 \cdot 10^{19}$ cm^{-3}, after which the equation may overestimate the effective band gap shrinkage. With N_b = $1 \cdot 10^{19}$ cm^{-3} equation (e130) gives ΔG = 66,8 meV, which may be compared to conduction band difference ΔE_c = 330 meV of $Al_{0,3}Ga_{0,7}As$ / GaAs junction. After adopting the effect of degeneracy to he fitting procedure the numerical values were fine tuned by *Harmon, Melloch and Lundstrom* [r25] to read

(e132) $$\Delta G = 2.55 \cdot 10^{-8} (N_A)^{\frac{1}{3}} + kT \cdot \ln\left(F_{\frac{1}{2}}\left[\frac{E_v - E_f}{kT} \right] \right) - (E_v - E_f),$$

for p-type GaAs, and

(e133) $$\Delta G = 3.23 \cdot 10^{-8} (N_D)^{\frac{1}{3}} + kT \cdot \ln\left(F_{\frac{1}{2}}\left[\frac{E_f - E_c}{kT} \right] \right) - (E_f - E_c),$$

for n-type GaAs. The Fermi-Dirac integral $F_{1/2}$ was introduced in equation (e3). For modeling purposes in this thesis the band gap shrinkage is calculated using definitions of equation (e90), or

(e134) $$\Delta G = 2.55 \cdot 10^{-8} (N_b)^{\frac{1}{3}} - kT \cdot fP,$$

for the base layer of the transistor, and

(e135) $$\Delta G = 3.23 \cdot 10^{-8} (N_e)^{\frac{1}{3}} - kT \cdot fN,$$

for the emitter layer of the transistor. Figures 21a and 21b compare transistor current gain dependence on band gap narrowing effect. Doping concentrations in the simulation were chosen such that, after taking into account the degeneracy effects, emitter majority electron concentration was n_{0e} = $5 \cdot 10^{23}$ m^{-3} , base majority hole concentration p_{0b} = $1 \cdot 10^{25}$ m^{-3} and majority electron concentration in collector n_{0c} = $4 \cdot 10^{22}$ m^{-3}.

Figure f25 gives transistor gain without band gap narrowing effects, and Figure f26 shows the gain with the band gap narrowing effects included. It is seen that transistor gain is underestimated severely if the band gap narrowing effect is not taken into account in simulations.

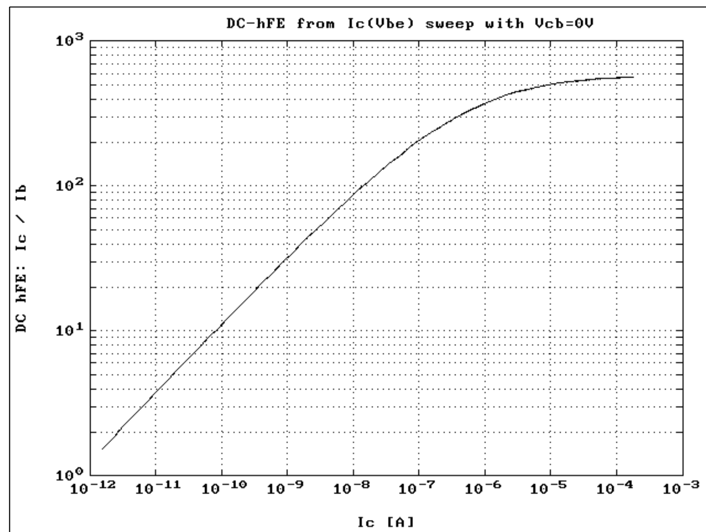

Figure f25: Transistor gain as calculated without band gap narrowing effects.

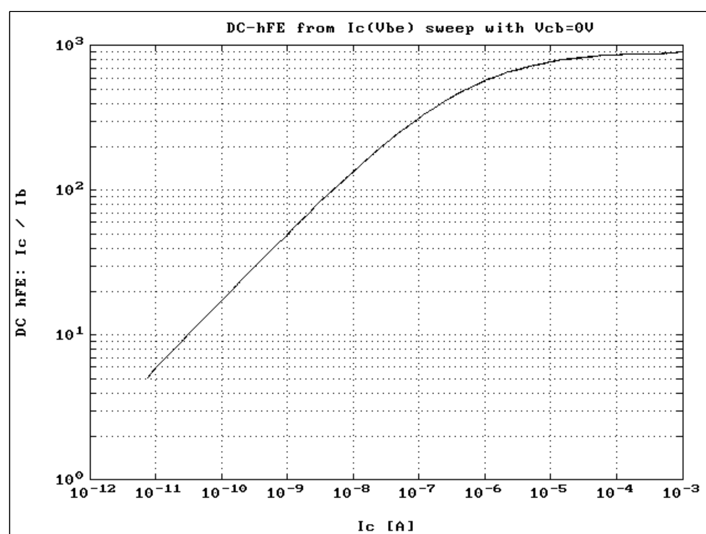

Figure f26: Transistor gain as calculated with band gap narrowing effects included.

2.13 Bias Conditions for Simulations

In order to gain full benefit from the basic transistor current equations some limiting conditions must be recognized. The excessive collector current density under strong bias conditions induces base push out or the "Kirk effect". Beyond a certain current level the mobile charge inside collector depletion region becomes comparable to the doping concentration N_c, and calculation of electric field with Poisson equation (e18) needs to be done mobile charge inclusive. Inside the collector depletion region the electrons travel at saturation velocity v_s of the order of 10^7 $^{cm}/_{s}$. The mobile charge inside the depletion region that is needed to maintain current flow is found from equation (e66). As collector current density increases, the mobile charge reduces the total space charge and forces the collector depletion region to become wider. If the base-collector bias V_{CB} is kept constant, the integral over electric field over the depletion region remains constant forcing the peak electric field to become lower.

At a definite current level the depletion region edge reaches the back side of the collector layer preventing further widening with increasing collector current. Instead, the shape of the electric field curve becomes pentagonal while the peak value at base-collector junction continues to decrease maintaining the constant area. At the onset of the Kirk effect the electric field at the junction goes zero. The majority holes at base layer are then allowed to spill into collector side, and the neutral base layer gets wider. As a consequence, the transistor current gain is reduced as indicated by equation (e74), and the base transit time is increased as indicated by equation (e70).

The Kirk effect is included into the simulation code used in this thesis in order to gain an estimate on the severity of the Kirk effect under the biasing conditions under study. However, the implementation is incomplete, modeling the effect only by rigid shifts of the base collector junction and the depletion region edges. After the onset of Kirk effect, the code will not produce strictly physically correct terminal currents. An example of transistor terminal characteristics with Kirk effects is shown in Figure f27. Doping concentrations were $N_e = 1 \cdot 10^{24}$ m^{-3}, $N_b = 5 \cdot 10^{23}$ m^{-3} and $N_c = 4 \cdot 10^{22}$ m^{-3}.

Base punch through is another possible bias-induced effect that affects the simulations. Heterojunction bipolar transistor design contains usually rather narrow layers of semiconductor, and it is relatively easy to choose doping and bias conditions such that the depletion regions occupy the whole base layer. Figure f28 shows how base width narrowing affects the transistor collector characteristics. Emitter thickness was 1000Å, base thickness was 1100Å, and collector thickness was 6000Å. Doping concentrations were $N_e = 5 \cdot 10^{23}$ m^{-3} , $N_b = 3 \cdot 10^{23}$ m^{-3} and $N_c = 4 \cdot 10^{22}$ m^{-3}. Base voltage bias was *1,1 V*, *1,08 V*, *1,06 V* and *1,04 V* during the collector sweeps. Figure f29 shows the neutral base layer width of the transistor during the simulation. The base is almost punched through by the collector depletion region under high reverse base-collector voltage. In IV-curves the punch-through effect is seen by strong increase in collector current level.

The final limitation of the usage of the current equations come from the fact that base current is not a freely variable parameter in simulations. Collector characteristics of a transistor are measured with fixed base current, letting V_{be} drift during measurement. In order to directly plot current to voltage simulations with constant base current, the respective base voltage need to be determined by iteration in every point of observation. The simulation platform for this thesis includes the iterative procedures, but the code proved slow in giving reasonable accuracy. That is why the constant base current analysis was excluded from this thesis.

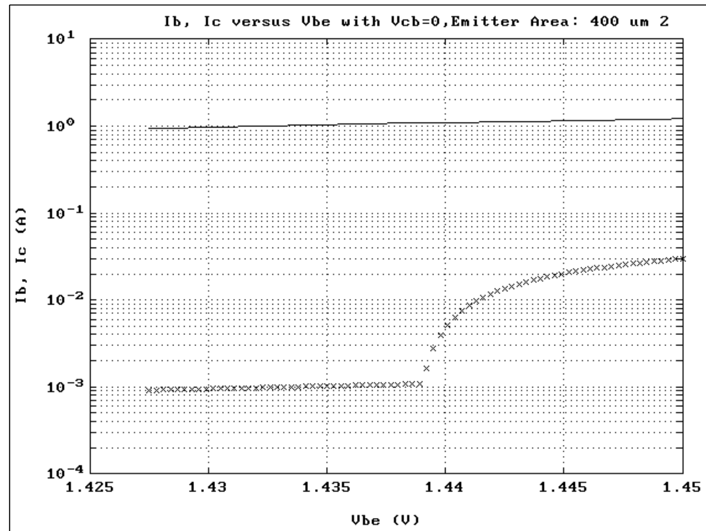

Figure f27: A transistor with Kirk effects included in the simulation. It is seen that current gain is reduced considerably after the collector current reaches the onset of Kirk effect.

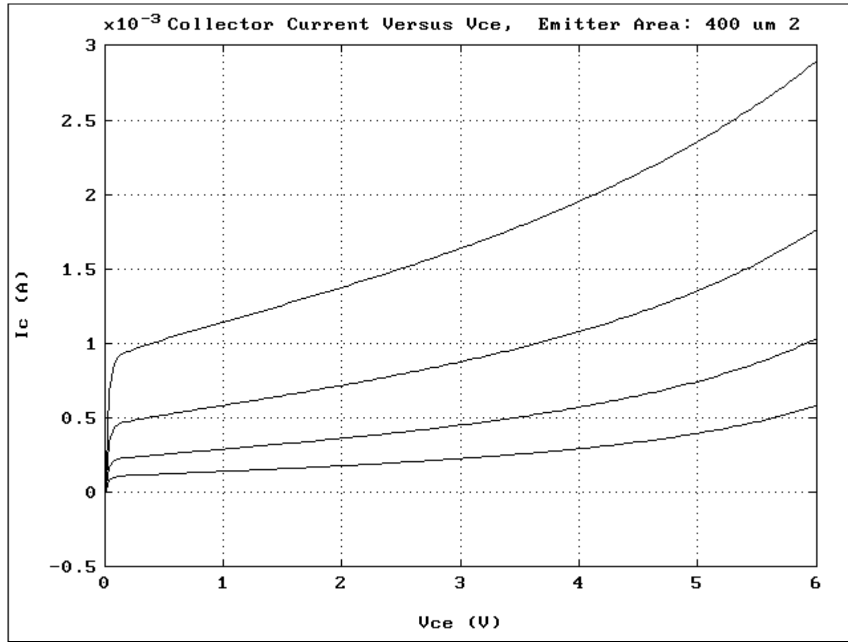

Figure f28: Transistor collector characteristics affected by base width narrowing effect. Emitter thickness was 1000Å, base thickness was 1100Å, and collector thickness was 6000Å. Doping concentrations were $N_e = 5 \cdot 10^{23}$ m^{-3} , $N_b = 3 \cdot 10^{23}$ m^{-3} and $N_c = 4 \cdot 10^{22}$ m^{-3}. Base voltage bias was *1,1 V*, *1,08 V*, *1,06 V* and *1,04 V* during the collector sweeps. AlAs mole fraction was x= 0,3.

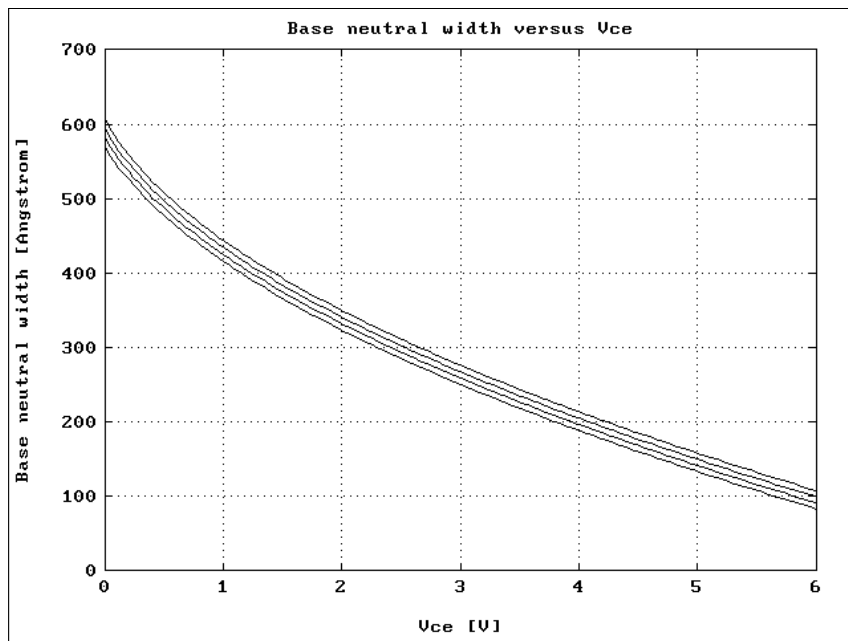

Figure f29: The neutral base layer width of the transistor during the simulation of Figure f28.

3 Experimental

In the experimental section of this thesis the focus is on the processing of traditional AlGaAs/GaAs heterojunction bipolar devices. The description of processing steps and the adopted methods follow those that are in use at Electron Physics Laboratory of Helsinki University of Technology. The process relies on proper device orientation with the substrate crystal, and utilises wet chemical etching on the mesa isolation steps. All the processing steps are manually controlled with common laboratory equipment. As such, the process is not intended to be used on large scale integration, nor it is directly applicable to high volume production. The described process is more suitable on laboratory scale experiments and hands-on education of basic device processing. Laboratory scale processing of compound semiconductor devices contains many distinctive details that one needs to be familiar with. One of the most important facts is the ease how a gallium arsenide wafer can be split to pieces after any scratch on the wafer periphery. While describing the processing steps, the proper methods as adopted in Electron Physics Laboratory are explained where ever possible. Optical lithography practise for this thesis is based on the special processes developed in the laboratory during several years of research. One of the most distinctive details of the adopted lithography is the usage of AZ5214E resist in multilayer sheme, in a way that allows the multi layer resist to be patterned in a layer by layer basis [r26]. Some of the basic research that led to first measurable heterojunction bipolar transistors made in Electron Physics Laboratory is explained in [r27].

3.1 Epitaxial Structure

Figure f30 shows a typical structure for a single heterojunction bipolar transistor. The basic device is a npn-transistor with “emitter up” design having abrupt junctions between the epitaxially grown layers. The cross section of a transistor with epitaxial layers as in Figure f30 was shown in Figure f1. In practise, several modifications to the basic structure are made to boost up the transistor speed and to make ohmic contacts more perfect. Figure f31 shows the heterojunction bipolar transistor with the most common modifications. The collector layer is divided to moderately doped and highly doped parts to reduce the base-collector capacitance. Emitter layer is graded to smoothen out the potential spike on the base-emitter boundary that would otherwise hinder electron injection from emitter. The emitter is capped with a heavily doped GaAs layer. This layer shields the oxygen sensitive emitter while serving as a contact

layer. It would be rather difficult to form a low resistivity contact directly to AlGaAs. More tailored structures include compositional grading also through the base layer. The purpose is to generate an electric field inside the otherwise neutral base that accelerates electrons towards base-collector boundary. Thus the electron transit time through base is reduced and the device speeds up.

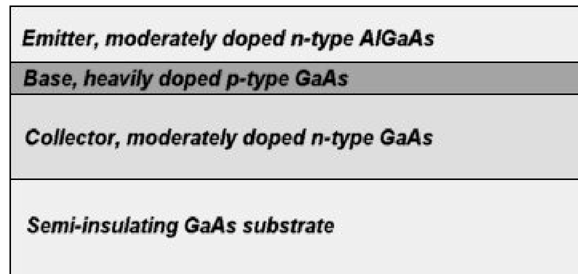

Figure f30: The basic epitaxial structure for a single heterojunction bipolar transistor.

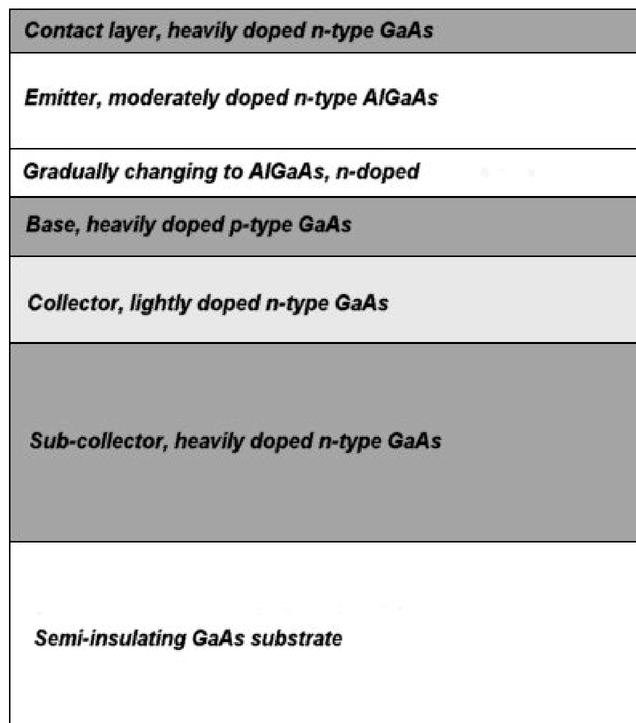

Figure f31: The heterojunction bipolar transistor structure with the most common modifications.

The epitaxial HBT structure is usually grown either using molecular beam epitaxy (MBE) or metallo-organic vapour phase epitaxy (MOVPE). Traditional MOVPE uses silicon as donor type dopant in GaAs, and zinc as acceptor type dopant in GaAs. MBE uses typically beryllium for acceptor type doping in GaAs. Both zinc and beryllium diffuse relatively rapidly in GaAs, and Zn redistribution during epitaxial growth with MOVPE has been a concern especially when highly silicon doped layers are involved [r28]. When acceptor atoms diffuse from base to emitter side, the pn-junction is shifted away from the heterojunction and the electrical structure is destroyed. Also, it has been difficult to achieve electrically active acceptor concentrations over $5 \cdot 10^{18}$ cm^{-3} with MBE. During the last decade MBE technology has adopted carbon as the acceptor type dopant in GaAs to suppress the diffusion problem. With carbon it is also possible to dope the base up to 10^{20} cm^{-3} level. When beryllium or zinc is used as p-type dopant, a spacer layer is usually added before heterojunction to prevent pn-junction shift. The spacer layer width is determined empirically and is usually about 10 .. 20 nm.

3.2 Current Gain Simulation of the Example Structure

The optimisation of a spesific HBT structure for layer thickness and doping concentrations is usually done with commercial computer sofware [r11]. If the transistor process is not well parameterized like often is the case in laboratory experiments, basic one dimensional calculations serve the purpose. One can then utilize simulation programs like PC-1D [r22], or rely on semiconductor text books, e.g., [r29]. All the simulation examples in this thesis are done with the matlab code generated by the author. Figure f32 shows an example of a real HBT structure. The vertical dimensions of the layers are in scale to illustrate their relative thicknesses. The dimensions are those that were used for the epitaxy of wafer “HBT02” processed during the experimental part of this thesis. Other properties of the layers are explained in Section 3.3.

The device in Figure f32 is a representation of an HBT in one dimension without external electrical connections to the actual device terminals. Simulation is needed in determining the proper doping concentrations for the layers before one could grow the epitaxial structure. For initial simulations, the structure of Figure f32 was reduced to three layers by removing the contact layers above emitter. The heterojunction grading was also removed, and the protective layer was joined with base. The active area of the device was put to 400 μm^2. The emitter AlAs mole fraction x was put to 0,25. Bulk recombination lifetimes were τ_{pe} = 0,076 μs for emitter, τ_{nb} = 0,0001 μs for base, and τ_{pc} = 0,34 μs for collector. Layer thicknesses for emitter, base and

collector were 1000 Å, 1100 Å and 6000 Å, respectively. Emitter doping was $N_e = 5 \cdot 10^{17}$ cm^{-3} and collector doping was $N_c = 4 \cdot 10^{16}$ cm^{-3} . With base doping of $N_b = 3 \cdot 10^{19}$ cm^{-3} the base-collector depletion region edge was about 218 nm into collector. The energy band diagram of the reduced structure with base doping of $N_b = 3 \cdot 10^{19}$ cm^{-3} was shown in Figure f6 with discussion on band gap tailoring.

Figure f33 shows the simulated current gain of the transistor with base doping of $3 \cdot 10^{17}$ cm^{-3}. Base-collector voltage was kept zero during simulation. Recombination effects were not included. With this doping level the base is not yet degenerate. The current gain is over 500 although the base narrowing effect reduces gain as V_{be} increases. Figure f34 shows the simulated effect for increasing the base majority carrier concentration by two orders of magnitude to $3 \cdot 10^{19}$ cm^{-3}. The simulated current gain is reduced to 50, which is still an acceptable value for device application in amplifier circuits.

The actual epitaxial structure contains a grading layer between emitter and base that smoothens the energy spike. The presence of a spike in conduction band increases the turn-on voltage of the base-emitter diode. V_{be} for 1kA/cm^2 forward current density was about 1,35 V for the structure of Figure f34. Proper smoothening of the spike should reduce the turn-on voltage for about 150 mV [r16]. The effect of spike smoothening may be simulated by, e.g., giving a very high value for the spike transparency γ in equation (e81) during simulations. Magnifying the transparency for about 500 times or more during calculations yielded to turn on voltage of about 1,245 V for the structure of Figure f34, with a slightly increased current gain.

Series resistance losses and two dimensional potential variations are not included in the core equations. However, the importance of series resistance losses is acknowledged, and a simple resistivity model is included into simulation code that calculates first estimates on resistive losses across transistor layers for the user. These refinements are not included in the text of this thesis.

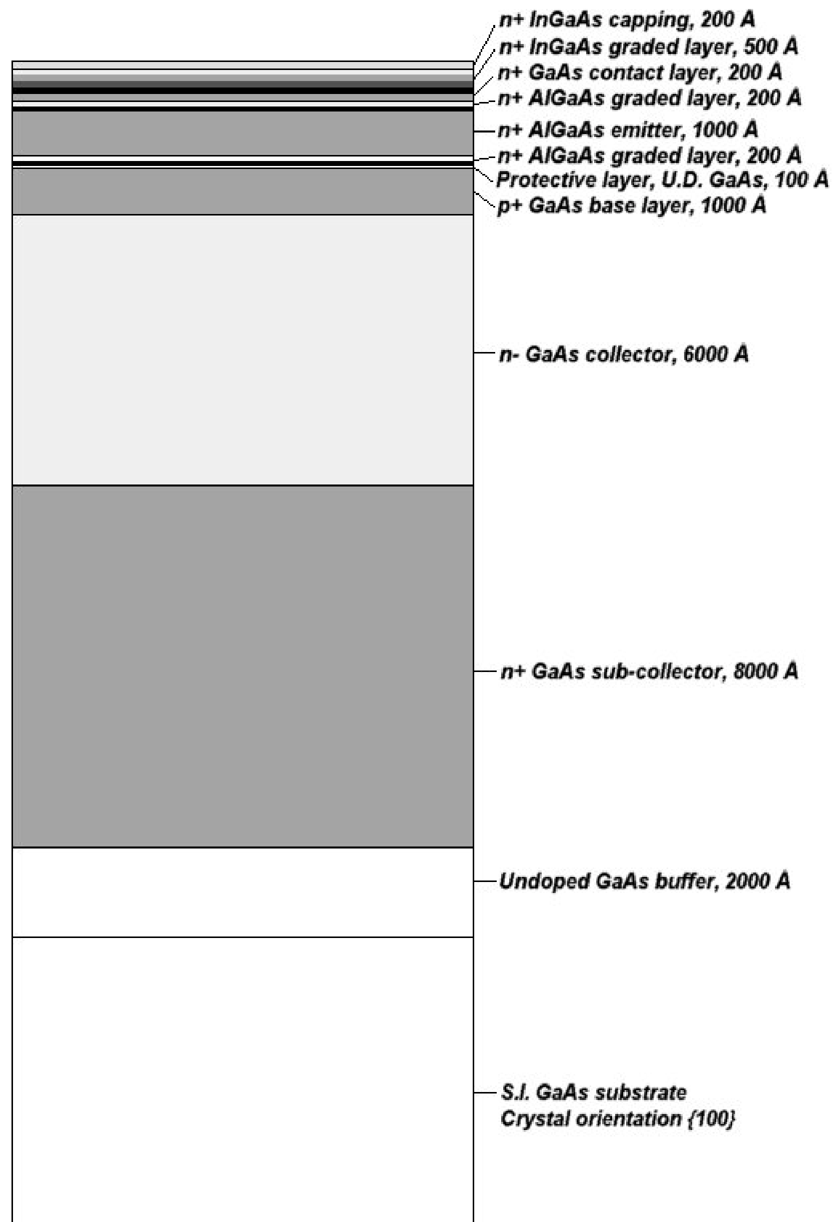

Figure f32: An example of a real HBT structure.

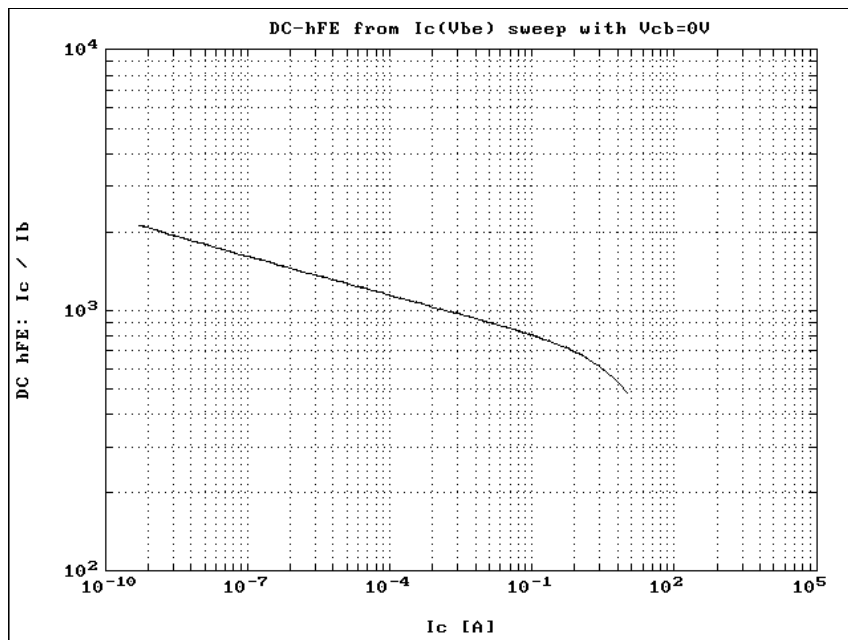

Figure f33: Simulated current gain of the abrupt heterojunction structure with base doping of $N_b = 3 \cdot 10^{17}$ cm^{-3}.

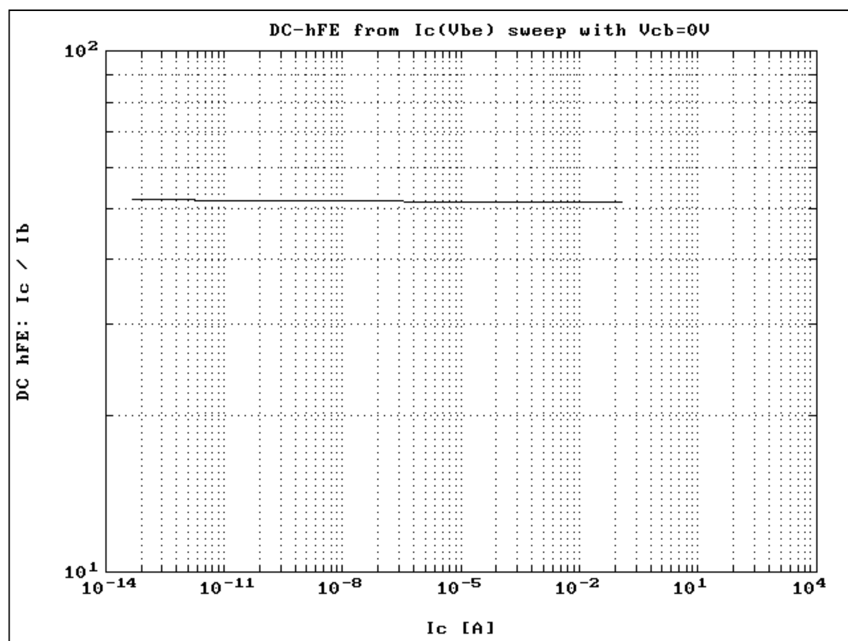

Figure f34: Simulated current gain of the abrupt heterojunction structure with base majority carrier concentration increased by two orders of magnitude to $3 \cdot 10^{19}$ cm^{-3}. The gain is still over 50.

3.3 Epitaxial Layers in Detail

The early experimental work for this thesis was done with samples that were epitaxially grown by H.U.T. Optoelectronics Laboratory. Samples that contained beryllium as base layer doping were grown by A. F. Ioffe Physico-Technical Institute in St. Petersburg. Various epitaxial constitutions were tried out during the process development while practical processing knowledge was being gained. The epitaxial structure of wafer "HBT02", represented in Figure f32, is chosen here as an example. Although the layers are explained in detail, the overall structure was not optimised to any spesific purpose but demonstration of the basic process. The base layer was deliberately doped to very high level to avoid complications that may have occurred due to excessive series resistance of the base contact. It was clear from previous studies that ohmic contact optimisation may be tedious and time consuming [r09]. As a result of high base doping, the current gain of the transistors was not expected to be higher than shown in Figure f34. The emitter layer contained InGaAs capping to facilitate low emitter contact resistance without extensive process optimisation. It was also recognized during the early stages of process development that it would be rather difficult to achieve good ohmic contacts for both emitter and collector simultaneously if the contact metal was kept the same for both terminals, as was assumed during mask design [r27]. However, perfect ohmic contact in collector was not essential for this thesis, and the collector contact was realised by a Schottky barrier which is forward biased during forward active operation of the transistor. The layers that consitute the processed HBT wafer are explained in detail below.

n+ (Si-doped) InGaAs contact layer, 5E18 cm-3, x=50%, 200 Angstroms

This layer is heavily doped and contains indium. Some ohmic contact processes introduce indium to the contact during ohmic metallisation and the following heat treatment. InGaAs capping introduces indium to the contact without alloying [r53]. Low resistivity contact between the emitter and contact metal will be presumably due first to high silicon doping enhancing the electron tunneling through the interfacial potential barrier and second because of indium lowering the barrier by pinning the Fermi-level on the interface. In GaAs the pinning position is roughly 0,8 eV below conduction band edge, and in pure InAs it is about 0,1 eV inside the conduction band. With 50% of indium one has the pinning position in somewhere between [r30].

n+ (Si-doped) InGaAs grading layer, 5E18 cm-3, graded roughly linearly, x=0.05 on bottom, x= 50% on top, 500 Angstroms

This layer smoothens out the potential spike of $In_{0,5}Ga_{0,5}As$ / GaAs interface and helps ruling out the strain induced by the lattice mismatch. Without this layer the lattice mismatch would be too much for epitaxial growth. Even with the grading layer present, $In_{0,5}Ga_{0,5}As$ will be more or less multicrystalline in nature [r52].

n+ (Si-doped), 5E18 cm-3, GaAs contact layer, 200 Angstroms

This layer also helps ruling out the spike. In simpler structures this layer is the contact layer for metal, but then it would be much thicker to prevent ohmic metallisation penetration into heterojunction area especially if gold-germanium based ohmic metallisation is used. For shallow contacts, a Pd-In metallisation scheme could be used where InGaAs is formed to the semiconductor surface during anneal [r31].

n+-AlGaAs grading layer, 2E18 cm-3, graded roughly linearly, x=25% on bottom, x= 0.05 on top, 200 Angstroms

This layer smoothens out the potential spike in the interface between capping layer and emitter.

n-AlGaAs emitter, x=25%, 5E17 cm-3, 1000 Angstroms

This layer is the actual emitter.

n-AlGaAs grading layer, 5E17 cm-3, graded roughly linearly, x=0.05 on bottom, x= 25% on top, 200 Angstroms

This layer helps smoothing out the potential spike between emitter and base. Without the smoothing layer, the transistor emitter-base junction would need more forward bias to inject electrons from emitter to base.

protective layer of undoped GaAs, 100 Angstroms

This layer prevents beryllium diffusion from base to heterojunction during epitaxial growth of the upper layers. If the structure is heated excessively during the transistor processing or use, this layer helps to minimise the performance reduction.

p+(Be-doped) GaAs base, 3E19 cm-3, 1000 Angstroms

This layer is the actual base. It is relatively thin to reduce electron transit time from emitter to collector and heavily doped to keep the series resistance low. The doping level is enough to turn the base degenerate. Although simple simulations in section 3.2. suggested that the doping should be reduced for better current gain, it was kept high to make sure a tunneling contact would be formed with base ohmic metal without need for high temperature alloying. With thickness of 1000Å, the base transit time for an electron with saturation velocity of $2 \cdot 10^5$ m/s would be about 0,5 ps. The diffusion transit time with a typical diffusivity of D_b = 30 cm^2/s would be about 1,7 ps.

n- (Si-doped) GaAs collector, 4E16 cm-3, 6000 Angstroms

This layer is the collector. It is lightly doped to allow the pn-junction depletion region to be wide thus reducing the base-collector capacitance. The maximum frequency of oscillation f_{max} (or the power gain cut off frequency) of the transistor depends on the product of base series resistance and base-collector capacitance. Reducing both will increase the transistor high frequency performance. According to section 3.2., the depletion region depth in thermal equilibrium will be about 218 nm. With a 400 μm^2 device active are this gives base-collector depletion capacitance of C_{bc} = 0,2 pF. Assuming a series resistance of 1 Ω, the charging time constant of the capacitance would be 0,2 ps. To keep the charging time less than the diffusion transit time of base, the collector series resistance should not exceed 10 Ω. Under normal operation conditions of the transistor, b-c junction would be reverse biased and electrons are accelerated to saturation velocity in the depletion region. An electron with saturation velocity of $2 \cdot 10^5$ m/s would have the depletion region transit time of about 0,6 ps.

n+(Si-doped) GaAs sub-collector, 5E18 cm-3, 8000 Angstroms

This layer serves as the contact layer for collector.

Undoped GaAs buffer layer 2000 Angstroms

This layer helps keeping the defect density of the actual epitaxial structure low.

S.I. GaAs substrate {100} oriented

The substrate is semi-insulating. Crystal orientation is {100} to allow proper orientation of transistor mesa isolation patterns with connection metal patterns. The correctly oriented mesa hills will have positive slopes in the direction where metal connection wires enter the mesa hill. This increases the reliability of the process as metal breaks are avoided.

3.4 Crystal Orientation

During conventional transistor processing the separate devices are electrically isolated from each other by removing the conductive epitaxial layers between the devices. In Figure f30 this means etching away the emitter, base and collector layers. The active devices look like hills, or “mesas”, on a semi-insulating substrate. The height of a mesa is typically 1 ... 2 micrometers. The mesas can be etched either by dry etching or wet chemical etching. In either case the two important characteristics that need to be controlled over are the etching depth and the profile of the etched mesa. In this HBT process the etching is based on citric acid and hydrogen peroxide.

The citric acid etching solution is made by adding 121 g of anhydrous citric acid crystals to every 100 ml of deionised water [r09]. The crystals dissolve to water rather slowly, so the solution is made preferably many days in advance the actual etching steps. The etching speed for GaAs is controlled by adding a specific amount of hydrogen peroxide to the solution. 1 ml of 31% H_2O_2 to every 100 ml of citric acid solution would give etching speed of roughly one monolayer per second. The etchant temperature was kept on 20 ^{0}C.

The etchant is anisotropic in nature making the profile of a mesa hill to depend on its orientation according to the wafer crystal lattice. Figure f35 shows how the mesa side slopes are etched on a {100} oriented GaAs wafer with respect to the orientation flats. As a rule of thumb, the direction of a smooth step over and thus the preferential entrance direction for a metal wire to a mesa hill is perpendicular to the major flat of the {100} GaAs wafer.

During the processing of experimental HBT structures it is sometimes preferred to cut the wafer to smaller entities before the actual processing to make several samples out of one wafer. It is then important to be able to verify the correct orientation of the sample before the alignment marks are made on the surface. An easy way to accomplish this is to etch rectangular test patterns to the boundary areas of the sample by using, e.g. citric acid and hydrogen peroxide in dilution of 10 : 1. Figure f36 shows the result after 15 min of etching. The etching depth was about four micrometers. The proper orientation for metal wires would be on horizontal direction for this sample. A small pin hole in the protecting layer would yield to a structure like in Figure f37.

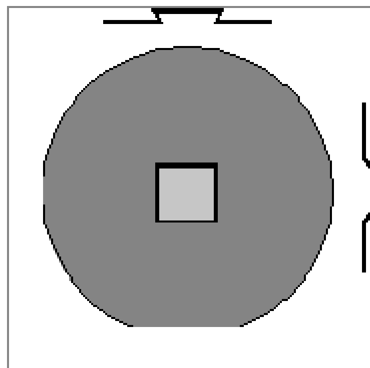

Figure f35: The mesa hill side slopes as etched on a {100} oriented GaAs wafer with respect to the orientation flats.

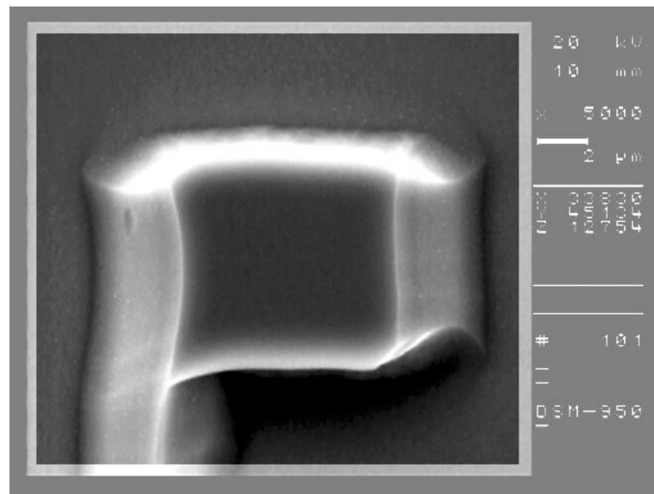

Figure f36: Orientation etching result after 15 min on citric acid : H_2O_2 with 10 : 1 dilution. The proper orientation for metal wires would be in horizontal direction.

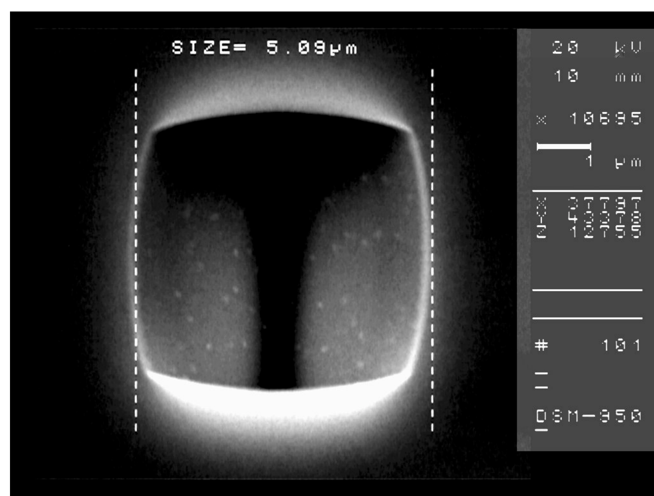

Figure f37: Orientation etching through a pin hole in the protecting layer. The direction of the sample was the same as in Figure f7.

3.5 Processing Steps

The processing steps for traditional HBT structures are explained in the following section. The process is tailored for the set of equipment that were in use at Electron Physics Laboratory of Helsinki University of Technology at the time of writing. Among the common laboratory equipment, the most crucial apparatus was a properly calibrated profilometer (Dektak 3 ™ by Sloan Technology). It was used in verifying the correct etching depths for mesa patterns. Most important for successful GaAs processing is to avoid any sources of unintentional scratches on the periphery of the sample. If a scratch was there, a GaAs sample barely holds its own weight when lifted up from corner. That is why every processing step was done using plastic tweezers only. Fixing the sample to evaporation holder for metallisation or into a quartz boat for heat treatment was done with extreme care. Any unnecessary "treatment" of the samples during the process was avoided.

The basic HBT process developed for this thesis contains 9 mask levels including a mask for alignment marks, 3 levels for mesa patterning, 3 levels for different kinds of metallisations, a contact hole mask and a mask for passivation nitride pad openings. Additional mask levels that were included to increase the process applicability were a mask level for patterning metal cross overs in more complicated devices, and a mask level for patterning air bridge structures. The basic lithography that was used for processing is explained in a separate booklet [r26]. The design of a mask set should take into account that connection metal wiring is allowed to enter the device mesa hill from the direction of smooth slopes of mesa hills only to avoid metallisation breaks. Alternatively, air bridges should be used for entering the mesa hill.

The processing involves surface cleaning prior to any wet chemical etch or metal deposition. If the surface contained any residuals prior to a wet chemical etch, the etching depth would differ throughout the sample area. After storing an initially clean gallium arsenide sample for 4 days in a shelf, the surface would contain about 30 Ångströms of different oxides of gallium and arsenide [r32]. Arsenic oxides dissolve readily to water, and gallium oxides dissolve to alkaline solutions but relatively slowly to acids [r33]. In this process uniform and repetitive wet chemical etching was initiated by the following treatment:

Dip in deionised water for 5 seconds for wetting the surface.

Dip in mild ammonium for 30 seconds to attack gallium oxides. The dip contains one part of 25% ammonia solution (M=17,03g/mol, 1L = 0.91 kg) to 85 parts of deionized water.

Dip in deionised water for 5 seconds to dilute out ammonium from the sample.

Dip in 1:1 solution of hydrochloric acid and deionised water for 30 seconds.

Dip in deionised water for 5 seconds to dilute out HCl.

Wet chemical etching is then started immediately after the rinse. Another way of preparing the surface would be to dip it on a strong HCl solution until the surface is hydrophobic.

3.5.1 Alignment marks

After verification of the correct alignment of the sample with respect to the mask, alignment marks are patterned using the lift-off method tailored for AZ5214E-resist and AZ400K developer. A Cr/Au-metallisation with 100Å of chromium and 500 ... 1000 Å of gold serves the purpose. Chromium is used as an adhesion promoting layer between the surface and gold. This mask level can be used also for patterning emitter contact metallisation for self-aligned base metallisation scheme (SABM). Self aligned bases use emitter metallisation as etching mask of emitter mesas. With wet chemical etching the emitter metal influences the etching process ("galvanic effect") making the method less controllable. In self aligned methods, dry etching is preferred. The mask set for this thesis contained several SABM structures with emitter contact metal depending on the choice of alignement metallisation. Galvanic effect seemed not to be a concern with with Cr/Au emitter metal. Just prior to evaporation of metal, the sample surface was cleaned by the method described above. If the cleaning was not successful, the alignment pattern adhesion will fail either in ultrasonic cleaning during liftoff or successive processing steps.

3.5.2 Emitter Mesa Pattern

The patterning is done with lithography tailored for AZ5214E and AZ 351B developer. The lithography is finalised by a mild post bake in 120 ^{0}C for 30 min to make the resist boundaries adhere more tightly to the surface. Without baking, the etchant would occasionally find its way under the resist making the mesa periphery imperfect.

The emitter etching is initiated with the dip cleaning sequence described above. The etchant solution consitutes of 1 ml of H_2O_2 in every 100 ml of citric acid solution. The etchant temperature was 20 ^{0}C. This solution will attack the sample roughly one monolayer per second. The etchant was made from pre-diluted citric acid liquid every time as it was needed, as the actual amount of hydrogen peroxide would not have been controllable if the etchant was stored long periods of time. It was proven very important to mix the etchant properly before use. The citric acid liquid is rather viscous, and the hydrogen peroxide does not mix unless the etchant is thoroughly stirred. The adhesion of AZ5214E resist would not hold against direct contact to hydrogen peroxide. With epitaxial structure like in Figure f32, the target is to remove about 2400 Å of capping and emitter material while the underlying base layer is only about 1000 Å thick. As the etchant is not selective between emitter and base layers, one has to be rather careful not to etch excessively deep or to stay too low. Etching is best done in two steps, making an intermediate measurement about the etching depth with profilometer from definite check points, and adjusting the second etching time accordingly. After the resist removal, the final etching depth is verified for future reference. Successful depth measurements call for proper calibration standards with the profilometer apparatus. In this process the measurements were done against a nominally 943 Å calibration standard with a certified systematic error of 15 Å at the day of calibration, December 19, 1996. The etching depth may be verified locally by checking the breakdown voltage of a mechanical probe needle contact with exposed semiconductor. Lightly doped n-type emitter would give a breakdown voltage in the order of 10 V, but heavily p-type doped base would be practically a short circuit [r14].

3.5.3 Base Mesa Pattern

The lithographic process for base mesa patterning is the same as for emitter mesas. The 2400 Å emitter mesas are shallow as compared to the resist AZ5214E nominal thickness of 1,4 micrometers, so no planarisation is not yet needed. Post baking step should again be included. Referring to Figure f32, the base mesa etch depth should be about 7000 Å, if the emitter mesa etch was done accurately. Any discrepancies on emitter mesa depth should be taken into account when etching the base mesa so that the sub-collector region is fully penetrated.

3.5.4 Emitter and Collector Ohmic Metal

After base mesa etch, the overall mesa hill will be about 8400 Å high with the structure as in Figure f32. That is about half the nominal thickness of AZ5214E resist in the standard lithography. The sample surface is planarised with the method described in reference [r26] during the lithography to allow smooth step coverage and controlled line widths over mesa regions. Post baking is not needed here. Prior to evaporation of ohmic metal, the surface oxides need to be removed. The dipping as described before may be used, preferably assisted with a short ion milling step prior to evaporation.

One of the important figures of merit of an HBT is the maximum frequency of oscillation f_{max}. It is maximised if the transistor active area is kept minimal. This calls for a very small area emitter. Typically, the emitter may be just a few micrometer square. Still, the emitter should be able to supply the transistor bias current without excessive series resistance loss. This translates to an extremely low resistance ohmic contact. With specific contact resistance of $1 \cdot 10^{-6}$ Ωcm^2, an emitter with one square micrometer area would have a series resistance of 100 Ω. With a bias current of 10 mA this would generate voltage drop of 1 V. For this thesis the emitter and collector ohmic metallisations were done simultaneously. The contact needs to be shallow in nature to prevent ohmic metal from penetrating the heterojunction. In GaAs-MESFET technology n-type layers are often contacted using eutectic gold-germanium (AuGe) based alloyed contacts that may penetrate several thousands of Ångströms into GaAs [r34]. AuGe is thus avoided in HBT designs with shallow emitters.

HBT structures without InGaAs-capping layer in emitter may use, e.g., Pd-In-based contact metallisations [r31]. With InGaAs layer included, a tri-layer of nonalloyed Ti/Pt/Au is often used to form a tunnelling contact. Ti serves as an adhesive and Pt prevents gold from diffusing into the semiconductor. The evaporation may be preceded by in-situ Ar+ ion bombardment to remove the interfacial oxides from the surface. Specific contact resistances in 10^{-8} Ωcm^2 range have been achieved with the ion bombardment method [r35]. Using a Pd/Ge bilayer, shallow contacts to InGaAs with specific contact resistances in 10^{-7} Ωcm^2 range have been demonstrated [r36]. For simple needs, a Cr/Au contact metal might be enough [r37], [r38]. Here chromium serves as an adhesion promoter between the sample surface and gold layer. Additionally, it should prevent gold and gallium from intermixing during subsequent heat treatments. Gold and gallium form liquid phases at temperatures over about 340 ^{0}C, as can be seen from the Au-Ga phase diagram in Figure f38 [r39]. With arsenic a liquid phase is found at about 640 ^{0}C. It is thus of crucial importance that direct contact with Au and GaAs surface is avoided if one wishes to maintain shallow ohmic contacts during any heat treatment.

The collector contact has typically much more area than emitter, and low contact resistance is not as important. Sometimes the collector contact is accomplished by a Schottky diode. A Schottky diode in transistor collector junction would be forward biased during the normal operation of transistor. GaAs-based Schottky diodes are very fast and do not affect the transistor high frequency performance [r08]. In this thesis, both emitter and collector contact areas were defined in a single mask step, and the collector contact formed a Schottky diode with properties that were dependent on the metallisation choice done in favour for reducing emitter contact resistivity. Electron beam evaporation of metals like Pt, Ti, or Pd may need a rather heavy beam current. In that case there is a risk of burning the resist while evaporating. Burned resist could in principle be removed with oxygen plasma, but at least with the equipment in our laboratory that took a very long time, and the sample was generally heated strongly during the treatment. Especially with fast diffusing dopant atoms like zinc or beryllium in the HBT base layer, heating over a few hundred degrees Celsius for extended period of time would be bad for the heterostructure. Usually, if the resist burned, the sample was considered to be lost. In some extreme cases a quick recovery trial may be applicable. Treating the sample with undiluted AZ400K developer in ultrasonic bath may lift off the resist in some minutes. If so, the sample surface is then finished with a relatively short oxygen plasma etch.

As Au

Assessed As-Au phase diagram (constrained vapor pressure).

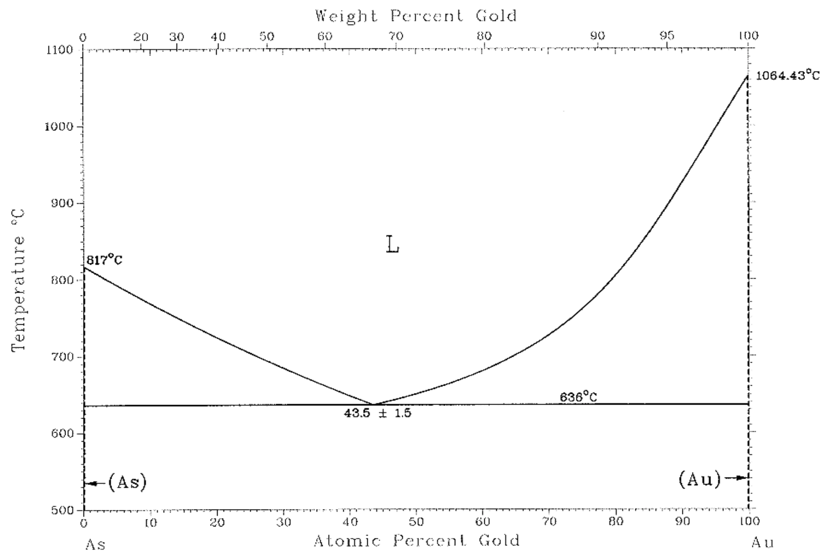

Au Ga

Assessed Au-Ga phase diagram.

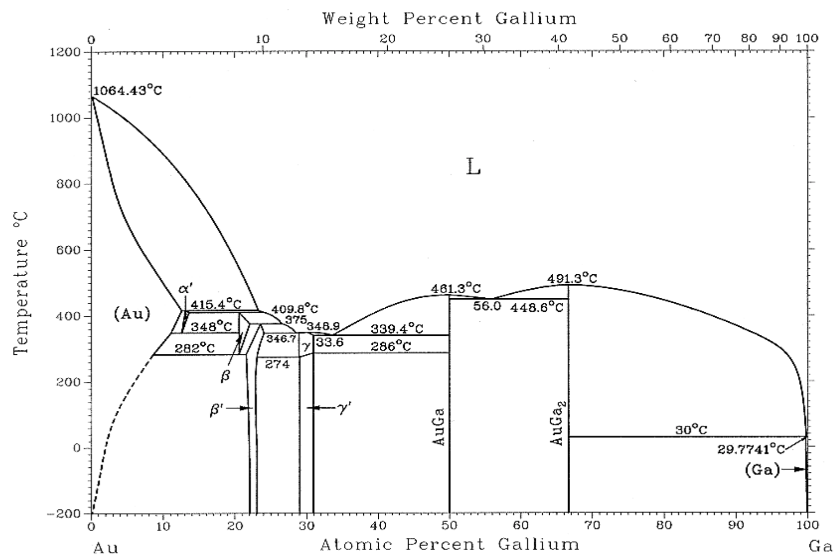

Figure f38: The phase diagrams of Au-As and Au-Ga systems [r39].

The ohmic metallisation is usually finalised by rapid thermal anneal. If the anneal was similar to the base ohmic metallisation, they are then preferably done simultaneously. While annealing GaAs, one should recall that GaAs surface decomposes in temperatures exceeding about 600 ^{0}C. To prevent arsenic atoms from escaping the surface during anneal, a silicon nitride capping layer is sometimes used with high temperature anneals. For this thesis the annealing temperatures were kept lower than 550 ^{0}C to minimise the decomposition problem.

3.5.5 Base Ohmic Metal

The base ohmic metal patterns are defined before etching collector mesas to benefit from the more shallow mesa hill. Lithography is of planarising type and similar to the previous step. Prior to evaporation of ohmic metal, the surface oxides need to be removed. With heavily p-type doped GaAs base, a typical choice for contact metallisation is Ti/Pt/Au [r35], [r40]. If the base layer was graded to reduce the carrier transit time, a Pt/Ti/Pt/Au metallisation may be adopted to facilitate contact formation to presumably oxidised AlGaAs surface of base [r41]. If the base layer was thick enough, also AuBe or AuZn alloys have been used. On evaporation of alloy material one should recall that resistive evaporation will not yield to homogenous metal film with material ratio of the source because of difference in evaporation rates of metals. Resistive evaporation may be applicable only if all of the source material is evaporated at once and the metal film was remixed during subsequent anneal. Alloyed source material is best evaporated using electron beam evaporation method. As an example, e-beam evaporation of AuZn alloy with 5 %wt Zn from a carbon crucible resulted a film of AuZn with 3,9 %wt Zn according to RBS measurement. Because of the carbon crucible, the film contained also about 5%at carbon.

3.5.6 Collector Mesa Pattern

Lithography here is of planarising type, and tailored for mesa etching. Post baking is again used to prevent the etchant from finding its way under the resist pattern making the mesa periphery imperfect. From Figure f32, the etching depth would be 8000 Å. After etching the devices should become isolated electrically. This may be verified by probe measurement on defined test points on the chip.

3.5.7 Insulation

After collector mesa etch the sample is ready to be coated with insulating material. In this process the insulation is accomplished by plasma enhanced chemical vapour deposited (PECVD) silicon nitride. During deposition the sample is kept at 300 ^{0}C temperature. The thickness of deposited insulation was typically 150 nm.

3.5.8 Contact Holes

In this process the contact hole pattern in the mask consists of 2 µm x 2 µm holes with 2 µm separation. The area that is to be contacted is filled with the dot pattern. Lithography is again of planarising type, tailored for contact hole patterning. After development, the contact holes on the resist will look like round circles. The hole pattern is then transferred to silicon nitride insulation layer by chemical plasma etching (CPE) with sulfur hexa fluoride (SF6). Figure f39 shows a SEM picture of an HBT just after opening the contact holes through nitride. The grainy contact metal is seen through the contact holes.

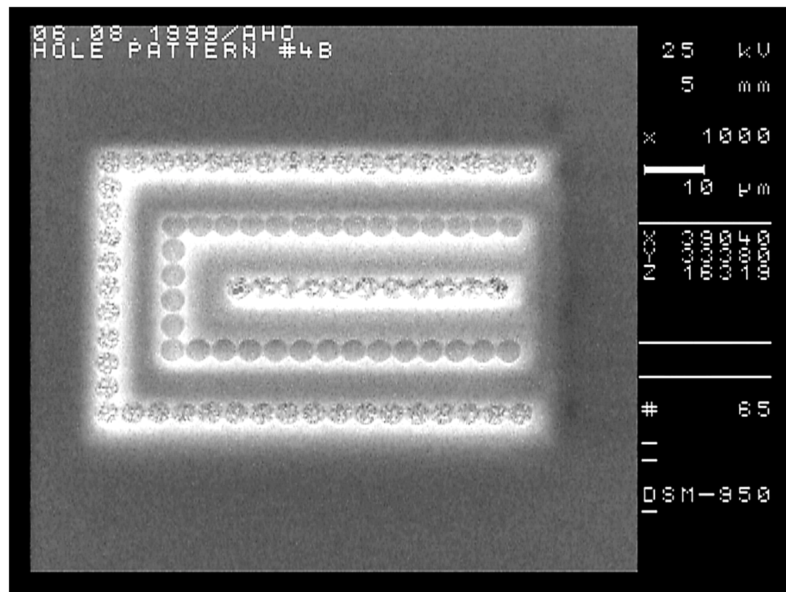

Figure f39: An HBT after contact hole etching step.

3.5.9 Wiring Metallisation

Wiring metallisation connects the device terminals with their contact pads. In some processes the semiconductor surface is planarised by, e.g., polyimide coating before wiring lithography. In this process the planarisation for wiring lithography is accomplished by a double layer of resist AZ5214E. Both resist layers may be patterned separately to form, e.g. air bridge structures. Similar kind of double layer lithography scheme was used with MPR1470 resist by Kazuhiko, T., et al. in reference [r42]. Wiring metallisation patterning is the most demanding lithography step on this process. While being planarising, the lithography has to maintain good line width control simultaneously on mesa regions (shallow resist) and field areas (thick resist). Yet the resist profile has to maintain a shape that is suitable for lift-off metallisation. In this process the metallisation is typically Cr/Au with 100 Å of chromium and 3000 Å of gold. For applications where the resistance of connector wiring is a concern, the wiring metal is made thicker. Preliminary tests on using electroless plating of copper in strengthening of the wiring metallisations were also examined as future addition to the process with encouraging results. Plating studies were not included in this thesis to avoid excessive divergence of the subject. Figure f40 gives an example of wiring into a transistor structure. The base contact in this example was split in two and connected together with a wiring metal crossover. Entrance to mesa hill was done by air bridges for emitter and base.

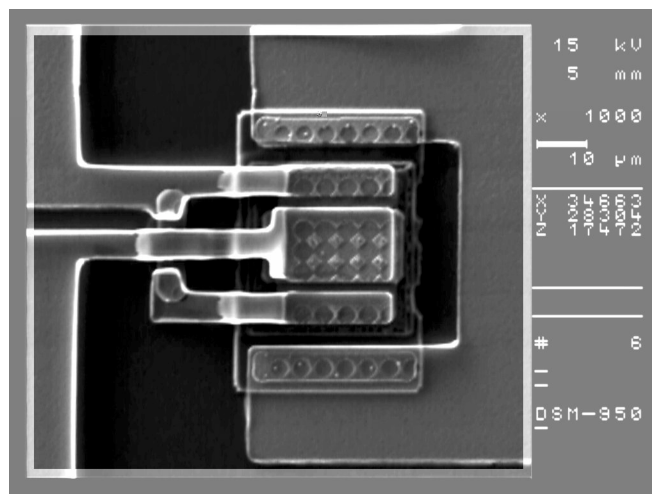

Figure f40: A transistor with a split base contact and air bridges in wiring metal.

3.5.10 Passivation

The insulation formed in step (3.5.7) shields the devices against contamination while forming the dielectric for capacitor structures. The final passivation step is included here to give the wiring metallisation in field areas of the sample mechanical shield against scratches. The passivation layer is again of silicon nitride. It should be noted that the scratch shield is not enough to protect the active areas of the sample, especially if the structures include air bridges. Care has to be taken in order not to ruin the samples mechanically before encapsulation. The samples do not survive if they were occassionnally flipped over on a flat surface.

3.5.11 Pad Opening

This step forms openings over contact pads and is made the same way as contact holes were made in step (3.5.8). After this step the sample is ready for probe measurements or wire bonding and packaging.

3.6 Naming Convention of the Processed Devices

All the processed devices were named with a self consistent manner in order to keep track of the various measurements and experiments that were done to the processed devices. The process runs were numbered cumulatively, and sample in runs were named alphabetically, e.g., A, B, and C. The chips on each processed samples were numbered by position on the sample, and each structure on the chip was number by the position in the chip. The name of a specific structure was then constructed by run, chip and structure type. For example, name HBT02-C:2403 refers to process run 2, sample C, chip 24 and structure 3. To maintain consistency, the naming convention is preserved in the Figures of this thesis for easy identification of the structure under study.

3.7 Test Structure with Loose Tolerance Design

Transistor geometry has to be optimised for high speed operation. Any stray capacitance and series resistance or inductance should be minimised. Figure f41 shows an illustrative example of an HBT layout with no special optimisation. This is the "loose tolerance" test structure from the basic HBT mask set. The emitter mesa size was 20 μm x 20 μm. There is no air bridge under the emitter wire for smooth entrance to emitter mesa over the boundaries. Only the preferential slope on mesa boundaries prevents the wire from breaking up.

The active region of the transistor is under the emitter mesa. Electrical path between the base contact and active region is relatively long and resistive. Self aligned base metallisation processes (SABM) would help reducing this parasitic base series resistance. A trial SABM process is included in the mask set. Also, the base surface is vastly exposed provoking surface recombination. Usually, if the base surface was exposed, it would be passivated, e.g., using a p-doped AlGaAs capping layer that repels charge carriers from the surface [r30]. As the surface recombination current is suppressed, the total base current that is needed for transistor biasing to operation point is reduced.

Not shown in the picture are the respective contact pads for emitter, base and collector. Additional series resistance will be generated by the resistivity of wiring itself. Although of gold, the wiring metal has to be thick and wide enough to minimise the series resistances. In our experience, the measured resistivity of e-beam evaporated gold wiring of 100 nm thickness was about four times the bulk value of gold. A 10 μm wide wire of 100 μm length and 100 nm thickness would then have a series resistance of 9,4 Ω. Finally, base and emitter wires have to travel on top of collector mesa for quite a long way with 150 nm of nitride isolation in between. Thus a considerable capacitance is formed between the legs of the transistor in addition to the intrinsic capacitances. Although of no use in applications, this example structure is good in checking out the parasitics of the transistor process. Loose alignment tolerances allow the structure to function electrically even with relatively huge alignment errors during the process. As a consequence, it has been usually the first structure that is tested out after an experimental HBT process.

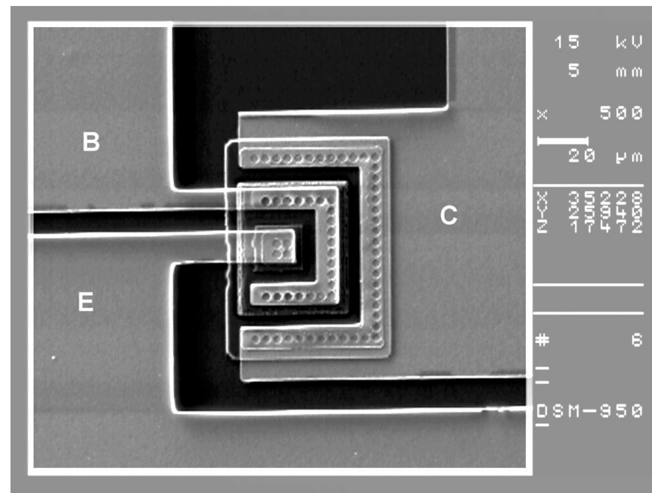

Figure f41: SEM picture of an HBT structure with loose tolerance design.

3.8 Choice of Contact Metallisation Material

Various ohmic metal compositions were examined during the early efforts of process development [r27]. The first transistor structures were with Zn-doped base layer and Pd/In-ohmic contacts for emitter and collector. InGaAs emitter capping was not yet present. The base contact was AuZn-based. The first structures showed rather poor DC characteristics with current gain barely exceeding unity. It was found out that the samples were very sensitive to heat treatment, and emitters were typically corrupted before ohmic contacts were formed during rapid thermal anneal. The emitter layers were then redesigned to include InGaAs capping, and any heat treatment other than implicit in, e.g., PECVD nitridation and e-beam evaporation was avoided. A very simple metallisation with Cr/Au on every contact was chosen as a base line reference (sample A). The epitaxial structure was as described in section 3.3. It was expected that emitter should have a fairly good ohmic contact with Cr/Au because of InGaAs capping. The Cr/Au -base contact should also become ohmic because of tunneling effect. Collector contact would be a more or less leaky Schottky diode which should not hinder the transistor operation, as the diode would be forward biased in normal transistor operation. Reverse Gummel plots would be severely affected because of the diode.

The collector diode suppresses reverse collector current which otherwise would equal the base current in measurements with forced base current. In structures with a very low current gain the reverse current would fit the same scale as the forward current and is visible unless there was a diode in the collector leg. This should be kept in mind when examining the measured IV-graphs, as the actual current gain can not be deduced from the graphs visually because of the collector diode. The graphs may look impressive even if the structure has a relatively poor current gain. Figure f42 gives typical measured collector characteristics of the reference structure. The collector has a Schottky diode as expected from having Cr/Au on moderately doped n-GaAs. The diode did not leak considerably.

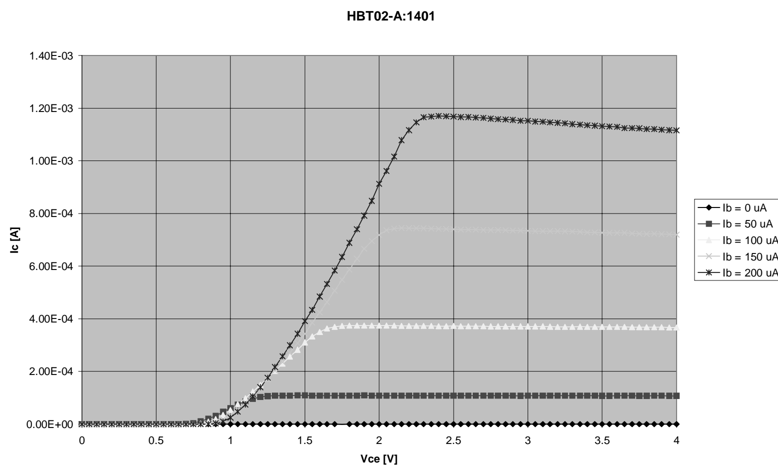

Figure f42: Typical collector characteristics of the test structure with non-alloyed Cr/Au contacts on emitter, base and collector.

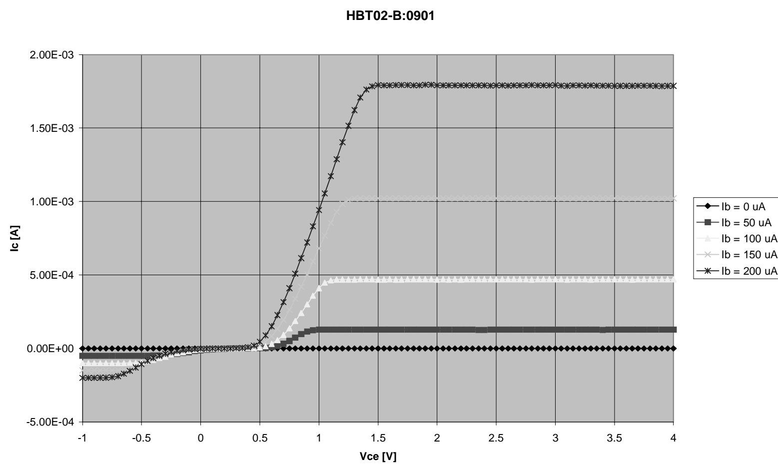

Figure f43: Typical collector characteristics of the test structure with Pd/Ge/Pd/Au n-type contacts and Cr/Au base contact.

Another sample was prepared with Pd/Ge/Pd/Au n-type contacts and Cr/Au base contact (sample B). The typical collector characteristics is shown in Figure f43. The negative currents were already partially visible, although the contacts were not fully ohmic. It is probable that a moderate anneal for this structure before PECVD step would have formed an ohmic contact to collector. Typical current gain was about 10. Some transistors on the sample showed current gains exceeding 30 because of process variations.

An effort to make a sample with Pd/AuGe/Ag/Au n-type contacts and Ni/AuZn base contact was also done (sample C). During e-beam evaporation of nickel the sample was over heated to an undetermined temperature and the resist was burned. The temperature exceeded AZ5214E resist burning limit of 120°C for several minutes. The sample was treated with the AZ400K method as described in paragraph 4.4. As a co-incident, the collector ohmic metal adhesion was found to be rather poor and it was ripped off during ultrasonic bath. Thus, even though there was no separate mask levels for emitter and collector ohmic contacts, it was possible to test out a method of making the collector contact directly with wiring metal Cr/Au through contact holes, presumably with some residuals of Pd on the collector surface. Also, the emitter contact had been unintentionally moderately heated by the failed Ni deposition. The opportunity encouraged to proceed the experiment forward even though the sample was considered lost.

The typical collector characteristics of the test structure is shown in Figure f44. The structures performed very good as compared to basic structure of Figure f42. From the Figure f44 it is seen that the slope of the curves are very steep, suggesting acceptably small series resistance on emitter and collector contacts. The collector contact was a diode. In the current range of Figure f44 the measured current gain was again about 10. The current gain of an HBT may increase with the collector current density. Low series resistance in this sample allowed the measurements to be done with more heavy current level without excessive resistive voltage drops. Figure f45 shows the transistor collector characteristics for base current up to $600\ \mu A$. The current gain approached 40 with collector current level of 20 mA.

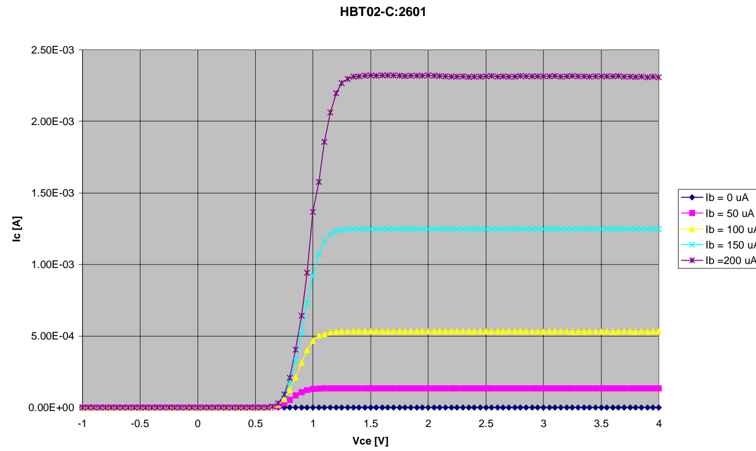

Figure f44: Typical collector characteristics of the test structure with Pd/AuGe/Ag/Au emitter contact, Cr/Au dot matrix collector contact and Ni/AuZn base contact.

3.9 Self Heating Effect

The negative differential dependence of collector current to collector voltage that is typical for AlGaAs/GaAs HBTs is clearly visible in Figure f45. Measured with a HP4155A parameter analyser, the dependence was the same whether the measurement sweep was short, medium or long. The negative slope is associated with the self heating effect of the transistor. The power that is dissipated inside the transistor is the product of collector current I_c and collector voltage V_{ce}. To first estimate, the temperature inside the transistor active area increases linearly with input power [r43]. Device temperature may be modeled as

(e136)
$$T = 300K + R_{th0} \cdot I_c \cdot V_{CE},$$

where R_{th0} is thermal resistivity of the substrate.

In reality, thermal resistance R_{th0} is a temperature dependent variable itself [r14]. It is possible to relate R_{th0} analytically to material parameters, as is done in reference [r14], but for the purpose of this thesis the accurate treatment was considered irrelevant because of other simplifications involved with the simulation code.

Figure f45 shows the measurement result of a transistor with constant base current stimulus. Device simulations should also be done in constant base current mode, letting base voltage to drift as the device heats up. The voltage drop over collector Schottky diode should also be taken into accunt in the simulation to properly estimate power load of the actual transistor. In paragraph 2.13 it was briefly mentioned that constant base current simulations constitute of massive iteration of the device equations, as the equations are not analytically solvable for V_{be}.

Figure f46 shows the result of constant base current simulation for a transistor with doping concentrations and layer thicknesses as in the actual measured transistor, and with numerical value of R_{th0} = 500 K/W. Base current level was stepped according to the insert of figure f45. The numerical value of the thermal resistance was chosen after some initial iteration for proper slope in the IV-curve, and represents a typical value [r14], [r56]. The simulation was based on thermionic emission theory, excluding the electrons that would tunnel through the conduction band spike. To include the spike transparency calculation within the iteration loop, the simulation code needs still some refinement not to overload the computer memory. Also included in the simulation was a rough model for the observed collector diode to take into account the diode voltage drop in the collector current path. Diode model parameters were $I_S = 1 \cdot 10^{-12}$ A for saturation current, $n = 2$ for ideality factor, $R_S = 1\ \Omega$ for series resistance and R_{SH} = 1MΩ for shunt resistance. The self heating effect in collector current is readily seen from the simulation result of Figure f46. More accurate fit to the measured curve may be obtained after inclusion of thermionic field-emission theory into calculations, after which a better diode modelling may also become relevant. It is seen from Figure f46 that simple thermionic model gives qualitative information on the self heating effect of the transistor under study. It is worth mentioning that the simulated effect relies on proper modelling of band discontinuities between emitter and base. Equations (e13) were used in determining the band structure in the simulations for this thesis.

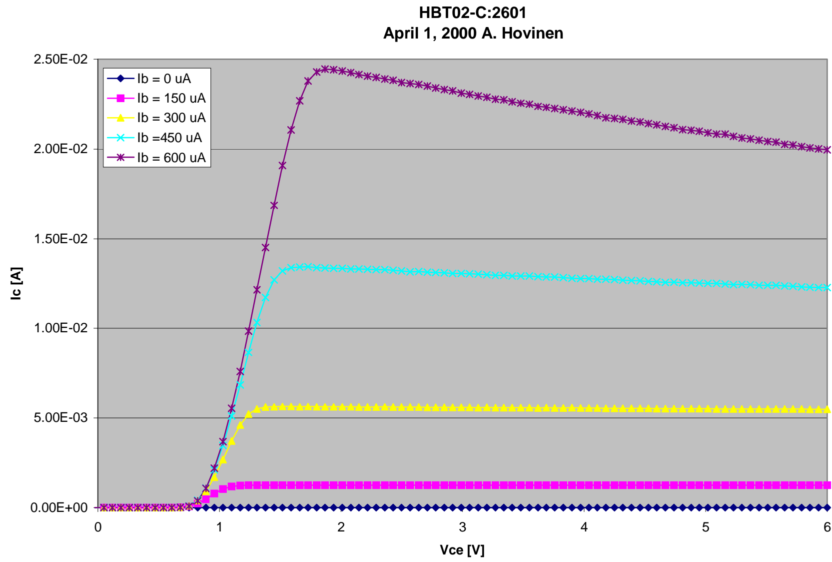

Figure f45: The transistor of Figure f44 with base current levels up to 600 uA. The resulting current gain was about 40 with collector current level of 20 mA.

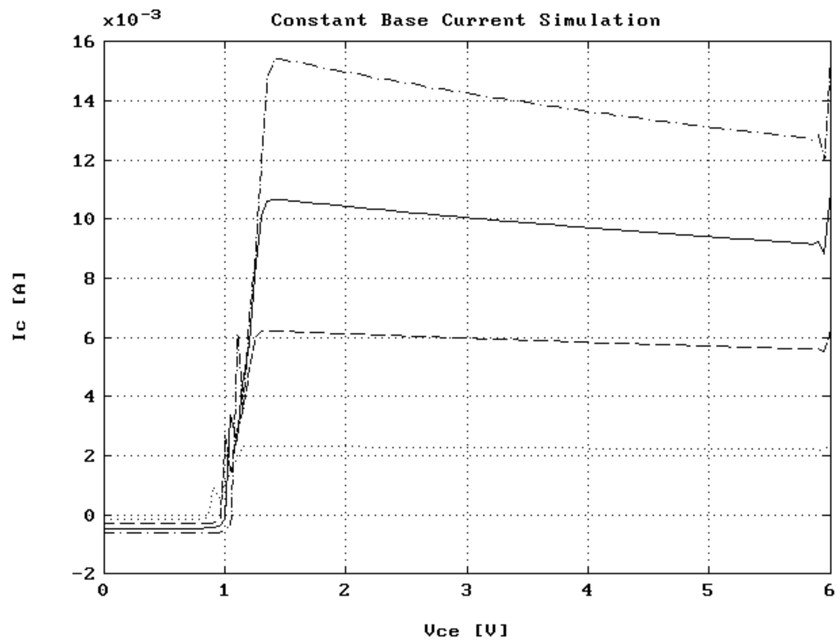

Figure f46: One dimensional constant base current simulation of the transistor with temperature effects, showing clearly the negative differential dependence of collector current to collector voltage. Doping concentrations and layer thicknesses were as in the actual measured transistor. Numerical value for thermal resistance was R_{th0} = 500 K/W. Base current level was stepped according to the insert of figure f45.

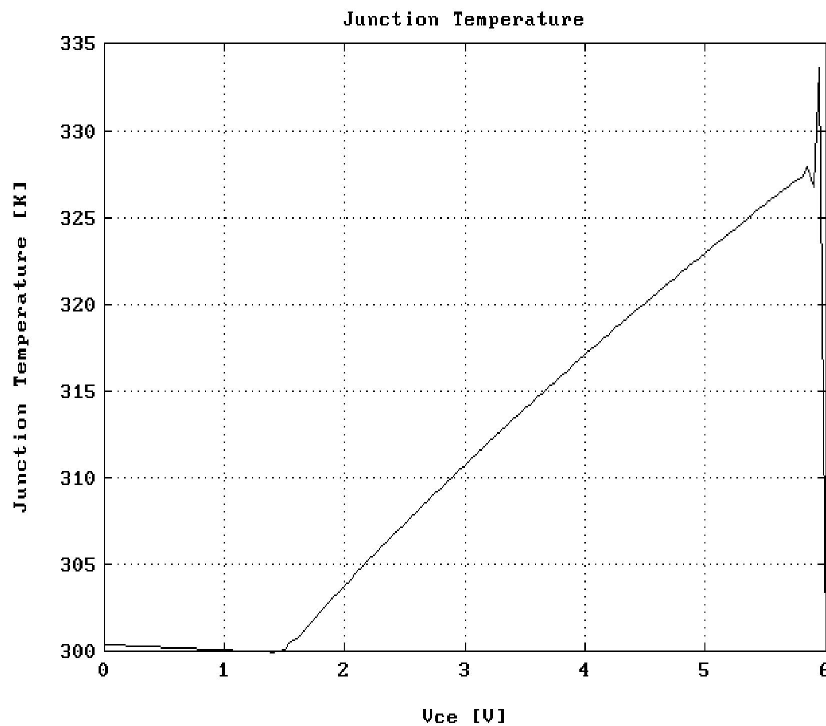

Figure f47: Junction temperature during the highest current sweep of simulation for Figure f46.

Figure f47 shows the simulated junction temperature during the sweep with 600 μA base current in Figure f46. The device heated up by 27 K with maximum power load during voltage sweep according to the simulation. The spiking around 6 V in the simulation is an artifact and comes from the simulation routine. The voltage sweep is simulated starting from high voltage and power with small voltage steps. Dissipated power is estimated from the result of previous simulation point. The first few points do not have proper estimate for input power, which is seen as spiking in the simulation results.

The collector diode was modelled in forward bias only during the simulation to take into account the power distribution between diode and transistor. The diode was disabled when collector current was negative during the simulation. That is why the negative part of the collector current is still visible in Figure f46. Future refinement of the simulation code may include more accurate modelling of the collector diode also in reverse bias.

4 Practical Measurements

4.1 Analysis environment

The main apparatus for direct current measurements of the test structures was HP 4155A parameter analyser with ICS Interactive Characterization Software™ by Metrics Technology. The apparatus was situated inside the H.U.T. clean room, which in essence is a Faraday cage with several high power radio frequency transmitters like PECVD inside. The measurements that needed low levels of environmental noise were done with HP4145 measurement setup outside the clean room.

Light sensitivity of the structures under "on wafer" study were examined as part of device probe measurements. Illuminated HBT is a photodetection device. The applicability of heterojunction devices in the field of high speed photodetection has gained growing interest during last decade. It was shown by *Suematsu and Ogawa* in [r44] that HBT–based photodetection is a competitive alternative to PIN-diode based photodetection in high speed applications. The absorption coefficient of intrinsic GaAs at room temperature for photons with energy exceeding the forbidden band gap width of 1,42 eV is about 10^4 cm^{-1} [r45]. This corresponds to absorption depth of about one micrometer. On the exposed areas of Figure f41 the photons are thus absorbed effectively by the base layer of 1000Å thickness and collector layer of 6000Å thickness. There is a finite spatial collection probability of generated electron-hole pairs for the reverse biased collector-base junction beneath the neutral base layer [r46]. Absorption in the neutral base layer increases the excess minority electron concentration, which reduces electron emission through heterojunction in low bias conditions reducing the phototransistor gain performance [r47]. Some of the electrical measurements were repeated under illumination to gain information on the severity of light pollution on the device measurements.

4.2 Connecting the Device to measurement

DC measurements were performed on manual probe stations with Tungsten needles. The series resistance over a needle tip during measurements was typically 4 Ω per needle according to short circuit measurements that were routinely performed before any transistor testing. Measurement pad connections were 100 μm x 100 μm squares. The pad metallisation was the same as used in wiring layer, typically 300 nm gold on 10 nm chromium. Scratching a contact pad during needle probing is inavoidable with the metal thicknesses of 300 nm or less. A device could typically be needle probed two or three times before the pad connection failed.

Some of the devices were wire bonded for more permanent study. Model *UZS.M-2.5* ultrasonic welding machine with 25 μm diameter aluminum wire was used. Processing of the measurement pad metallisation was not yet optimised for ultrasonic bonding, which allowed the bonding operation to become rather destructive. Typical bonding associated failure was metal rip off under the area of bonding, which could have been avoided by thicker pad metallisation. In some cases it was seen that improper cleaning of the silicon nitride surface prior to pad metallisation resulted in adhesion failure of the pad. The surface under bonding pads was not pretreated to promote adhesion. In forecoming processing efforts the pad metallisation should be refined to make wire bonding feasible. In this thesis the low yield of wire bonding step was not a concern, and transistors in a chip were ruined rather nonchalantly until a satisfactory bonding was achieved. Typically 5 devices were lost for every succesfully wire bonded device.

4.3 Extracting Equivalent Circuit Parameters from Measurements

Gummel plot is a tool for extracting transistor DC parameters for base and collector current. The Gummel measurement is performed by sweeping V_{BE} across the safe operation area of the device while keeping V_{CB} zero, and measuring terminal currents. Light sensitivity of the device may be seen from the low current region of the Gummel plot. Figure f48 compares room temperature measurement results of a device in dark and as illuminated by probe station microscope light. The non-zero measured current level of 30 pA in dark at zero base-emitter voltage is an indication of the systematic measurement error level of the measurement apparatus, not actual device current. It is seen that illumination generated about 3 nA “short circuit” current in the base-collector circuit.

Also shown in Figure f48 is the result of exponential fit of the base and collector currents of the transistor under study. According to the fit, base current obeys ideal diode law with saturation current $I_{s,base} = 4 \cdot 10^{-15}$ A and ideality factor $n_{base} = 1{,}935$. Device emitter area was 10 x 50 µm. Collector saturation current was $I_{s,collector} = 2 \cdot 10^{-23}$ A and ideality factor $n_{collector} = 1{,}067$. The ideality factors indicate that base current was mainly of space charge recombination current type, and collector current was of diffusion current type [r13]. The measurement also reveals that the device gain barely exceeded unity at current levels of 1 mA. This was because the rectifying collector contact was not forward biased during the measurement with $V_{CB} = 0$V.

Figure f49 shows a collection of Gummel plot measurement data of another transistor from the same chip. Device are emitter area was 6 x 26 µm. This time the base-collector voltage V_{CB} was varied according to the insert of Figure f49. It was observed during measurements that illumination did not affect considerably the collector current when V_{CB} was over 1V. However, currents measured in dark were seemingly swapped. Dark base current curve matched with the collector current curves with V_{CB} offset at high V_{BE}, and dark collector current matched with base current curves, although not as smoothly. The seemingly confusing result was related to non-ohmic collector contact, and was later verified with Spice-based simulations. The constant collector current with low V_{BE} bias came from leakage between base and collector. The leakage current dominated over "photocurrent" when V_{CB} was over 1 V. The distance between flat parts of the current sweeps is roughly constant in logarithmic scale, indicating that the leakage current obeys exponential law. Fit to measurement data at $V_{BE} = 0{,}6$ V gave leakage diode parameters $I_{s,leakage} = 5 \cdot 10^{-11}$ A for saturation current, and $n_{leakage} = 11{,}316$ for ideality factor. The high value of n indicates that voltage was actually not constant over the area of leakage, but in average only a small fraction of V_{CB}. High values of n are sometimes also justified, e.g., with recombination by series effect of tunneling through a potential barrier and recombination via junction interface recombination centers rising *tunneling-recombination leakage current* with ideality factor n approaching 4 in room temperature [r14].

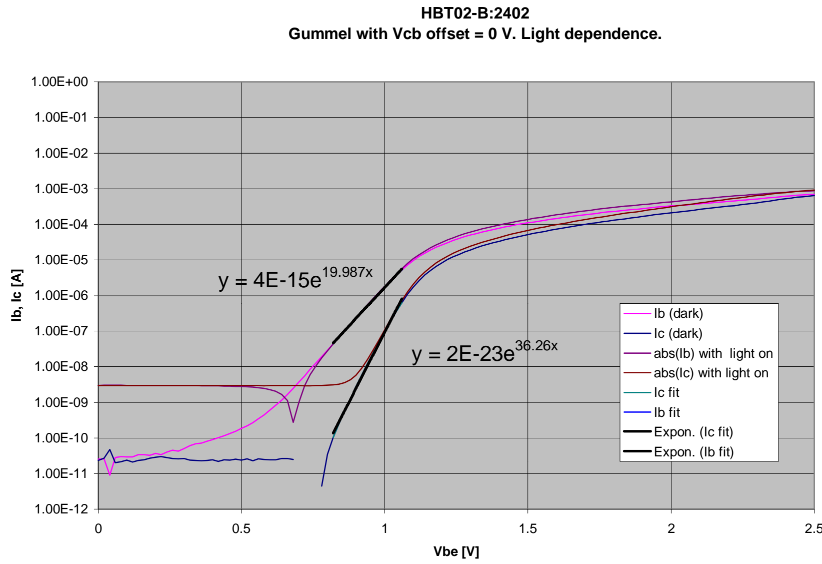

Figure f48: Gummel plot measurement of a transistor acting as a “photodetector”. Note that negative current data from measurement under illumination is converted to absolute value in order to be seen in logaritmic scale. Device emitter area was 10 x 50 μm

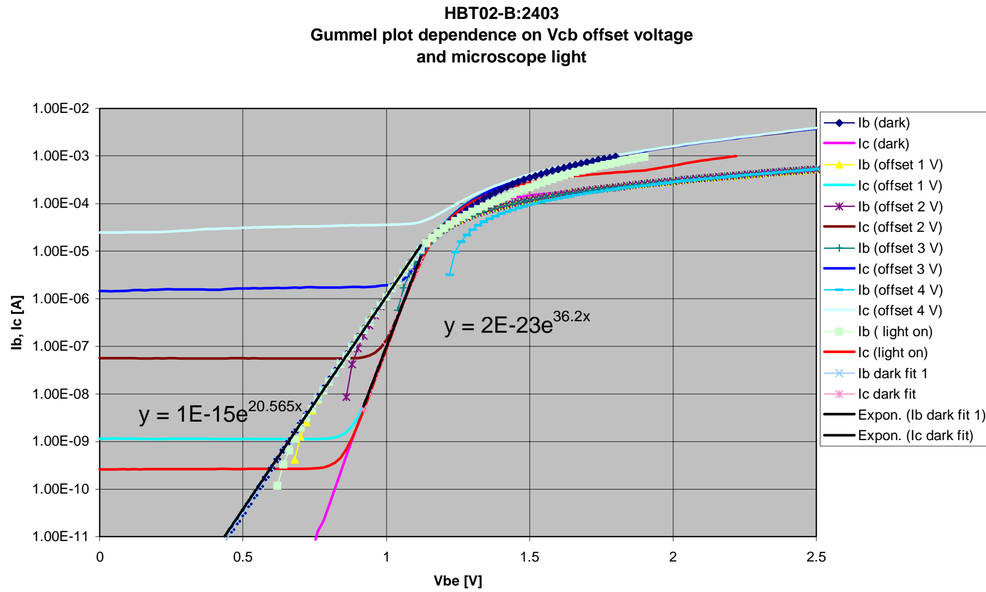

Figure f49: A collection of Gummel plot measurement data of transistor HBT02-B:2403. Device emitter area was 6 x 26 μm. The leakage of base-collector diode is readily identified from the plot.

Attempts to model the leakage current as reverse leakage across base-collector junction failed because of the distributed nature of the leak. The exponential dependence of leakage current on applied voltage V_{CB} ruled out generation current J_{gC} in the junction depletion region as a possible cause, although the direction of leakage current could support the assumption. Presumably the leak originated from surface effects. PECVD deposited silicon nitride does not passivate GaAs surface efficiently, and it is conceivable that base minority electrons and collector minority holes in the vicinity of base periphery may leak by the sides of the pn-junction using the surface channels in the periphery [r48]. The observed "photocurrent" in nanoampere scale may also be considered as periphery leak current instead of short circuit current of collector junction acting as a solar cell, for the simple reason that series resistances in the circuit blocked out the concept of a short circuit. Instead, the illumination increased the potential difference between base and collector layers by solar cell action to approximately *1 V* level, which in turn made leaking to occur under illumination. The measurement apparatus kept external V_{CB} at *0V*, while the light-induced voltage difference was over the reverse biased rectifying contact of collector. It may be concluded that the device process should include effective surface passivation if devices with perimeter of 6 x 26 µm or less are to be processed with intention to reach controllable collector operation under 100 μA level at V_{CB} of several volts.

Also shown in Figure f49 is the result of fitting the base and collector currents to ideal diode law. The base current may be modeled with $I_{s,base} = 1 \cdot 10^{-15}$ A and ideality factor n_{base} = 1,881. Emitter diode characteristics were also measured separately and fitted to a diode model including series resistance R_s [r49]. Extracted diode parameters were $I_{s,base} = 1{,}299 \cdot 10^{-15}$ A and n_{base} = 1,8941 with R_s = 453,415 Ω, including both emitter and base resistances. Emitter resistance R_e was extrated independently from end resistance measurement data giving R_e = 379,22 Ω. Base resistance was then R_b = 74,195 Ω . From the fit in Figure f49, collector saturation current was $I_{s,collector} = 2 \cdot 10^{-23}$ A and ideality factor $n_{collector}$ = 1,069. Separate collector diode measurements suggested that the base-collector circuit contained diodes in back to back arrangement, the first being transistor collector diode and the second being the rectifying collector contact. It was not possible to deduce diode parameters from the separate collector diode measurement. Instead, the parameters of the collector rectifying contact were extracted from transistor common emitter collector characteristics, shown in Figure f50. Transistor geometry suggested that the collector diode could be represented by two parallel diodes, as the transistor was of double side contacted type shown in Figure f40.

It was also found out that good fit was obtained only if the rectifying contact was modeled by two diodes in series. After splitting the collector diode, fit to measurement data was obtained with diode parameters $I_{s,contact}$ = $1{,}183 \cdot 10^{-12}$ A and $n_{contact}$ = 1,9321 with collector series resistance R_c = 11,684 Ω.

The measured device parameters were input to a pSpice simulation to confirm the numerical values. A demonstration copy of Orcad pSpice™ Student Version 9.1 was chosen as simulation platform. The circuit that was used in simulation is shown in Figure f51. Voltage and current sources and swithces SW1, SW2 and SW3 were arranged such that basic transistor measurements could be simulated with the same schematic page easily. The simulation goal was to match measured Gummel plot of Figure f49 and common emitter collector characteristics of the same device, shown in Figure f50.

The pSpice parameters for passive components that satisfy Figures f49 and f50 are shown in Figure f51. Figure f52 shows the simulated collector characteristics, and Figure f53 shows the simulated Gummel plot. Resistance values were rounded, and emitter resistance was lowered slightly from the measured R_e = 379,22 Ω in order to match simulation more perfectly to the measurement with high collector currents. The end resistance measurement seemingly over-estimated the emitter resistance by 10%. A 750 MΩ shunt resistor was included over base-collector junction to simulate the observed leakage in Gummel plot of Figure f49. Attempt to model the leakage behaviour more rigorously suggested that the shunt resistor should have been replaced by a voltage controlled current channel between collector and base. The resistivity of the current path should have reduced exponentially with increasing V_{CB}, reaching 10 MΩ level with V_{CB} = 4 V. However, such a refinement was not included in the final simulation for simplicity. The transistor was modeled by a pSpice *silicon* NPN device with DC gain of 23, IS = 2e-23, NF = 1.069, ISE = 1,299E-15 and NE = 1.8941. The junction built in potentials had their default silicon values of 0,75 V, because they do not contribute to the direct current calculation in pSpice simulation. ISE and NE properly modeled the current gain degradation due to space charge recombination in low current levels, as observed in Figure f50. It was not possible to join measurement data directly on top of simulation curves with the demonstration version of pSpice used, but visual comparison of Figures f50 and f52 suggests that the parameters were adequate.

4.4 Conclusive Remarks on the Process Run

The device under measurement was from a process with Pd/Ge/Pd/Au n-type contacts and Cr/Au base contact (sample B). Emitter areas for self aligned base metallization (SABM) structures were defined by Cr/Au contact layer. The device HBT02-B:2403 was a SABM device with Cr/Au emitter contact, Cr/Au base contact and Pd/Ge/Pd/Au collector contact. The contacts were not intentionnally heat treated, besides during the PECVD nitridation in 300 ^{0}C. The emitter resistance of a 6 x 26 μm device was 350 ohm, corresponding to contact resistivity of $\rho_{c,emitter} = 1,82 \cdot 10^{-4}\ \Omega\text{cm}^2$. The contact resistivity was about 100 times higher than acceptable for a high performance HBT emitter. The collector included series resistance of about 10 Ω, with total collector contact area of 2 x 16 x 42 μm. The base series resistance was 75Ω, including contact and bulk resistance. The base resistance value is acceptable for an HBT.

The collector current under low voltage bias obeyed ideal diode law only if it was modeled by two diodes in series with identical parameters. The model diode ideality factor approached 2 indicating that space charge recombination was the main conduction mechanism across the contact. Having two diodes in series was a necessity to simulate the observed high value of V_{offset}. It is conceivable that along the path of collector current there was in reality two regions in series where the conduction mechanism was through recombination centers, e.g. collector contact and some of the epitaxial interfaces in the current path. It has to be noted that the simulation result may be repeated after moving the other diode to the emitter leg of the transistor, indicating process-oriented problems with either the emitter epitaxy or with the emitter contact. In that case more refined simulation would have probably given difference in the diode parameters. The proper position of the nonlinearity may be judged by monitoring V_{BE} while measuring the device with constant base current stimulus. A diode in emitter leg would rise V_{BE} accordingly. For the transistor under study the measured V_{BE} was less than 2,8 V throughout the measurement of Figure f50, and accorded within 15% with values obtained from the pSpice simulation. This did not encourage moving the additional diode to emitter side of the transistor.

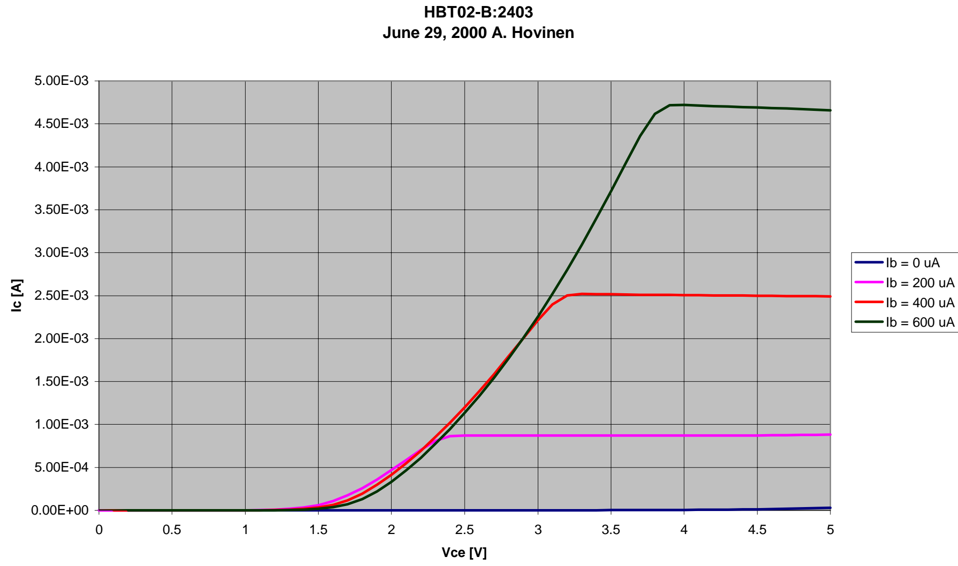

Figure f50: Measured common emitter collector characteristics of device HBT02-B:2403.

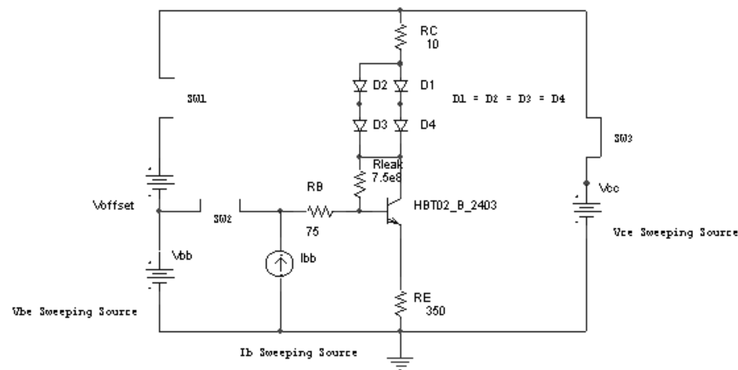

Figure f51: A simple DC model of transistor HBT02-B:2403.

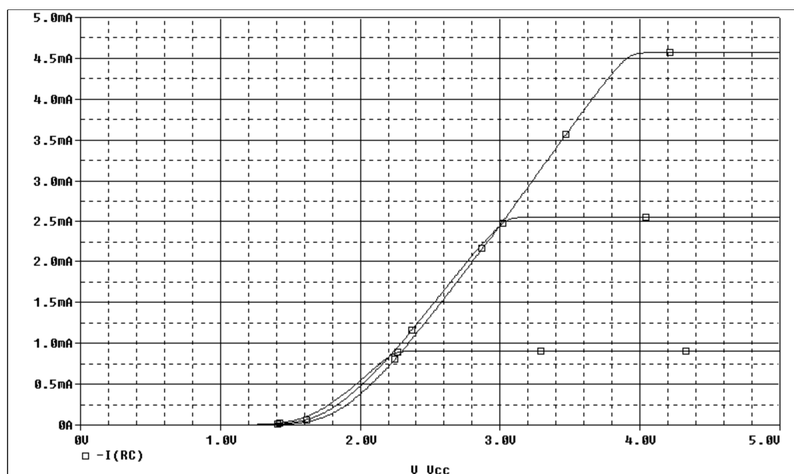

Figure f52: Simulated common emitter collector characteristics of HBT02-B:2403 using the pSpice model of Figure f50. This simulation should be compared with measurement results of Figure f51.

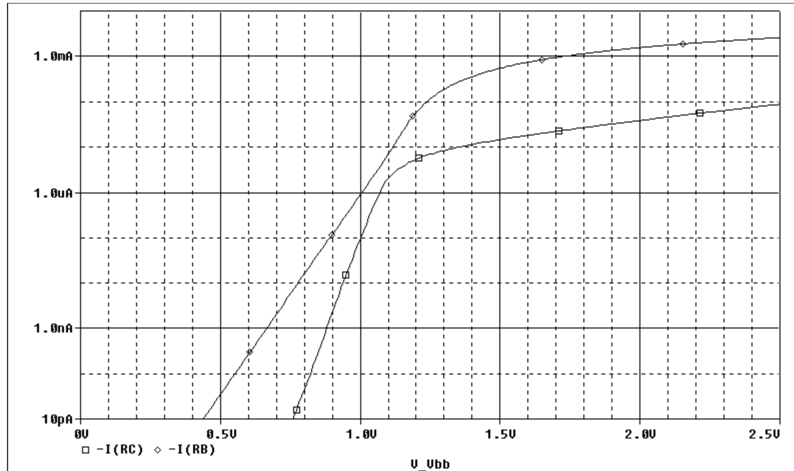

(a)

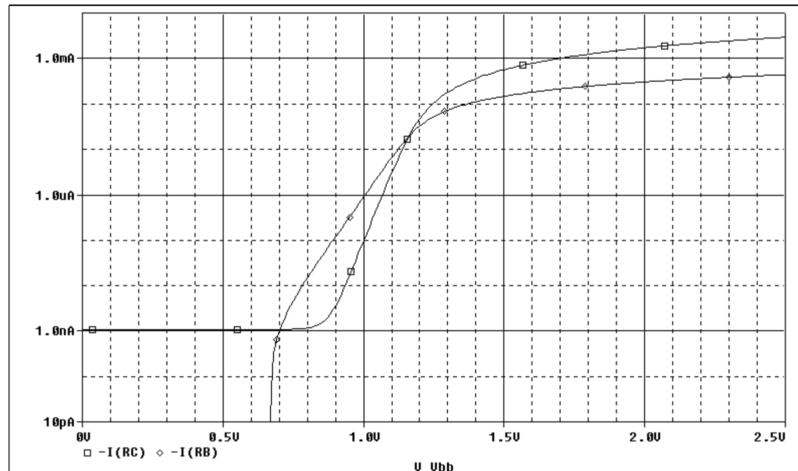

(b)

Figure f53: Simulated Gummel plot as obtained from transistor equivaled circuit of Figure f51. (a): V_{CB} = 0 V. (b) V_{CB} = 1V. Transistor did not have positive current gain unless V_{CB} was reverse biased because of the rectifying contact in collector.

Figure f53 alleviates the choice of proper biasing conditions for the processed devices. Application of transistors from process run “B“ in electrical circuits should take into account that in order to have current gain, the transistors need to be biased such that the rectifying diodes are forward biased in all circumstances. Typical operation point bias would be V_{CE} = 5V for the HBT02-B series.

4.5 Stability of the Measured Transistor Performance

One of the most important characteristic that governs over the applicability of a transistor process is the long term stability of the processed devices. An otherwise very attractive process scheme has to be discarded if the device does not give stable long term charateristics. At worst, the device properties may change as stocked in room temperature for a relatively short time. In any process development the device has to be evaluated against stability. As the main focus of this thesis was to examine the issues involved with actual processing, the long term stability question was not the principal motive force. However, while the time span of the practical work was quite long due to circumstances, it was possible to re-examine some early samples to monitor the possible degradation without actual temperature accelerated testing. Figure f54 shows collector characteristics of a sample from process run “C” as measured the day the process was completed (31-Ma-00) and six months later (30-Oct-00). It is seen that the nonlinear contact of the transistor is severely degraded over time. Special care was taken during measurements to achieve good probe needle contact to device. Poor needle contact would result to a similar looking result.

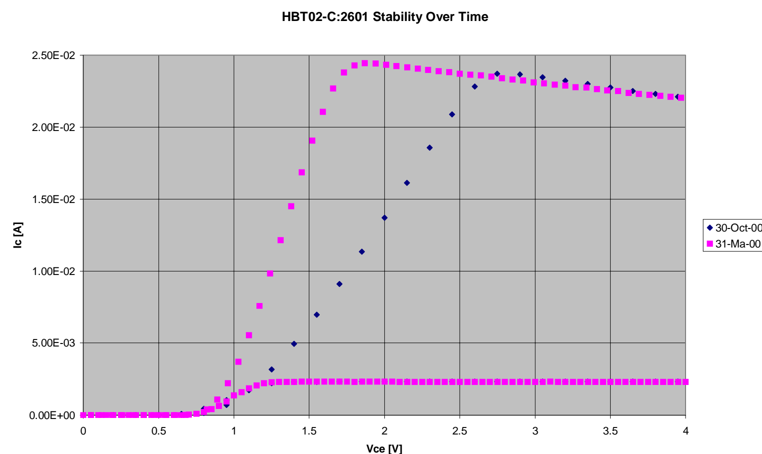

Figure f54: Worst case example of a device that suffers from unstable contacts.

The instability is understandable with reference to the process diary of the sample. During the processing of sample C the surface preparation prior to metal depositions may have been inadequate. The lift-off lithography was not finalised by oxygen plasma removal of resist residuals because of the wish to avoid heating effect from the plasma reactor. Lithography was finalized only by rinsing in deionised water for a predetermined time to dilute out the residual developer from the sample, followed by NH_4OH and HCl dips prior to metallisation.

It is very probable that not all of the residual developer or resist was removed. As a result, the sample surface was probably not clean enough for a high quality contact formation. Additionally, the evaporation of ohmic metals for emitter and collector were far from succesfull according to process diary. From Figure f54 it is also seen that the current gain of the device was not affected by ageing, which suggests that the actual epitaxial composition of the device did not alter over time.

Figure f55 shows how the stress introduced by device measurements may affect the degraded contacts. A transistor from the process run “C” that had degraded for six months showing similar symptoms as in Figure f54 was stressed by repeated measurement sweeps for collector characteristics. The 4145 parameter analyzer with “medium” integration time was used in the experiment. One measurement sweep completed in about 10 seconds. Special care was taken to achieve good probe needle contacts to device.

The measurement was left running in a loop for definite time to monitor possible changes. Figure f55 gives collector characteristics of the device at the beginning of the experiment (blue diamonds), after one hour (pink squares) and after 20 hours (yellow triangles). It is seen from the figure that the repeated measurement stress affected both the contact region and current gain of the device. Most of the change occurred within 1 hours. The 20 hours result diverges from 1 hour result in high current region mainly due to probe needle contact degradation.

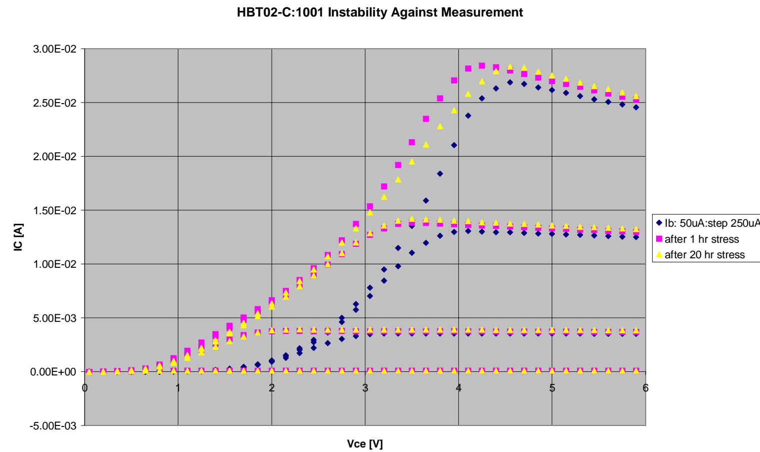

Figure f55: Instability of the device against measurement stress. The sample was first allowed to degrade for six months and then stressed by repeated IV-measurements for 1 hours (pink squares) and 20 hours (yellow triangles).

It is seen from Figure f55 that the device tend to become leaky after stress, suggesting that the nonlinear contact has become more ohmic. The change in current gain suggests that the active parts of the device were also affected by the effort. This is more readily seen from Figure f56, where comparison is made between measurement result of the newly processed device and the same device after six months of ageing and successive electrical stress. It is seen that the device does not turn on as sharply any longer. There is considerable leak present with the once rectifying contact, while series resitance is increased. Current gain is also increased considerably.

Gummel plot of the device after stress is shown in Figure f57. V_{CB} was kept at zero volts during the measurement. It is seen that the device starts to show current gain with V_{BE} exceeding 1,5V. Nonlinearity of the collector contact has now lesser impact on forward Gummel plot vith V_{CB} = 0V. Reverse Gummel plot measurements were still not possible. Also shown in the figure is the result of fitting to ideal diode law. Base current obeyed diode law with $Is = 2 \cdot 10^{-15}$ A and n = 1,857. Collector current parameters were $Is = 4 \cdot 10^{-21}$ A and n = 1,264. Device emitter area was 20 µm x 20 µm.

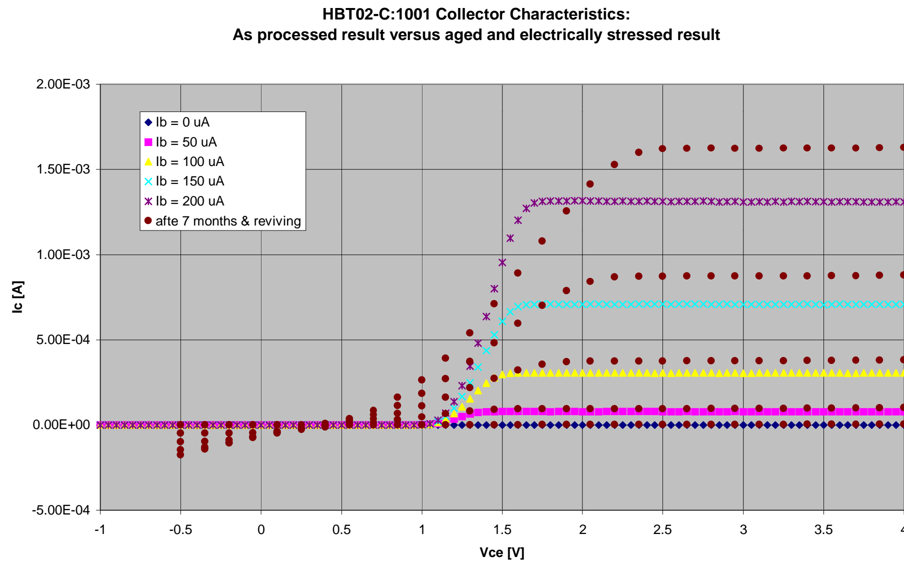

Figure f56: Device characteristics after six months of ageing and electrical stress.

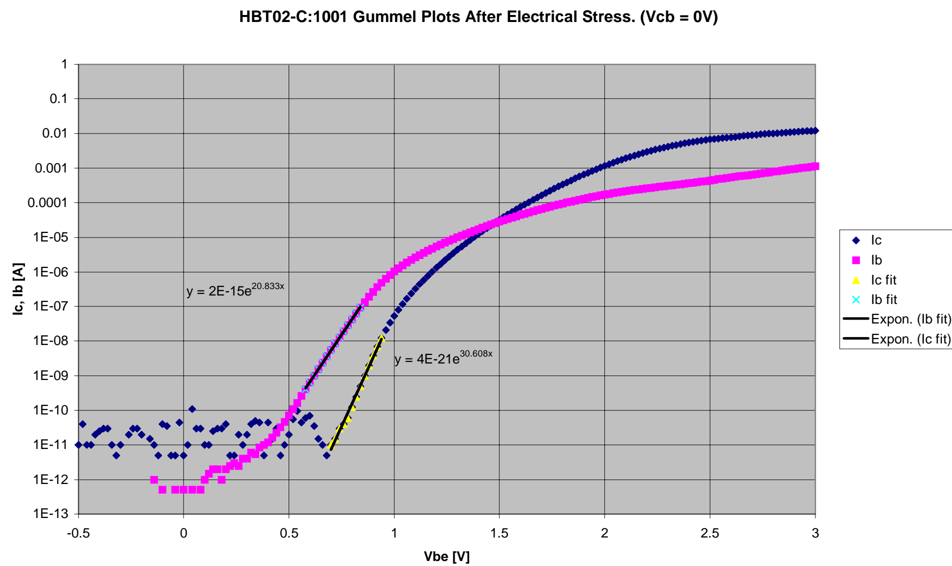

Figure f57: Gummel plot of the device after stress experiment.

It is worth to note that transistor measurements with forced base current implicitly force V_{BE} to vary accordingly in order to maintain constant base current over the entire sweep of V_{CE}. Figure f58 shows the V_{BE} variation as observed during the measurements for Figure f56. I_B values with dotted labels refer to the measurement after ageing and electrical stress. It is seen that external base voltage for a given base current was increased considerably, and V_{BE} for low V_{CE} values is no longer constant because of the leak currents. In that respect, the as-processed measurement result is pathologically neat, suggesting that the V_{BE} result may be interpreted with simple arguments. Considering V_{BE} being affected by resistive loss across base resitance R_b and emitter resistance R_e , and emitter diode obeying diode law, and assuming that all of the base current eventually flow through emitter resistance, V_{BE} should be calculated by

(e137) $$V_{BE} = \frac{nkT}{q} \ln\left(\frac{I_B}{I_s}\right) + I_B\left(R_b + R_e\right) + I_C R_e .$$

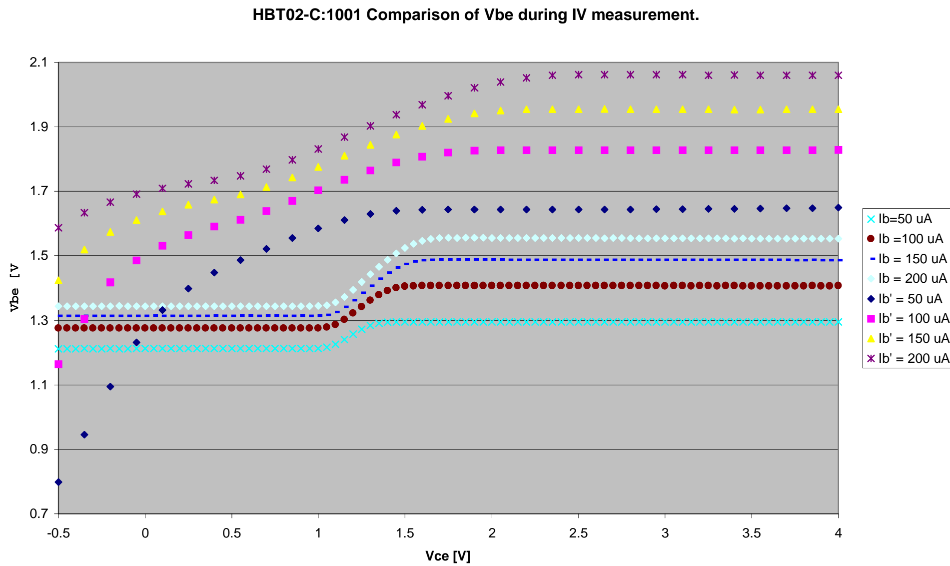

Figure f58: V_{BE} that was needed to maintain the constant base current condition during measurements for Figure f56.

Trial to fit the as-processed measurement data into equation (e137) was not satisfactory unless the emitter resistance value was allowed to drift. Equation (e137) fitted to measurement data with diode ideality factor n = 2 and R_b = 50 Ω when R_e and I_s depended on base current as shown in Table IV. It is seen that the heterojunction emitter had a nonlinear character left despite the compositional grading of the epitaxial structure of the device, which is reflected into the necessity to vary the value of R_e in the simple fitting equation of the as-processed device. The stress experiment may have affected the device emitter heterojunction in a way that the residual conduction band spike was lowered while the ohmic losses in the emitter volume increased yielding to the observed results of Figure f56 for gain and turn on characteristics. In normal operation at junction temperatures below 250^0C HBTs are known to degrade by increase in the number of point defects with a current assisted mechanism [r50], [r54], [r55]. Rapid degradation was associated with a dark line defect that was identified with electroluminescence imaging method.

It may be concluded that the emitter heterojunction design need to be re-evaluated for future applications. One of the weakest design parameters was the thickness of spacer layer that was to prevent Be diffusion into emitter heterojunction, which should have been determined experimentally. Also, the grading distances in either side of the emitter may not have been at optimum. It seems that the observed high numerical values of emitter resistances were only partially due to ohmic contacts, and the possibility of the existence of the conduction band spike has to be taken into account in the Spice simulations. For the devices processed within this thesis the series resistances were themselves high, such that the device DC performance was possible to be modeled through a simple pSpice transistor equivalent circuit as the finer aspects of heterojunction were screened out.

	Ib = 50 µA	Ib = 100 µA	Ib = 150 µA	Ib = 200 µA
Is	$8 \cdot 10^{-15}$ A	$4 \cdot 10^{-15}$ A	$3 \cdot 10^{-15}$ A	$2 \cdot 10^{-15}$ A
Re	950 Ω	400 Ω	250 Ω	150 Ω

TABLE IV: Saturation current and emitter resistance as obtained from V_{BE} fit to measurement data of the as-processed device.

4.6 Evaluation of the Frequency Response of the Processed Devices

The purpose of this thesis was to study the processing of new semiconductor devices such as heterojunction bipolar transistors. Optimisation for high speed device performance is relevant as soon as the processing itself is at routine level. This thesis contained just about enough process runs to set up the minimum level of practise for routine processing of conventional mesa isolated heterojunction devices for DC and low frequency purposes. It was beyond the scope of this thesis to raise up a process flow that could be directly applied to high volume production of commercially relevant devices. The optimisation for high speed is about minimising parasitic resistances and reactances in device design to minimise RC delays in the circuit. Matching the device to the signal line is crucial beyond frequencies over a few gigahertz. It would not have been practical to jump over to high speed optimisation with this thesis, due to the lack of previous knowledge on process parameters. The high speed performance of the processed devices was thus of secondary importance.

However, as a demonstration of the capabilities of heterojunction bipolar technology, frequency characteristics of a device from process run “B” was measured for future reference. The device emitter area was 10 µm x 50 µm with sigle sided base contact. The original device was of DC design with measurement pads in a conventional 100 µm x 100 µm matrix. The device wiring metallisation was redesigned and reprocessed to facilitate on-wafer RF-probing with G-S-G type probes in 150 µm pitch. As a useful addendum to the processing skills in the laboratory, a simple electron beam process was set up for lithographical mask making, and the device wiring metallisation was reprocessed by add-on method to adopt G-S-G probing.

Scattering parameter measurement was performed by Microwave Engineering Laboratory of Technical University of Berlin. The bias condition was V_{CE} = 6,0V and V_{BE} = 1,7 V for I_C = 12 mA and I_B = 650 µA in common emitter configuration. Frequency was swept from 100MHz to 6900MHz during S-parameter measurement. Scattering parameter *S21* gives the forward transfer characteristics from base-emitter input port to collector-emitter output port. Small signal current gain of the device is obtained after converting scattering parameters to hybrid or h-parameters. The magnitude of parameter *h21* gives device current gain. There are several tools available for doing the mechanical conversion automatically.

For this thesis the conversion was done with a demonstration version of *Smith*™-software programmed in University of Applied Sciences, Berne, Switzerland, and distributed at the time of writing as freeware by *RFGlobalnet* at *www.rfglobalnet.com* site. Figure f59 shows the frequency dependence of the small signal gain for the measured device. The current gain cuts off at f_t = 2,3 GHz. According to data analysis with *Smith*-software the maximum oscillation frequency f_{max}, or the maximum power gain cut off frequency, was about 1,1 GHz. In a well designed HBT the current gain rolls off at a rate of 20 dB per decade increase of frequency. Tenfold increase in frequency should reduce gain tenfold. In Figure f59 the decrease is only fourfold, or 12 dB/decade. It is known that excessive back injection current in base-emitter junction causes the slope to reduce to 10dB/decade [r14]. The explanation is adequate for the transistor under measurement, and is an indication that the valence band discontinuity was not holding off holes efficiently at the used bias conditions for measurement.

It may be concluded that even the basic process that was designed for DC device characterisation with apparent emitter resistances of about hundred times more than preferable was capable of introducing power gain in gigahertz range. This is an encouraging result for the future refinement of the process towards applicable high speed device processing.

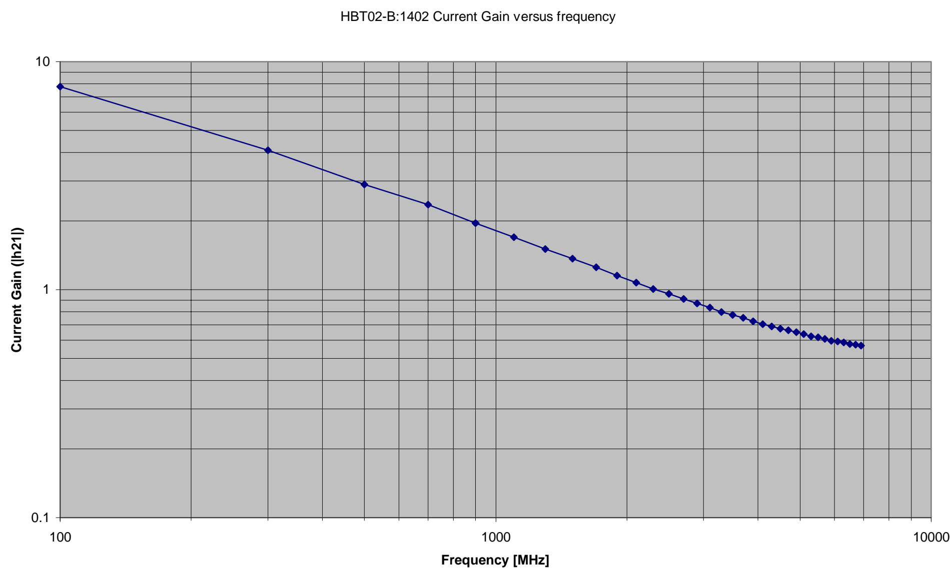

Figure f59: Small signal gain versus frequency of the measured transistor. The current gain cut off frequency was f_t = 2,3 GHz.

5 Conclusions

Processing and characterization of high speed compound semiconductor devices was studied with emphasis on the conventional wet chemically isolated AlGaAs/GaAs heterojunction bipolar transistor. The aim was to develop a laboratory scale process for research and educational purposes. Physical one dimensional device simulation and practical work on process development together resulted in a feasible process scheme. Excluding the numerous separate experiments on the individual process steps, the process development contained three complete process runs. The current gain and DC performance of the last processed samples accorded with the simulation predictions showing that the process is applicable to reach controlled device performance. The measurement results were possible to fit into a simple pSpice equivalent circuit with appreciable confidence.

At early stage of process development it was observed that the first devices were easily destroyed by excessive heating during ohmic contact formation. The process was then modified towards low thermal energy budget, avoiding any source of heat but implicit to the PECVD nitridation. Different contact metal choices were tested for applicability in non-alloyed contact formation against a reference of a Cr/Au based non-alloyed scheme. It was verified that for short term testing purposes Cr/Au may serve as a basic contact metal if InGaAs-capped emitter is used. Collector contact will then be a rectifying diode. Substitution of Cr/Au with Pd/Ge/Pd/Au resulted in ohmic contacts in both emitter and collector. It was also observed that a device with Pd/AuGe/Ag/Au with InGaAs capping layer as emitter contact scheme, Ni/AuZn as base contact scheme and Cr/Au rectifying collector diode contact yielded to very good transistor performance with respect to DC characteristics. However, it was left open whether the actual collector contact contained residuals of palladium, which is a true possibility with reference to the process diary. Palladium is known on its capability to penetrate native oxides, which may have helped in collector contact formation. Future refinement of the process should include re-examination of the collector metallisation comparing Cr/Au and Pd/Cr/Au. Finally, it was observed that the processed devices were rather unstable with time and with electrical stress. This is conceivable to occur with low thermal budget processing. The long term reliability is a concern if the process if further refined towards device applications.

Shallow air bridges and metal cross-overs were included to facilitate process application for the future needs in high speed compound semiconductor device processing. Passive structures such as coils, capacitors and resistors are possible with the process. Electrochemical plating of wiring metallization should be further examined to turn the process more applicable with respect to low resistivity wiring and mechanically stronger air bridging. Preliminary tests on copper plating were made, but not included in the text of this thesis in length. The tests showed that the plating process should not possess a problem, if the adhesion of initial wiring metal is good enough. Otherwise the plated metal contains bumps of loose metal film. A perhaps useful note for future reference about the plating experiment was that also the back side of the GaAs wafer got plated by copper during the experiment seemingly smoothly. This should facilitate the process refinement towards high speed devices with ground metallizations carried through via holes in the thinned GaAs substrate.

Although the processing steps were demonstrated with AlGaAs/GaAs-based material, most of the processing methods that were adopted are applicable also for, e.g., GaInAs/InP-material with some adjustment in etching processes and metallisation choices. As such, the process is ready to be used as a tool for laboratory scale research and education on HBT technology.

6 Acknowledgements

I wish to thank Dr. Alexei Malinin and Janne Kylmäluoma for assistance with PECVD nitrides, and Dr. Anni Seppälä from Helsinki University for the Rutherford back scattering measurements during the studies of e-beam evaporated metal layers. The staff with the Laboratory of Electronics Production Technology of Helsinki University of Technology was of great help in the plating experiments and with the interpretation of phase diagrams of metal compounds. Dr. Mikko Taskinen and Dr. Lauri Knuuttila deserve a special thank for making my early HBT samples with Zn-base doping with their MOCVD at Optoelectronics laboratory of Helsinki University of Technology. I appreciate the contribution of *EMCEC Oy* to this work by donation of the HP4145A parameter measurement apparatus with associated fixtures for Electron Physics Laboratory.

I express my gratitude to Dr. Darrell Hill with *TriQuint Semiconductor* for his warm encouragement and sympathy during my early efforts in process development of HBT's. I also express my appreciation to Dr. Nikolai Maleev with A. F. Ioffe Physico-Technical Institute, St. Petersburg, for his fruitful comments on the design of the epitaxial structure of the HBT and growing the final samples with beryllium base doping with their MBE. I wish also to acknowledge the help of Dr. Kai Schmidt von Behren with Microwave Engineering Laboratory of Technical University of Berlin, with the scattering parameter measurements of the transistors. Most of all, I wish to hail the contribution of Mr. Risto Salo to my work by his uncompromising devotion to the cause of modernisation of the clean room facilities in our university.

7 References

[r01] Kroemer H: *Heterostructure Bipolar Transistors and Integrated Circuits*, Proc. IEEE, Vol. 70, No. 1, 1982, pp. 13-25

[r02] The Royal Academy of Sciences Press Release on the Nobel Prize in Physics 2000, October 10, 2000

[r03] Kroemer, H.: *Theory of a Wide-Gap Emitter for Transistors*, Proc. IRE, Vol. 45, No. 11, 1957, pp. 1535-1537

[r04] Morozov, Y. V.: *Personalia Zhores Ivanovich Alferov (on his seventieth birthday),* Physics – Uspekhi, Vol. 43, no. 3, 2000, pp. 307-08

[r05] *U.S. Patent No. 2569347* to W. Shockley, Filed 26 June 1948, expired 24 September 1968

[r06] Bardeen J., Brattain W. H.: *The Transistor, a Semi-Conducting Triode,* Phys. Rev., Vol. 74, June 25, 1948, pp. 230-331

[r07] Hill, D.: *High Voltage HBT Technology*, IEEE 20th GaAs IC Symposium 1998 Technical digest, 1998, pp. 149 - 52

[r08] Lee, Q., Martin, S. C., Mensa, D., Smith, R. P., Guthrie, J., Rodwell, M. J. W.: *Submicron Transferred-Substrate Heterojunction Bipolar Transistors*, IEEE Eletron. Dev. Lett., Vol. 20, No. 8, 1999 pp. 396-98

[r09] Hovinen, A.: *Fabrication of a Heterojunction Transistor*, Master's Thesis, Electron Physics Laboratory, Helsinki University of Technology, Espoo 1992 (in Finnish)

[r10] Hovinen A.: *Fabrication of a Crystalline Thin Film Solar Cell*, Licentiate's Thesis, Electron Physics Laboratory, Helsinki University of Technology, Espoo 1995 (in Finnish)

[r11] Anholt R., *Electrical and Thermal Characterization of MESFETs, HEMTs, and HBTs,* , Artech House, Boston, 1995

[r12] Seely, S.: *Electron Tube Circuits*, McGraw-Hill, N.Y., 1958

[r13] Sze, S. M., *Physics of Semiconductor Devices,* 2nd ed., John Wiley & Sons, New York, 1981

[r14] Liu, W., *Handbook of III-V Heterojunction Bipolar Transistors,* John Wiley & Sons, New York, 1998

[r15] Wood, D.: *Optoelectronic Semiconductor Devices*, Prentice Hall, Hertfordshire, 1994

[r16] Das, M. B. in Ali, F., Gupta, A.: *HEMTs and HBTs : Devices, Fabrication, and Circuits,* Artech House, Boston (MA), 1991

[r17] Böer, K.W., *Survey of Semiconductor Physics, Vol II: Barriers, Junctions, Surfaces and Devices,* Van Nostrand Reinhold, New York, 1992

[r18] Alonso, M., Finn, E. J.: *Fundamental University Physics*, Vol 1: Mechanics and Thermodynamics, 2nd ed., Addison-Wesley, 1980

[r19] Grinberg, A. A., Shur, M. S., Fischer, R. J., Morkoc, H.: *An Investigation of the Effect of Graded Layers and Tunneling on the Performance of AlGaAs / GaAs Heterojunction Bipolar Transistors*, IEEE Trans. El. Dev., vol. ED-31, no. 12, December 1984

[r20] Das, A., Lundstrom, M. S., *Numerical Study of Emitter-Base Junction Design for AlGaAs/GaAs Heterojunction Bipolar Transistors*, IEEE Trans. El. Dev., vol. 35, no. 7, July 1988

[r21] Kennedy, D. P.: *The Potential and Electric Field at the Metallurgical Boundary of an abrupt p-n semiconductor junction*, IEEE Trans. Electr. Dev., 22, 1975, 988-994

[r22] Basore P. A. et al.: *PC-1D Version 2: Enhanced Numerical Solar Cell Modeling*, Proceedings of the 20th IEEE Photovoltaic Specialists Conference, pp. 389-96, 1988

[r23] Shur, M.: *Recombination Current in Forward Biased p-n junctions,* IEEE Trans. El. Dev., vol. 35, no. 9, September 1988

[r24] Klausmeier-Brown, M. E., Lundstrom, M. S., Melloch, M. R.: *The effects of Heavy Impurity Doping on AlGaAs/GaAs Bipolar Transistors*, IEEE Trans. El. Dev., Vol. 36, no. 10, 1989

[r25] Harmon, E. S., Melloch, M. R., Lundstrom, M. S.: *Effective Band Gap Shrinkage in GaAs*, Appl. Phys. Lett., Vol. 64, no. 4, 1994

[r26] Hovinen, A., Malinin, A., Lipsanen A.: *Lithography in Experimental Environment,* Reports in Electron Physics 2000/21, Helsinki University of Technology, Espoo 2000

[r27] Hovinen, A., Lipsanen A.: *Processing of AlGaAs-GaAs Heterojunction Bipolar Transistors,* Reports in Electron Physics 2000/22, Helsinki University of Technology, Espoo 2000

[r28] Kurishima, K. et al., *Growth, Design and Performance of InP-based Heterostructure Bipolar Transistors,* K. IEICE Trans. Electron., vol. E78-C, no. 9, pp. 1171-80, 1995

[r29] Shur, M., *GaAs Devices and Circuits,* M. Plenum Press, New York, 1987

[r30] Tiwari, S., Wright, S.L., Frank, D. J.: *Compound Semiconductor Heterostructure Bipolar Transistors,* IBM J. Res. Develop. vol. 34, no. 4, 1990

[r31] Wang, L. C., Wang, X. Z., Lau, S. S., Sands, T., Chan, W. K., Kuech, T. F.: *Stable and Shallow PdIn ohmic Contacts to n-GaAs,* Appl. Phys. Lett., vol 56, no. 21, pp. 2129-31, 1990

[r32] Pruniaux, B. R., Adams, A. C.: *Dependence of Barrier Height of Metal Semiconductor (Au-GaAs) on Thickness of Semiconductor Surface Layers,* J. Appl. Phys., vol. 43, pp. 1980-03, 1972

[r33] Mukherjee, S. D., Woodard, D. W.: *Etching and Surface Preparation of GaAs for Device Fabrication,* in Howes, M. J., Morgan D. V. (ed.): Gallium Arsenide Materials, Devices and Circuits, New York, 1985, John Wiley & Sons, pp. 119-60

[r34] Shih, Y.-C., Murakami, M., Wilkie, E. L., Callegari A. C.: *Effects of Interfacial Microstructure on Uniformity and Thermal Stability of AuNiGe Ohmic Contact to N-type GaAs*, J. Appl. Phys., vol 62, no. 2, pp. 582-9, 1987

[r35] Stareev, G., Künzel, H.: *A Controllable Mechanism of Forming Extremely Low-resistance Nonalloyed Ohmic Contacts to Group III-V Compound Semiconductors,* J. Appl. Phys., vol. 74, no. 12, pp. 7344-56, 1993

[r36] Yeh, Y.-H., Lai, J.-T., Lee, J. Y.: *Low Contact–Resistance and Shallow Pd/Ge Ohmic Contacts to n- $In_{0.53}Ga_{0.47}As$ on InP Substrate Formed by Rapid Thermal Annealing,* Jpn. J. Appl. Phys., vol. 35, pp. L 1569-71, 1996

[r37] Huelsman, A. D., Fonstad, C. G.: *Compositional Changes during Alloying of Ohmic Contacts to $In_{0.53}Ga_{0.47}As$,* J. Electrochem. Soc. Solid-State Science and Technology, vol. 132, no. 12, pp. 2989-92, 1985

[r38] Wakita, A., Moll, N., Ficher-Colbrie, A.: *Design and Surface Chemistry of Nonalloyed Ohmic Contacts to Pseudomorphic InGaAs on n^+GaAs,* J. Appl. Phys., vol. 68, no. 6, pp. 2833-8, 1990

[r39] Massalski, T.B.: *Binary Alloy Phase Diagrams*, ASM International, 1996

[r40] Stareev, G.: *Formation of Extremely low Resistance Ti/Pt/Au ohmic Contacts to p-GaAs,* Appl. Phys. Lett. vol. 62, no. 22, pp. 2801-03, 1993

[r41] Sugiyama T. et al..: *Ultra-Low Resistance Base Ohmic Contact with Pt/Ti/Pt/Au for High-f_{max} AlGaAs / GaAs Heterojunction Bipolar Transistors,* Jpn. J. Appl. Phys., vol. 33. part 1, no. 1B, pp. 786-9, 1994

[r42] Kazuhiko, T., Masaru, S., Koichi, K.: *Submicrometer Optical Lithography Using a Double-Layer Resist by a single Development Technology*, IEEE Trans. on El. Dev., vol. ED-31, no. 12, 1984

[r43] Liou, Juin J., Huang, Chern I., Bayraktaroglu, B.: *A Physics Based, Analytical Heterojunction Bipolar Transistor Model Including Thermal and High Current Effects*, IEEE Trans. El. Dev., Vol. 40, no. 9, 1993

[r44] Suematsu, E., Ogawa, H.: *Frequency Response of HBT's as Photodetectors*, IEEE Microwave and Guided Wave Letters, Vol. 3., no. 7, 1993

[r45] Blakemore, J. S.: *Semiconducting and Other Major Properties of Gallium Arsenide*, J. Appl. Phys., vol 53, no. 10, 1982

[r46] Sinkkonen, J., Ruokolainen J., Uotila P., Hovinen A.: *Spatial Collection Efficiency of a Solar Cell*, Appl. Phys. Lett., vol. 66., no. 2, 1995

[r47] Roenker, K. P., Frimel, S. M., Cahay, M. M.: *Effects of Optical Absorption on the Quasi Fermi Level Splitting at the Emitter-Base Junction in npn Heterojunction Bipolar Phototransistors*, IEEE Trans. El. Dev., Vol. 46., no. 4, 1999

[r48] Grove, A.S.: *Physics and Technology of Semiconductor Devices,* J. Wiley & Sons, New York, 1967

[r49] Hovinen, A.: *Fitting of the Solar Cell IV-curve to the Two Diode Model*, Physica Scripta, Vol. T54, 1994 pp. 175 – 76

[r50] Henderson, T.: *Model for Degradation of GaAs/AlGaAs HBTs Under Temperature and Current Stress*, 1995 IEEE International Electron Devices Meeting Digest, pp. 811-14

[r51] Das, M. B. in Ali, F., Gupta, A.: *HEMTs and HBTs : Devices, Fabrication and Circuits*, Artech House, Boston, 1991

[r52] Morkoc, H, Sverdlov, B., Gao, Guang-Bo: *Strained Layer Heterostructures and their Applications to MODFET's, HBT's and Lasers*, Proc. IEEE, vol. 81, no. 4, 1993, pp. 493 – 56

[r53] Nagata, K. et al.: *Self-aligned AlGaAs/GaAs HBT with Low Emitter Resistance Utilizing InGaAs Cap Layer*, IEEE Trans. El. Dev., vol. ED-35, no. 1, 1988, pp.2-7

[r54] Bovolon, N., et al.: *Analysis of the Short-Term DC-Current Gain Variation During High Current Density-Low Temperature Stress of AlGaAs/GaAs Heterojunction Bipolar Transistors*, IEEE Trans. El. Dev., vol. 47, no. 2, 2000, pp. 274 – 81

[r55] Adlerstein, M. G., Gering, J. M.: *Current Induced Degradation in GaAs HBT's*, IEEE Trans. El. Dev., vol. 47, no. 2, 2000, pp. 434 – 39

[r56] Marsh, S. P.: *Direct ExtractionTechnique to Derive the Junction Temperature of HBT's Under High Self-Heating Bias Conditions*, IEEE Trans. El. Dev., vol. 47, no. 2, 2000, pp. 288 – 91